UNIVERSITY OF CALIFORNIA,
IRVINE

Methodology for Non-covalent Attachment of Molecular Species onto Electrode Surfaces and Electrochemical Studies with Nitrogenase from *Azotobacter vinelandii* Towards Synthetic Fuel Forming Reactions

DISSERTATION

submitted in partial satisfaction of the requirements
for the degree of

DOCTOR OF PHILOSOPHY

in Chemistry

by

Brian Raymond Lydon

Dissertation Committee:
Assistant Professor Jenny Y. Yang, Chair
Professor Andrew S. Borovik
Assistant Professor Shane Ardo

2019

DEDICATION

To

Mom, Dad, Nikki, and Grandma

TABLE OF CONTENTS

LIST OF FIGURES

LIST OF TABLES

LIST OF SCHEMES

ACKNOWLEDGMENTS

I would like to express my deepest gratitude to my advisor Prof. Jenny Y. Yang for allowing me to be one of her first graduate students. Although I may forever hold the Yang Lab record for most missed deadlines, thank you for your patience, your trust in giving me difficult projects, and working with me to always improve as a scientist.

Thank you to my committee members Prof. Shane Ardo and Prof. A. S. Borovik for helpful discussions about electrochemistry and metallobiochemistry respectively. Also, thank you Prof. Ardo for your bottomless well of positivity and ideas when it comes to solving problems.

Thank you to my collaborators Prof. Markus Ribbe and Prof. Yilin Hu for allowing me to use their labs' proteins, cofactors, and instrumentation. Thank you to Dr. Nate Sickerman, Dr. Caleb Hiller, and Megan Newcomb for invaluable discussions and advice about nitrogenase and working with me with little to no notice. Thank you to Dr. C. C. Lee, Johannes Rebelein, and Kazuki Tanifuji for allowing me to use their personal stock of proteins and cofactors. Additionally, thank you to Prof. Manny Soriaga and Dr. Alnald Javier for helpful discussions and advice for experiments in Chapter 1 relating to gold.

Thank you to all of my labmates in the Yang Lab who kept the lab space an amazing and friendly atmosphere for scientific discussion and experiments, especially: Dr. Charlene Tsay, Dr. Juliet Kotyk, Steve Poteet, Bianca Ceballos, Alex Reath, Caitlin Hanna, Jeff Barlow, Alex Germann and Wyeth Gibson. Special thank you to Zach Thammavongsy for sticking through graduate school with me the entire way and being an amazing friend that I can always rely on.

Without the help of the many facility directors at UCI I would have been absolutely lost on day 1 of graduate school. I would like to greatly express my gratitude for the help and assistance I received from: Dr. Qiyin Lin, Dr. Ich Tran, and Zhongyue Luan for XPS experiments; Dr. Phil Dennison for NMR experiments; Dr. Felix Grun for working with me on specialized GC and MS experiments. I would like to express a big special thank you to Jorge Meyer and the Meyer family for personally working with me and producing specialty high quality glassware that I never would have otherwise been able to obtain.

I would like to thank all of my family and friends who have supported me the last five and a half years: John, Sheri, Sally, Sean, Kevin, Ryan and P.J. as well as the entire extended Lydon and Salazar families and friends. Without your continued support and words of motivation, I doubt I could have completed this document.

Finally, I would like to thank my wife, Nikki, who has been with me on this journey since my days in community college nearly 10 years ago. I am exceedingly lucky and thankful that I found someone to support me through some of the toughest years of my life and beyond.

I would like to acknowledge The Royal Society of Chemistry for reproduction of portions of chapter 1 and WILEY-VCH Verlag GmbH & Co. for reproduction of Figure 3.1.

CURRICULUM VITAE

Brian R. Lydon

EDUCATION

- **Ph.D.** Chemistry, University of California, Irvine. 2019
  Advisor: Professor Jenny Y. Yang
- **M.S. & B.S.** Chemistry, University of California, Los Angeles. 2013
  Advisor: Professor Paula L. Diaconescu

PUBLICATIONS

1. Lydon, B. R.; Germann, A.; Yang, J. Y., *Chemical Modification of Gold Electrodes via Non-Covalent Interactions*. Inorganic Chemistry Frontiers **2017,** 3, 836-841.

2. Upton, B. M.; Gipson, R. M.; Duhovic, S.; Lydon, B. R.; Matsumoto, N. M.; Maynard, H. D.; Diaconescu, P. L., *Synthesis of ferrocene-functionalized monomers for biodegradable polymer formation.* Inorganic Chemistry Frontiers **2014**, 1 (3), 271-277.

3. Alexandrova, A. N.; Nechay, M. R.; Lydon, B. R.; Buchan, D. P.; Yeh, A. J.; Tai, M.-H.; Kostrikin, I. P.; Gabrielyan, L., *The same in the bulk but different as clusters: X3Y3 (X = B, Al, Ga; Y = P, As).* Chemical Physics Letters **2013**, 588 (0), 37-42.

AWARDS

2013 Dolores Cannon Southam Award for Excellence in Research,
University of California, Los Angeles

2012 Chemistry Departmental Scholar**,**
University of California, Los Angeles

2012 Raymond and Dorothy Wilson Endowment Summer Research Fellowship,
University of California, Los Angeles

PRESENTATIONS (Oral or Poster)

2017 Poster Presentation: "Electrocatalytic reduction of CO and CO_2 using VFe and MoFe protein bioelectrodes" Socal Bioinorganic 2017 Meeting

2017 Oral Presentation: "Method for non-covalent attachment of molecules to electrodes and nitrogenase electrochemistry" UCI Inorganic Chemistry Student Seminar Series

2016 Poster Presentation: "A Modular Method for Non-covalently Adsorbing Molecular Catalysts to Surfaces" SoCal Organometallics Spring 2016 Meeting

2016 Oral Presentation: "A Modular Method for Non-covalently Adsorbing Molecular Catalysts to Surfaces" *251st* American Chemical Society National Meeting

TEACHING EXPERIENCE

2013 - 2018 Graduate Teaching Assistant, Irvine, CA

Metallobiochemistry (Chem 218)
Inorganic Chemistry Laboratory (Chem 107L)
Organic Chemistry Laboratory (Chem 51LC, 51LD)
Honors General Chemistry Laboratory (Chem M2LA/H2LA)
General Chemistry Laboratory (Chem 1LC, 1LD)

Mentor to undergraduate researchers

2016 - 2018 Wyeth S. Gibson
2014 Alex Germann

COMMUNITY SERVICE

2013 - 2018 UCI Laboratory Experiments and Activities Program (LEAPS)
2016 UCI Math CEO Program

ABSTRACT OF THE DISSERTATION

Methodology for Non-covalent Attachment of Molecular Species onto Electrode Surfaces and Electrochemical Studies Involving Nitrogenase from *Azotobacter vinelandii* Towards Synthetic Fuel-Forming Reactions

By

Brian Raymond Lydon

Doctor of Philosophy in Chemistry

University of California, Irvine, 2019

Professor Jenny Y. Yang, Chair

As solar energy becomes the primary renewable energy resource, its intermittency still remains an important issue. One solution to solar intermittency is to store harvested excess solar energy in carbon-based chemical fuels that are compatible with our energy infrastructure through utilization of molecular catalysts. This dissertation describes three projects that are motivated by electrocatalytic conversion of C1 feedstocks to reduced products.

Chapter 1 describes a successful proof-of-concept model for non-covalent immobilization of molecular species to surfaces using aromatic π-π interactions. Aromatic character was imparted to a gold surface through functionalization of a pyrene-containing self-assembled monolayer. After exposure of the aromatized gold surface to a pyrene-functionalized ferrocene solution, it maintained facile electron transfer to the ferrocene. X-ray photoelectron spectroscopy, infrared spectroscopy, and cyclic voltammetry were used to demonstrate successful physisorption of the pyrene-functionalized ferrocene onto the pyrene-modified gold

surface. Physisorption is attributed to pyrene–pyrene (π) interactions, as the ferrocene compound was not observed after identical treatment of an unmodified gold electrode surface.

Chapter 2 describes the electrochemical characterization of isolated nitrogenase cofactors from *Azotobacter vinelandii*. Voltammetric studies were performed on three isolated nitrogenase cofactor species: the iron-molybdenum cofactor (M-cluster), iron-vanadium cofactor (V-cluster), and a homologue to the iron-iron cofactor (L-cluster). Two reductive events were observed in the redox profiles of all three cofactors. The reduction potentials of the isolated cofactors are significantly more negative compared to previously measured values within the molybdenum-iron and vanadium-iron proteins. The outcome of this study provides insights into the importance of the heterometal identity, the overall ligation of the cluster, and the impact of the protein scaffolds on the overall electronic structures of the cofactors.

Chapter 3 describes the integration of nitrogenase enzymes into bioelectrodes for the electrocatalytic conversion of sodium nitrite, sodium azide, carbon monoxide, and carbon dioxide to reduced products. Cyclic voltammetry experiments demonstrate that the vanadium-iron protein is the only protein in this study that is able to reduce carbon monoxide. Preliminary controlled potential electrolysis studies in tandem with gas chromatography suggest that the products formed from the mediated electroreduction of CO using the vanadium-iron protein are C1-C4 hydrocarbons.

INTRODUCTION

0.1 Carbon-based Energy Infrastructure and Renewable Energy Storage

Since the advent of the industrial revolution, fossil fuels such as coal, oil, and natural gas have been a primary and cost effective means to power modern society.[1] Combustion of fossil fuels (eq 1) produces a release of enthalpic energy upon oxidation of C-C and C-H bonds yielding water and carbon dioxide which are subsequently discarded as waste into the atmosphere. According to the United States Energy Information Administration, approximately 80% of the energy consumed by the United States in 2017 was derived from fossil fuel sources; only 11% of energy consumed was derived from renewable sources, and 9% from nuclear electric power.[2] In addition to the finite supply of accessible fossil fuel reserves, the greenhouse gas effect from carbon dioxide has caused a measurable shift in Earth's climate contributing to anthropogenic global warming.[3-5]

$$\mathbf{C_xH_y + zO_2 \longrightarrow xCO_2 + 0.5yH_2O + energy} \qquad \mathbf{(1)}$$
$$\mathbf{where\ z = x + 0.25y}$$

As global energy consumption is projected to increase 48% between 2012 and 2040 the need for alternative energy solutions is imperative to the health and success of future generations.[2] In order to decrease dependence on fossil fuels and simultaneously reverse the effects of climate change, three research areas need to be rapidly co-developed: atmospheric CO_2 capture, efficient conversion of renewable energy, and renewable energy storage. The latter research area is the motivation for the work herein.

In terms of maximum theoretical output, the sun consistently provides the Earth between 10^3-10^4 times more power than any other renewable resource.[6] To harvest the sun's energy,

photovoltaic cells made from semiconducting materials with bandgaps in the solar spectrum are needed to convert light to electricity.[7-12] Intermittency of available solar energy caused by the Earth's natural day/night cycle translates to a lack of directly accessible energy when the sun is not shining. As a solution to solar intermittency, excess energy can be stored in the form of chemical potential to be utilized at a later time.[13]

Lithium ion battery and other rechargeable battery technologies have advanced greatly since their invention in 1976 and are a useful tool in the direct utilization of stored electrical potential,[14-17] but there are numerous issues surrounding them that have yet to be addressed including: poor storage capacity, finite charge/discharge cycles, self-discharge, and a finite supply of lithium that would be unsustainable for mass energy storage on a global scale.[18-20]

Alternatively, chemical covalent bonds are a convenient form of energy storage;[21] breaking energy dense chemical bonds either through combustion or a fuel cell provides an accessible pathway to utilize the energy stored within them. Nature has demonstrated that energy can be densely stored in C-C and C-H chemical bonds using solar energy through the process of photosynthesis (eq 2). The enzyme ribulose-1,5-bisphosphate carboxylase (RuBisCO) which binds CO_2 during the Calvin cycle is highly selective for carbon dioxide at very low atmospheric concentrations of CO_2 compared to state-of-the-art synthetic catalysts which often require oxygen-free conditions and concentrated CO_2 to operate.[22-25]

$$\mathbf{6CO_2 + 6H_2O \xrightarrow[RuBisCO]{sunlight} C_6H_{12}O_6 + 6O_2} \qquad \mathbf{(2)}$$

Liquid carbon-based fuels provide superior energy density over current commercial rechargeable battery technology (Figure 0.1).[20,26] In order to generate chemical fuels that are compatible with the world's carbon-based energy infrastructure, reduction of oxidized monocarbon (C1) substrates, such as CO_2 and CO, is required. Though most current artificial

photosynthetic systems focus on the generation of H_2 and O_2 from water,[27-30] reduction of the products of combustion back to liquid hydrocarbons could also provide a pathway towards a carbon-neutral fuel cycle to reverse the effects of climate change in addition to storing clean solar energy.[31]

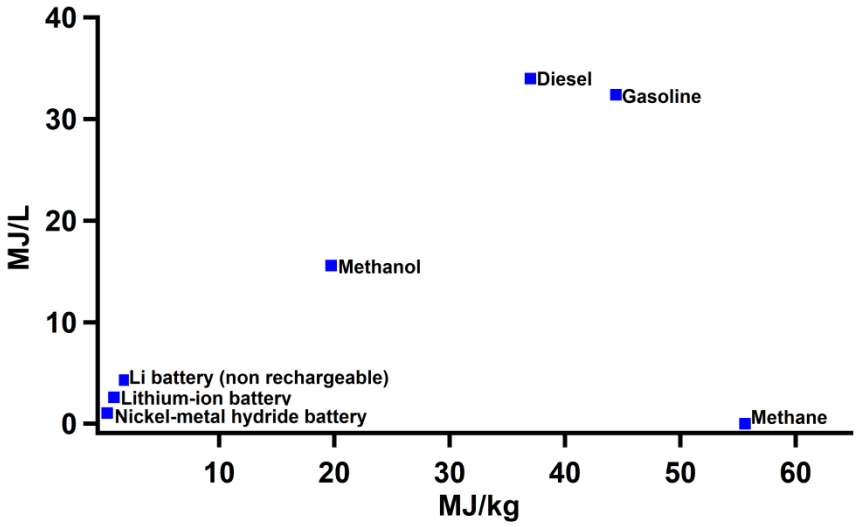

Figure 0.1: Selected energy densities of commercial battery technology, methanol, and fossil fuels

As seen in Figure 0.1, gasoline (C4-C12) and diesel (C9-C25) liquid hydrocarbon mixtures contain an order of magnitude greater energy density than current commercial battery technologies. Methane, the primary component of natural gas, contains more energy per mass than diesel and gasoline because it contains a higher density of C-H bonds, but due to its gaseous state contains very little energy per volume at standard temperature and pressure. Similarly, dihydrogen is the most energy dense compound per mass at 120 MJ/kg (not shown on graph), but possesses very poor energy per volume (< 0.1 MJ/L at STP) unless highly compressed.[26] Therefore liquid hydrocarbons are ideal synthetic fuel targets for renewable energy storage provided that the substrates used in their syntheses are oxidized C1 feedstocks.

There are several challenges that directly impact the formation of hydrocarbon fuels from C1 feedstocks. All fuel forming reactions from oxidized substrates are, by definition, endergonic and require energy input to proceed forward. Additionally, fuel forming reactions containing carbon monoxide and carbon dioxide as a substrate suffer from slow kinetics due to high transition state barriers activating their triple and double C-O bonds respectively.[24,32-34] To overcome kinetic barriers associated with CO_2 and CO reduction, heterogeneous and homogeneous catalysts have been developed.

The reduction of C1 substrates to liquid hydrocarbons was discovered in 1925[35] and has been industrially relevant since 1936 by the Fischer-Tropsch process (eq 2) using steam reformation of methane (eq 3) and the water-gas shift reactions (eq 4) as a source of CO and H_2 (synthesis gas).[36-38] All three processes require elevated temperatures and pressures as well as solid state transition metal catalysts in order to proceed. Transition metals suitable for commercial Fischer-Tropsch syntheses include Ru, Fe, and Co; however, Ir, Pt, and Pd have also demonstrated activity. Energy input is needed for generation of liquid fuels *via* the Fischer-Tropsch process, however unless that energy is derived from a renewable resource a carbon-neutral cycle is not established as the energy required to drive each reaction will come from a fossil fuel.

$$(2n+1)H_2 + nCO \longrightarrow C_nH_{(2n+2)} + nH_2O \quad (3)$$

$$CH_4 + H_2O \rightleftharpoons CO + 3H_2 \quad (4)$$

$$CO + H_2O \rightleftharpoons CO_2 + H_2 \quad (5)$$

For superior substrate and product selectivity as well as milder operating conditions, synthesis of hydrocarbon fuels would ideally be facilitated by a discrete well-defined homogenous catalyst. However, to date, other than the active site metallocofactors native to the nitrogenase enzymes (see Chapters 2 and 3),[39-44] there have not been any homogeneous catalysts

that can convert oxidized C1 substrates to C2+ hydrocarbons with similar product distribution to the Fischer-Tropsch process. Light driven conversion of carbon dioxide to methane has been achieved by an iron tetraphenylporphyrin complex functionalized with trimethylammonio groups,[22] however carbon-carbon coupling to higher order hydrocarbons is still a challenge for homogeneous systems.

0.2 Electrocatalysis and fuel forming reactions

In reactions with homogeneous transition metal catalysts, a reductant with a fixed reduction potential can be used to reduce the catalyst to its active form where it can deliver electrons to a substrate. However, reductants are not tuned exactly to the redox potentials of the catalyst nor are they efficiently regenerated. Ultimately use of reducing agents leads to an energy and atom inefficient process, generating chemical waste. Alternatively, electrochemistry can be used to directly transfer electrons to a catalyst from an electrode at the catalyst's reduction potential and utilize the solvent or an organic acid as the source of protons.[45,46]

In a simplified example of a reductive catalyst following an EC mechanism (an electrochemical step followed by a chemical step, Figure 0.2), the oxidized catalyst (cat^{ox}) would obtain the electrons necessary to reduce the catalyst's metal center (cat^{red}). Upon reduction cat^{red} can bind a substrate (i.e. CO_2 or CO). The substrate bound cat^{red} can transfer reducing equivalents into the substrate to convert it into product after subsequent reaction with protons. The oxidized catalyst releases the product and regenerates cat^{ox}.

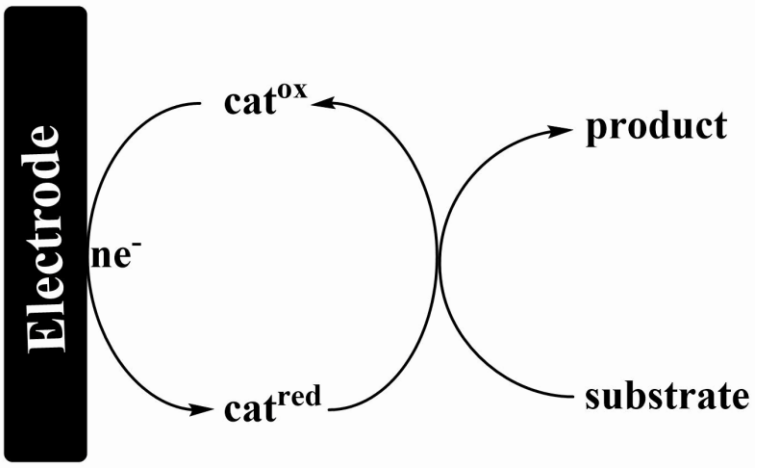

Figure 0.2: General example of a cathodic electrocatalytic reaction.

The two electron, two proton reduction of CO_2 to CO and water (eq 6) is an energy intensive process with a reduction potential of –0.53 V *vs.* NHE at pH 7 and 1 atmosphere pressure of CO_2.[32] The high energy transition states required for reduction makes the reaction

$$CO_2 + 2H^+ + 2e^- \longrightarrow CO + H_2O \quad E^{0'} = -0.53\ V \qquad (6)$$

kinetically inaccessible without an electrocatalyst that is able to coordinate the ensemble of CO_2, 2 protons, and 2 electrons. Additionally, the potential required to reduce electrocatalysts for CO_2 fixation is often far beyond the thermodynamic reduction potential of CO_2, leading to unwanted excess potential beyond the thermodynamic potential (overpotential) needed to drive the process. Development of homogeneous catalysts that can operate at low overpotentials and simultaneously produce hydrocarbon products of reduction from oxidized carbon substrates is pivotal to future energy storage needs.

0.3 Electrode supports and direct motivation for work

Photoelectrochemical cells are mediums in which sunlight can be absorbed by a photovoltaic material and generate chemical fuels.[47] Separation of holes and electrons at the photoabsorber to the anode and cathode of an electrochemical cell, respectively, can drive electrochemical reactions at the surface of each electrode. However, photoabsorbing semiconductors are not effective catalysts for the fuel forming reactions described above because they are not adequately selective or efficient; therefore strategies to create monolithic systems by adsorption of fuel-forming cocatalysts to these photoabsorbers must be explored.

Inorganic materials

The modification of electrode materials can provide for better selectivity at their surfaces during electrocatalytic processes. Solid state materials can be altered in their surface preparation as well as percent composition of various inorganic species (e.g. formation of alloys or inclusion of additives), but exact tuning and characterization of active site geometry and electronic properties are difficult, if not impossible, to achieve. Alternatively, adsorption of structurally and electronically well-defined molecular catalysts to electrode supports can allow for hybrid catalysts with the discrete specificity of a homogeneous catalyst and the structural stability of a heterogeneous catalyst.

Current methodology for deposition of solid state catalysts to surfaces include chemical vapor deposition, physical vapor deposition, dip coat, electrodeposition, spin coat, and various forms of sputter coating.[48-51] Homogeneous catalysts can be both chemisorbed (covalently attached) and physisorbed (non-covalently attached) to surfaces with varying success. Non-

covalent interactions such as π-π, electrostatic, and Van der Waals forces can be used to adhere molecules to surfaces. Chapter 1 of this thesis describes common problems associated with adsorption of molecular catalysts to surfaces and presents a study introducing a novel method demonstrating facile attachment of molecular species utilizing π-π interactions.

Enzyme bioelectrodes

Biological metalloenzymes such as CO dehydrogenase,[52,53] nitrogenase,[43] hydrogenase,[54] and methane monooxogenase,[55] are relevant model catalysts for synthetic fuels research because they are able to reduce target substrates to desirable reduced products at ambient temperatures, pressures, and pH while utilizing transition metal centers. Interfacing metalloenzymes with electrodes to perform their respective reactions electrocatalytically is currently a large field of study.[54,56-60] Chapter 2 describes a study electrochemically characterizing the isolated metallocofactors of the nitrogenase enzymes and Chapter 3 describes a study performing the electrocatalytic reduction of nitrogen (NO_2^- and N_3^-) and carbon substrates (CO and CO_2) to reduced products using nitrogenase enzymes on carbon electrodes with a polymer support.

0.4 References

(1) Lackner, M., Combustion Science and Technology, *Kirk-Othmer Encyclopedia of Chemical Technology*; Wiley & Sons, Posted October 14, 2011. https://onlinelibrary.wiley.com/doi/abs/10.1002/0471238961.0315130219080118.a01.pub2.

(2) *Monthly Energy Review: February 2019*; U.S. Dept. of Energy, Energy Information Administration: Washington, DC, 2019.

(3) McMichael, A. J.; Woodruff, R. E.; Hales, S. *Lancet* **2006**, *367*, 859.

(4) Parmesan, C.; Yohe, G. *Nature* **2003**, *421*, 37.

(5) Intergovernmental Panel on Climate, C. *Climate Change 2007 - Mitigation of Climate Change: Working Group III contribution to the Fourth Assessment Report of the IPCC*; Cambridge University Press: Cambridge, 2007.

(6) Kopp, G.; Lean, J. L. *Geophys. Res. Lett.* **2011**, *38*.

(7) Gay, C., F., Photovoltaic Cells, *Kirk-Othmer Encyclopedia of Chemical Technology*; Wiley & Sons, Posted December 4, 2009. https://onlinelibrary.wiley.com/doi/abs/10.1002/0471238961.16081520070125.a01.

(8) Shah, A.; Torres, P.; Tscharner, R.; Wyrsch, N.; Keppner, H. *Science* **1999**, *285*, 692.

(9) Hagfeldt, A.; Boschloo, G.; Sun, L.; Kloo, L.; Pettersson, H. *Chem. Rev.* **2010**, *110*, 6595.

(10) Li, G.; Zhu, R.; Yang, Y. *Nat. Photonics* **2012**, *6*, 153.

(11) Green, M. A.; Ho-Baillie, A.; Snaith, H. J. *Nat. Photonics* **2014**, *8*, 506.

(12) Haegel, N. M.; Margolis, R.; Buonassisi, T.; Feldman, D.; Froitzheim, A.; Garabedian, R.; Green, M.; Glunz, S.; Henning, H.-M.; Holder, B.; Kaizuka, I.; Kroposki, B.; Matsubara, K.; Niki, S.; Sakurai, K.; Schindler, R. A.; Tumas, W.; Weber, E. R.; Wilson, G.; Woodhouse, M.; Kurtz, S. *Science* **2017**, *356*, 141.

(13) Lewis, N. S.; Nocera, D. G. *Proc. Natl. Acad. Sci. U.S.A.* **2006**, *103*, 15729.

(14) Besenhard, J. O.; Eichinger, G. *J. Electroanal. Chem.* **1976**, *68*, 1.

(15) Besenhard, J. O.; Schöllhorn, R. *J. Power Sources* **1976**, *1*, 267.

(16) Cabana, J.; Monconduit, L.; Larcher, D.; Palacín, M. R. *Adv. Mater.* **2010**, *22*, E170.

(17) Dunn, B.; Kamath, H.; Tarascon, J.-M. *Science* **2011**, *334*, 928.

(18) Bradley, D. C.; Stillings, L. L.; Jaskula, B. W.; Munk, L.; McCauley, A. D., 2017, *Lithium, chap. K,* Schulz, K. J., DeYoung, J. J. H., Seal Ii, R. R., Bradley, D. C., eds., Critical mineral resources of the United States—Economic and environmental geology and prospects for future supply: U.S. Geological Survey Professional Paper 1802, K1, 10.3133/pp1802K.

(19) Etacheri, V.; Marom, R.; Elazari, R.; Salitra, G.; Aurbach, D. *Energy Environ. Sci.* **2011**, *4*, 3243.

(20) Tarascon, J. M.; Armand, M. *Nature* **2001**, *414*, 359.

(21) Pauling, L. *J. Am. Chem. Soc.* **1932**, *54*, 3570.

(22) Rao, H.; Schmidt, L. C.; Bonin, J.; Robert, M. *Nature* **2017**, *548*, 74.

(23) Raines, C. A. *Photosynth. Res.* **2003**, *75*, 1.

(24) Costentin, C.; Robert, M.; Savéant, J.-M. *Chem. Soc. Rev.* **2013**, *42*, 2423.

(25) Qiao, J.; Liu, Y.; Hong, F.; Zhang, J. *Chem. Soc. Rev.* **2014**, *43*, 631.

(26) *Proceedings of the 2000 U.S. DOE Hydrogen Program Review*; NREL/CP-570-28890; Energy, U. D. o.: San Ramon, CA, 2000.

(27) Bard, A. J.; Fox, M. A. *Acc. Chem. Res.* **1995**, *28*, 141.

(28) Gust, D.; Moore, T. A.; Moore, A. L. *Acc. Chem. Res.* **2009**, *42*, 1890.

(29) Kudo, A.; Miseki, Y. *Chem. Soc. Rev.* **2009**, *38*, 253.

(30) Nocera, D. G. *Acc. Chem. Res.* **2012**, *45*, 767.

(31) Olah, G. A.; Goeppert, A.; Prakash, G. K. S. *J. Org. Chem.* **2009**, *74*, 487.

(32) Benson, E. E.; Kubiak, C. P.; Sathrum, A. J.; Smieja, J. M. *Chem. Soc. Rev.* **2009**, *38*, 89.

(33) Gattrell, M.; Gupta, N.; Co, A. *J. Electroanal. Chem.* **2006**, *594*, 1.

(34) Chaplin, R. P. S.; Wragg, A. A. *J. Appl. Electrochem.* **2003**, *33*, 1107.

(35) Fischer, F.; Tropsch, H. Process for the production of paraffin-hydrocarbons with more than one carbon atom U.S. Patent 1,746,464, February 11, 1930.

(36) Khodakov, A. Y.; Chu, W.; Fongarland, P. *Chem. Rev.* **2007**, *107*, 1692.

(37) Leckel, D. *Energy Fuels* **2009**, *23*, 2342.

(38) Maitlis, P. M. *J. Organomet. Chem.* **2004**, *689*, 4366.

(39) Lee, C. C.; Hu, Y.; Ribbe, M. W. *Angew. Chem. Int. Ed.* **2012**, *51*, 1947.

(40) Lee, C. C.; Hu, Y.; Ribbe, M. W. *Angew. Chem. Int. Ed.* **2015**, *54*, 1219.

(41) Lee, C. C.; Tanifuji, K.; Newcomb, M.; Liedtke, J.; Hu, Y.; Ribbe, M. W. *ChemBioChem* **2018**, *19*, 649.

(42) Sickerman, N. S.; Tanifuji, K.; Lee, C. C.; Ohki, Y.; Tatsumi, K.; Ribbe, M. W.; Hu, Y. *J. Am. Chem. Soc.* **2017**, *139*, 603.

(43) Lee, C. C.; Hu, Y.; Ribbe, M. W. *Science* **2010**, *329*, 642.

(44) Rebelein, J. G.; Hu, Y.; Ribbe, M. W. *ChemBioChem* **2015**, *16*, 1993.

(45) Bard, A. J.; Faulkner, L. R. *Electrochemical Methods: Fundamentals and Applications*; 2 ed.; Wiley: New York, 2001.

(46) Saveant, J.-M. *Elements of Molecular and Biomolecular Electrochemistry: An Electrochemical Approach to Electron Transfer Chemistry*; John Wiley & Sons, Inc.: Hoboken, N. J., 2006

(47) Grätzel, M. *Nature* **2001**, *414*, 338.

(48) Serp, P.; Kalck, P.; Feurer, R. *Chem. Rev.* **2002**, *102*, 3085.

(49) Meille, V. *Appl. Catal. A-Gen.* **2006**, *315*, 1.

(50) Kim, D.-R.; Cho, K.-W.; Choi, Y.-I.; Park, C.-J. *Int. J. Hydrog. Energy* **2009**, *34*, 2622.

(51) Vukmirovic, M. B.; Bliznakov, S. T.; Sasaki, K.; Wang, J. X.; Adzic, R. R. *Interfaces* **2011**, *20*, 33.

(52) Jeoung, J.-H.; Dobbek, H. *Science* **2007**, *318*, 1461.

(53) Rakowski Dubois, M.; Dubois, D. L. *Acc. Chem. Res.* **2009**, *42*, 1974.

(54) Vincent, K. A.; Parkin, A.; Armstrong, F. A. *Chem. Rev.* **2007**, *107*, 4366.

(55) Merkx, M.; Kopp, D. A.; Sazinsky, M. H.; Blazyk, J. L.; Müller, J.; Lippard, S. J. *Angew. Chem. Int. Ed.* **2001**, *40*, 2782.

(56) Minteer, S. D.; Liaw, B. Y.; Cooney, M. J. *Curr.Opin. Biotech.* **2007**, *18*, 228.

(57) Meredith, M. T.; Minteer, S. D. *Annu. Rev. Anal. Chem.* **2012**, *5*, 157.

(58) Milton, R. D.; Hickey, D. P.; Abdellaoui, S.; Lim, K.; Wu, F.; Tan, B.; Minteer, S. D. *Chem. Sci.* **2015**, *6*, 4867.

(59) Armstrong, F. A.; Evans, R. M.; Hexter, S. V.; Murphy, B. J.; Roessler, M. M.; Wulff, P. *Acc. Chem. Res.* **2016**, *49*, 884.

(60) Evans, R. M.; Siritanaratkul, B.; Megarity, C. F.; Pandey, K.; Esterle, T. F.; Badiani, S.; Armstrong, F. A. *Chem. Soc. Rev.* **2019**.

Chapter 1

Methodology for Non-covalent Attachment of Molecular Species onto Electrode Surfaces

Portions of this Chapter have been published in:
Lydon, B. R.; Germann, A.; Yang, J. Y., *Inorg. Chem. Front*., **2016**, *3*, 836-841.

1.1 Introduction

Electrode surfaces modified with redox-active molecules have demonstrated significant utility in fundamental electron transfer studies and in the development of tailored electroresponsive materials.[1-8] These materials have been applied in chemical sensors, biochemical sensors,[10] and hybrid catalytic systems.[11] Hybrid catalytic systems are multicomponent assemblies containing a molecular catalyst affixed to a solid support. Hybrid systems permit reactions in media in which a molecular catalyst is not soluble, enabling facile recycling of molecular catalysts, and reduce issues of mass transport to an electrode in electrocatalytic systems.[11,12] Although heterogeneous bulk catalysts can be cheap and robust, they are not easily tuned for substrate/product specificity, and detailed mechanistic studies can be challenging. In contrast, the electronic properties and molecular geometry of molecular catalysts can be finely tuned *via* its ligands and studied by a large variety of spectroscopic methods for characterization and mechanistic studies.

Scheme 1.1: Depiction of an often unsuccessful method of covalently functionalizing surfaces with molecular complexes

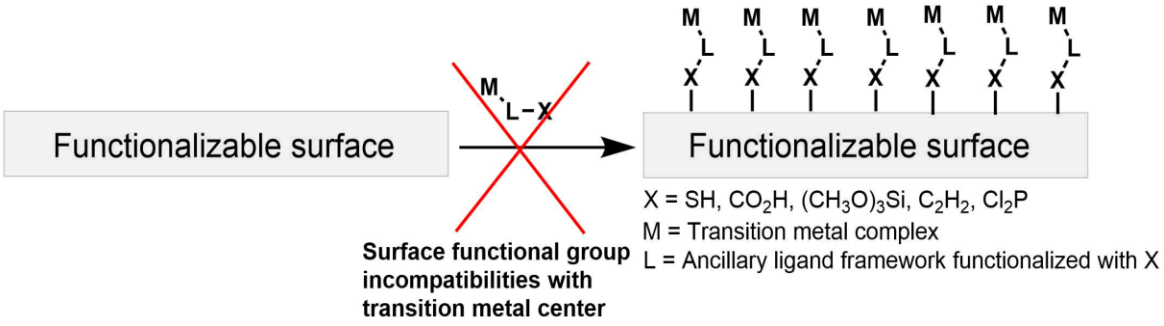

One method of accessing chemically modified electrodes is attachment of the target molecular complex to the surface via covalent bonds.[13-16] However, the reactive functional groups used to form covalent bonds to electrode surfaces (e.g. thiols to gold, or olefins, carboxylic acids, and phosphonic acids to metal oxides)[17] are often synthetically incompatible with molecular complexes containing open coordination sites or sensitive functional groups. The technical challenges inherent to this approach have limited the scope of molecular complexes that can be used for electrode surface modification. Scheme 1.1 outlines the nature of the problem. As mentioned above, the benefit of molecular catalysts is their ability to be electronically tuned, but if the ligands to effectively tune the complexes are not available due to the synthetic incompatibility with surface attachment then the desired molecular complex will either not be isolable or will lose its desired properties during the attachment process.

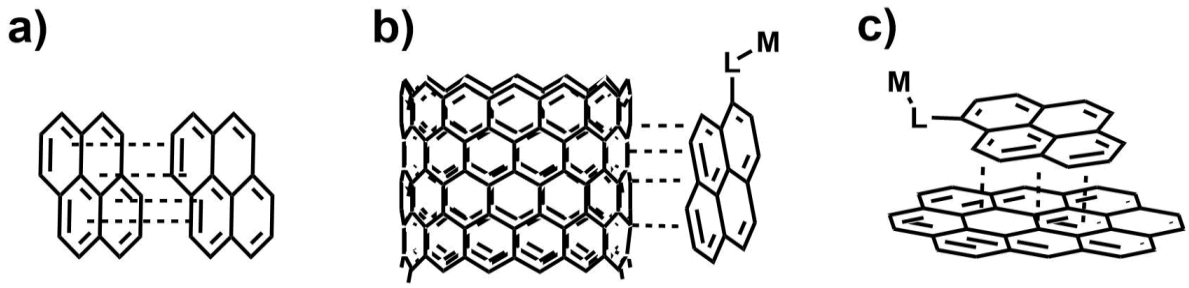

Figure 1.1: Example π-π interactions with pyrene a) intermolecularly with pyrene, b) pyrene-functionalized molecular complex and carbon nanotubes, and c) pyrene-functionalized molecular complex and graphene or graphite.

Pyrene, a polyaromatic hydrocarbon consisting of four fused benzene rings, can potentially be utilized towards a solution to the problems outlined in Scheme 1.1. Pyrene is known for its photochemical properties and aromatic conjugated π system forming π-π interactions.[18-22] The attractive quadrupolar interaction observed between two or more π systems containing a network of aromatic conjugated π bonds forms eximers that can be observed *via* fluorescence spectroscopy.[18] Although there is no theoretical consensus for the basis of π-π interactions,[23-26] their existence has been observed in both organic and biological systems.[27] Adsorption of molecules containing aromatic rings onto carbon electrodes was reported as early as 1976 when Brown et al. noted that two aromatic rings on *o*-dianisidine readily adsorbed onto a vitreous carbon electrode in a 1 M $HClO_4$ solution.[28] In that study, molecules with only one aromatic ring could not adsorb to the electrode surface, indicating the importance of a larger π-conjugated system for adsorption.

More recently, studies have focused on the physisorption of pyrene-functionalized molecular complexes to carbon nanotubes and graphitic electrodes (e.g. highly oriented pyrolytic graphite and graphene).[19,29-41] A visualization of this interaction is presented in Figure 1.1. Graphitic electrodes contain an array of sp^2 hybridized carbons in a hexagonal geometry imparting a relatively 'infinite' delocalized π system across the plane. This π network makes

graphic electrodes ideal surfaces to adsorb molecules using attractive π-π interactions. Additionally, the π-π interaction at the interface allows facile electron transfer between the electrode and molecular complexes.

Pyrene is relatively inert and insoluble in most solvents. However, it also maintains the same type of reactivity observed in typical aromatic systems, such as electrophilic aromatic substitution, allowing it to be functionalized at its open positions. Installation of pyrene on a broad range of molecular complexes and sensitive biological molecules with desirable catalytic, redox, or sensing properties has already been successful by LeGoff and others, which have then been physisorbed onto graphitic carbon electrodes.[32-39,41-47]

Electrocatalysts for synthetic fuel forming reactions would allow the conversion of intermittent renewable energy, which is typically generated in the form of electricity, into energy dense C-C, C-H, and H-H bonds. Molecular rhodium and iridium electrocatalysts for fuel forming reactions have been non-covalently affixed to pyrolytic graphite electrodes using pyrene linkers by Blakemore and Gray.[42] Importantly, in this study, it was shown that the catalytic function of the electrocatalysts remained unchanged after physisorption.

This approach of non-covalent attachment has been limited to modifying carbon-based electrodes with inherent aromatic character. Photovoltaic surfaces, which do not naturally contain aromatic character, would be the ideal source of electron flux upon illumination for fuel forming reactions. It would be beneficial to adapt this method of physisorption of an electrocatalyst by non-covalent interactions to non-graphitic surfaces in order to directly take solar flux from a solar absorber and convert it into product.

Scheme 1.2: Two step process for non-covalent attachment of transition metal complexes onto non-graphitic surfaces. 1) Functionalization of the surface with a pyrene-functionalized derivative. 2) non-covalent attachment of the transition metal compex modified with pyrene.

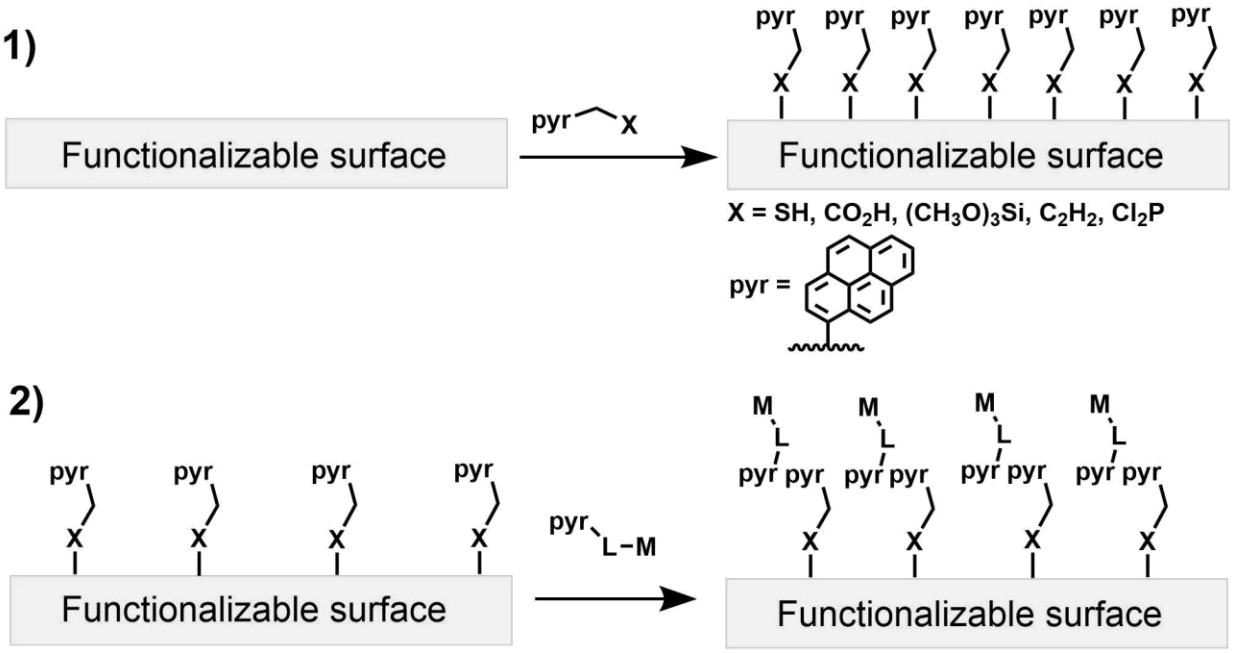

A general method for extending non-covalent physisorption of molecular complexes onto non-carbon electrodes is described. In the first step, a surface is pre-functionalized with covalently bound pyrene using the required functional groups for surface functionalization because they do not react with pyrene (Scheme 1.2.1). In the second step, pyrene-functionalized complexes exploit π-π interactions for physisorption onto the surface without having to interact with the reactive functional groups used in the first step (Scheme 1.2.2). Along with synthetic challenges, direct covalent attachment to each desired surface would require a new synthetic scheme for the ligand functionalization of the catalyst resulting in a monetarily and time expensive process. With this methodology, one molecular catalyst functionalized with pyrene could be physisorbed onto any pyrene-functionalizable surface.

As a proof of concept for the feasibility, stability, and facile electron transfer of this method of surface modification, a pyrene monolayer was established on a gold foil electrode.

Gold, a relatively inert metal towards oxidation was chosen due to its well-established sulfur self-assembled monolayer chemistry. A pyrene-functionalized ferrocene with well-defined redox properties was used to interrogate physisorption and electron transfer at the interface. The studies confirm that covalently bound pyrene can sufficiently alter the surface properties of the electrode to allow physisorption and electron transfer to pyrene-functionalized molecular complexes. This method represents a milder route to functionalize electrodes with sensitive molecular complexes, effectively expanding the scope of molecular species that can be used to modify non-carbon surfaces.

1.2 Results and Discussion

1.2.1 Synthesis and molecular characterization

1.2.1.1 S-(pyren-1-ylmethyl)ethanethioate

Scheme 1.3: Synthesis of *S*-(pyren-1-ylmethyl) ethanethioate **(1)**

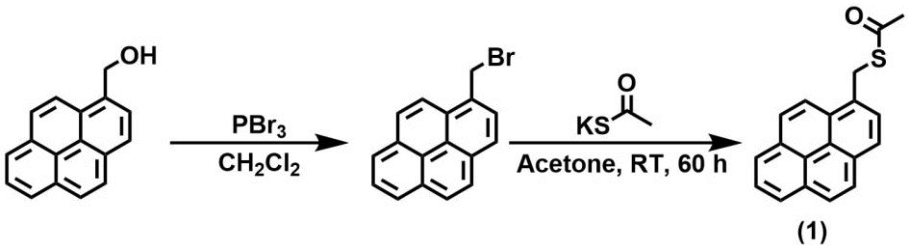

Initial attempts to synthesize a thiol-functionalized pyrene using established procedures were unsuccessful due to intermolecular disulfide linkages, evident in ^{1}H NMR spectroscopy, that prevented clean isolation of the product.[48] As a result, a strategy to protect the sulfide moiety until it could be covalently bonded to the gold electrode was employed. The thioacetate-functionalized pyrene, *S*-(pyren-1-ylmethyl) ethanethioate, (**1**) was ultimately synthesized.

Thioacetate derivatives have greater stability than their thiol counterparts because they are not prone to oxidation to form disulfides or sulfoxides, making them easier to isolate and purify.[49]

Compound **1** was formed by nucleophilic substitution of 1-bromomethylpyrene with potassium thioacetate in acetone and was characterized *via* ^{1}H NMR spectroscopy (Figure 1.2), ^{13}C NMR spectroscopy (Figure 1.3), and high-resolution mass spectrometry as described in the Experimental Section. ^{1}H NMR spectroscopy yielded a multiplet integrating to 9 protons between 8-8.2 ppm that is characteristic of resonances originating from pyrene. Additionally, only two other resonances were detected at 4.88 and 2.38 ppm representing the methylene and methyl protons, confirming high purity of the isolated compound. Fourier transform infrared (FTIR) spectroscopy for **1** displayed vibrational stretching frequencies at 3037, 2922, 2854 cm^{-1}, assigned as sp^2 C-H and sp^3 C-H stretches (Figure 1.4). The FT-infrared spectrum also had a resonance at 1686 cm^{-1} assigned to the C=O vibration. The thioacetate can be deprotected using a strong base (NH_4OH) *in situ* to form a covalent attachment to the surface.

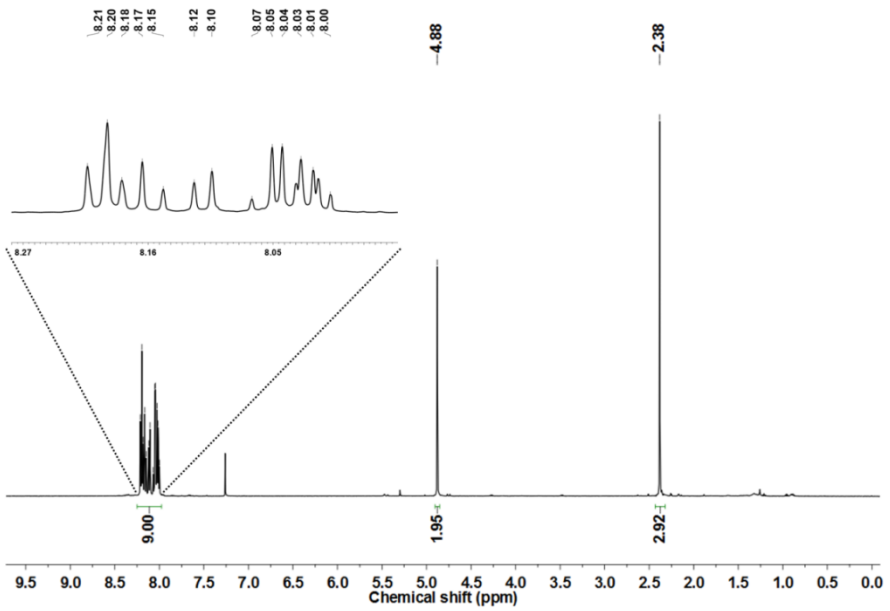

Figure 1.2: ^{1}H NMR spectrum of *S*-(pyren-1-ylmethyl) ethanethioate in $CDCl_3$

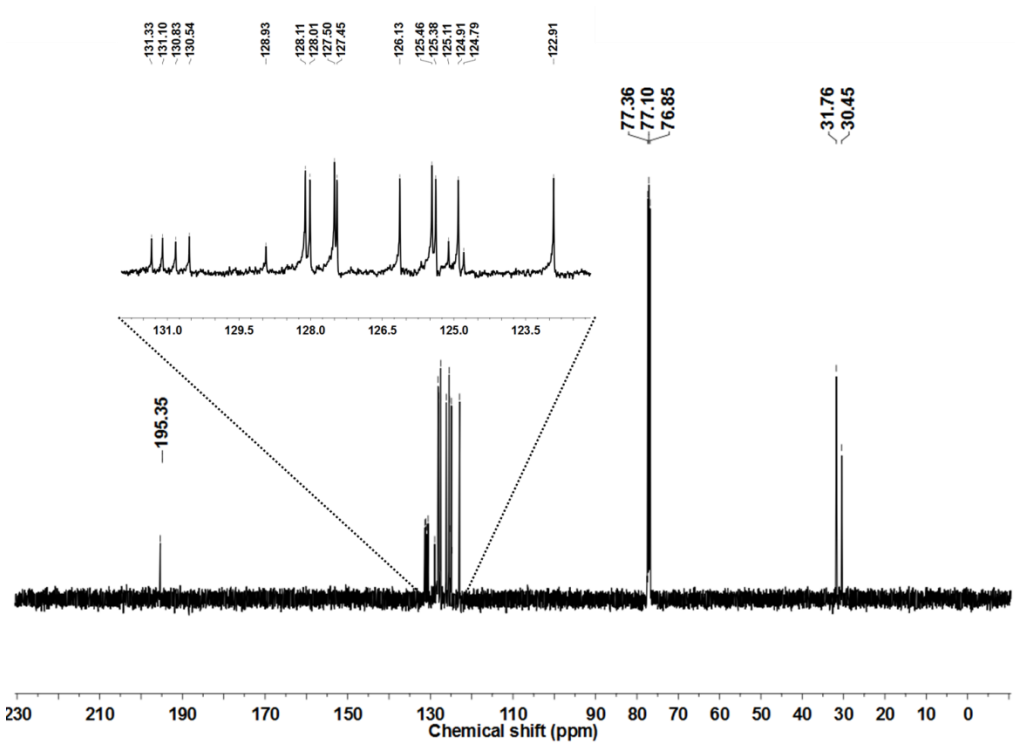

Figure 1.3: ^{13}C NMR spectrum of *S*-(pyren-1-ylmethyl) ethanethioate in $CDCl_3$

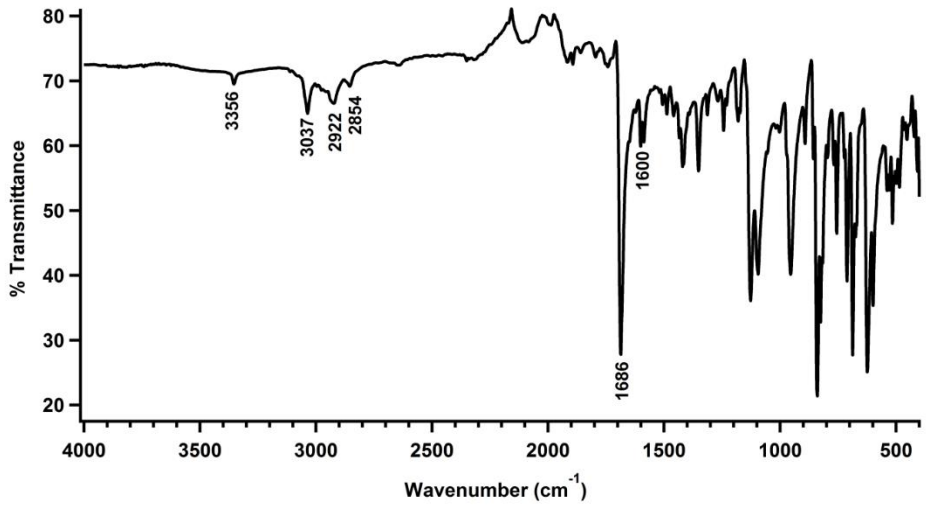

Figure 1.4: FTIR spectrum of *S*-(pyren-1-ylmethyl) ethanethioate

1.2.1.2 Syntheses of ferrocene-functionalized pyrenes

Ferrocene functionalized with pyrene was targeted as the electroactive marker for successful attachment onto a gold surface. As a proof of concept model for the methodology of physisorbing molecules onto surfaces, ferrocene is an ideal candidate for physisorption because modifying its cyclopentadiene rings is synthetically accessible, and its redox couple can be used as an electrochemical marker for surface attachment. Ferrocene is a known electrochemical standard with near ideal and reversible behavior.[9,50] The iron(II) center of ferrocene is coordinatively saturated, moderately inert, and can also be used as an iron marker in X-ray photoelectron spectroscopy for elemental identification. Initial synthetic strategies to form a pyrene-functionalized ferrocene involved using an amide linkage between the ferrocene and pyrene moieties. An amide bridge has been used in previous examples to covalently link pyrene to ancillary ligand backbones for attachment of rhodium bipyridine catalysts onto highly oriented pyrolytic graphite (HOPG) electrodes.[42]

Scheme 1.4: Synthesis of *N*-(pyren-1-ylmethyl)ferrocenyl-1-carboxamide

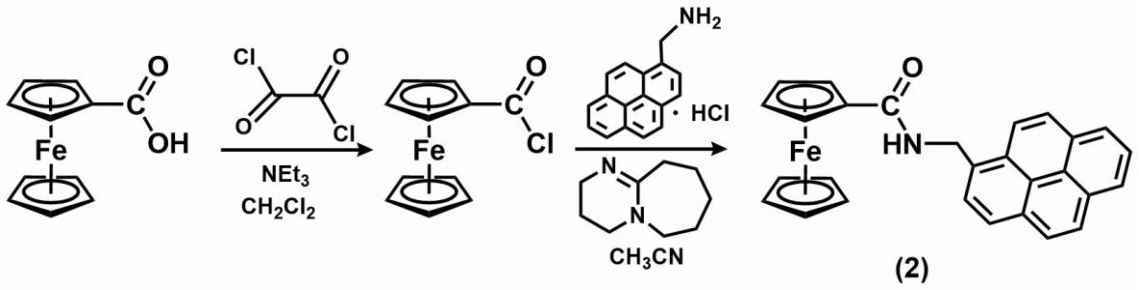

Synthesis of *N*-(pyren-1-ylmethyl)ferrocenyl-1-carboxamide (**2**) started with chlorination of ferrocenecarboxylic acid with oxalyl chloride to yield ferrocenoyl chloride as described previously.[51] Deprotonation of pyren-1-ylmethanamine hydrochloride with 1,8-diazabicyclo[5.4.0]undec-7-ene resulted in nucleophilic attack onto the carbonyl group with

subsequent release of HCl through a tetrahedral intermediate to yield the final product. ^{1}H NMR spectroscopy (Figure 1.5) verified the product through characteristic resonances for pyrenyl and ferrocenyl protons in addition to resonances for the amide and methylene protons within the linker.

Functionalization of the cyclopentadienyl rings of ferrocene with electron withdrawing or donating groups can alter the electronic properties of the ferrocenium/ferrocene redox couple by increasing or decreasing the electron donating ability of the rings. In most cases, however, the ferrocene typically retains its reversible nature. Cyclic voltammetry was performed on **2** (Figure 1.6) and the resulting voltammogram demonstrated similar electrochemical properties to ferrocene. Compound **2** exhibits one reversible couple at –189 mV *vs.* $Cp_2Fe^{+/0}$ with a peak-to-peak separation of 84 mV, approximately equal to the 86 mV peak-to-peak separation of the ferrocene internal standard.

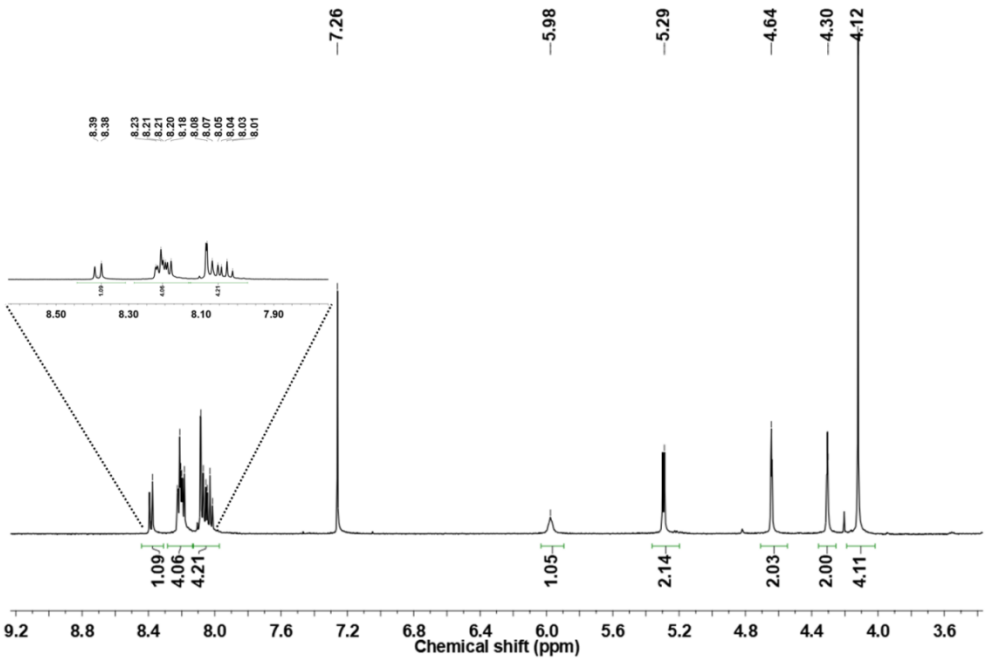

Figure 1.5: ^{1}H NMR spectrum of *N*-(pyren-1-ylmethyl)ferrocenyl-1-carboxamide in $CDCl_3$

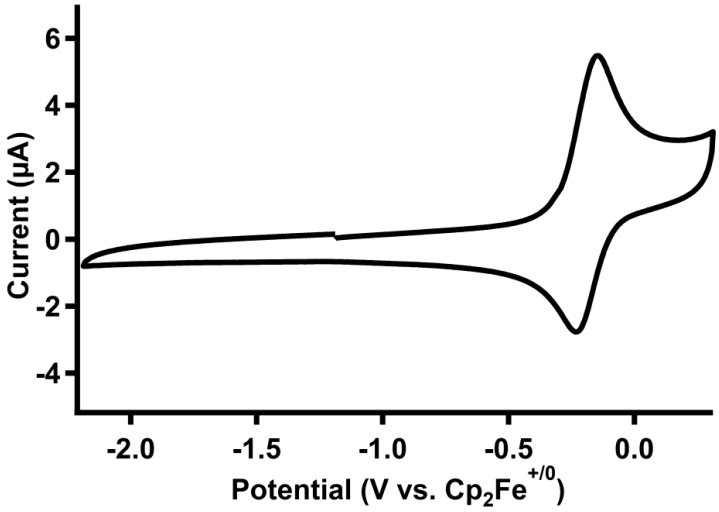

Figure 1.6: Cyclic voltammogram of *N*-(pyren-1-ylmethyl)ferrocenyl-1-carboxamide

Unfortunately, **2** is prone to gradual degradation in air as observed visually by color changes from orange to brown and formation of new peaks in the ^{1}H NMR spectrum over time. The products of the degradation were not determined, but the degradation is hypothesized to occur through either hydrolysis of the amide bond to regenerate the ferrocenecarboxylic acid starting material or oxidation of the benzylic position in the pyrene system because of the relative oxidative stability of the rest of the molecule. Because the surface analysis required for this project is performed after exposure to air and the electrochemistry is performed in acidic aqueous media in air it was necessary to reformulate the linkage between the ferrocene and the pyrene to protect the complex from oxidation.

Scheme 1.5: Synthesis of 1-pyrenylferrocene **(3)**

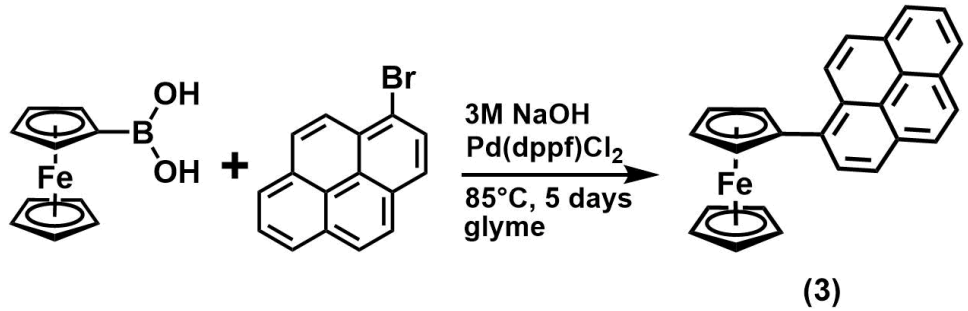

(3)

A direct covalent link between ferrocene and pyrene was achieved *via* Suzuki coupling between ferroceneboronic acid and 1-bromopyrene using [1,1′-bis(diphenylphosphino)ferrocene]dichloropalladium as the catalyst (Scheme 1.5). After isolation by column chromatography, the purity of the compound was verified by ^{1}H NMR spectroscopy, which produced characteristic resonances originating from pyrenyl and ferrocenyl protons between 8-9 ppm and 4-5 ppm at the proper integrations, respectively (Figure 1.7). ^{13}C NMR spectroscopy produced 20 resonances correlating to 20 unique carbon nuclei in the molecule (Figure 1.8).

FTIR spectroscopy of **3** (Figure 1.9) contains features consistent with both ferrocene and pyrene. The vibrational modes at 3091, 2924, and 1601 cm^{-1} correlate to the sp^2 C-H and sp^2 C-C stretches respectively from ferrocene. The remaining resonances in the organic region of the spectrum labeled in Figure 1.9 are consistent with pyrene. These spectra, as well as high resolution mass spectrometry, confirm the structure, isolation, and purity of **3**.

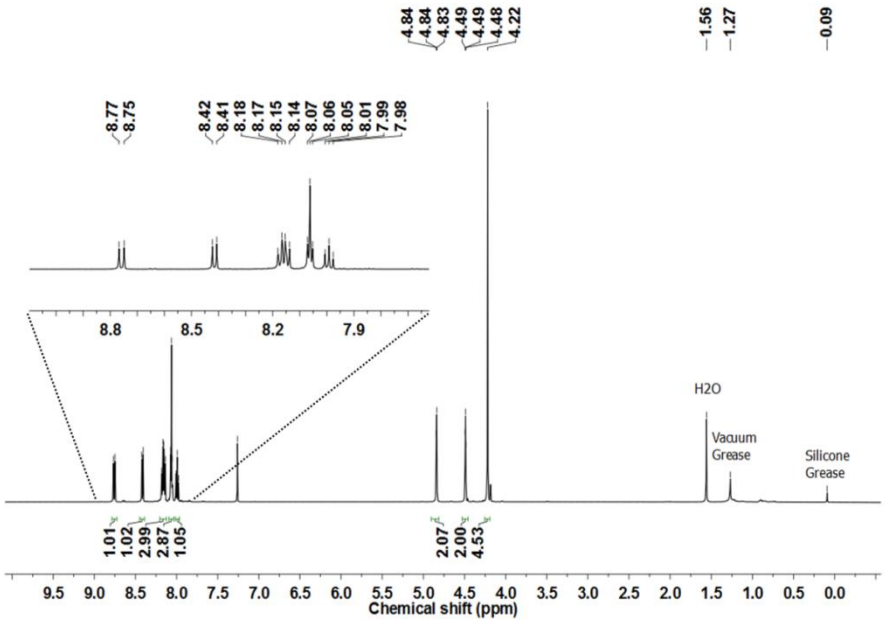

Figure 1.7: ^{1}H NMR spectrum of 1-pyrenylferrocene in $CDCl_3$

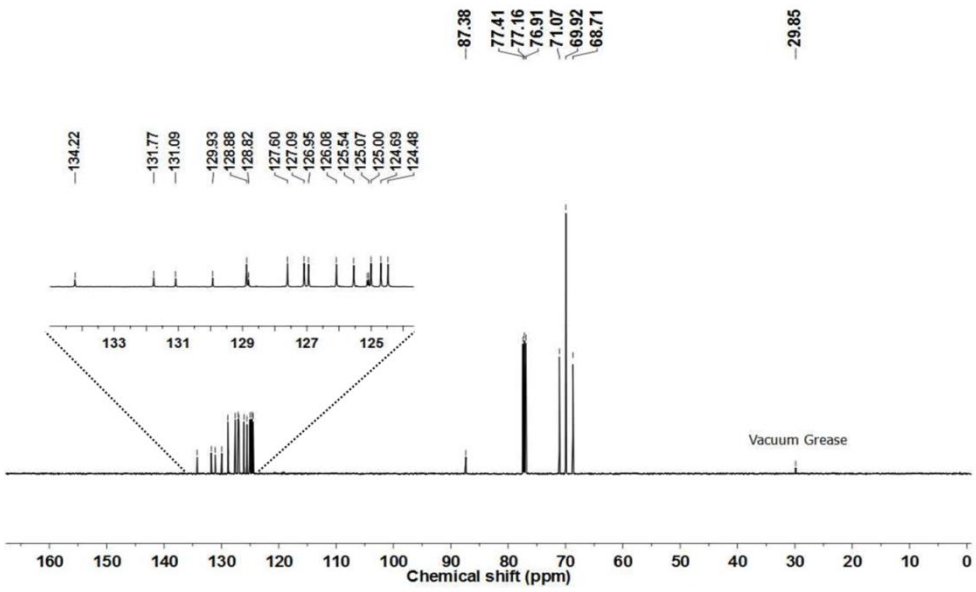

Figure 1.8: ^{13}C NMR spectrum of 1-pyrenylferrocene in $CDCl_3$

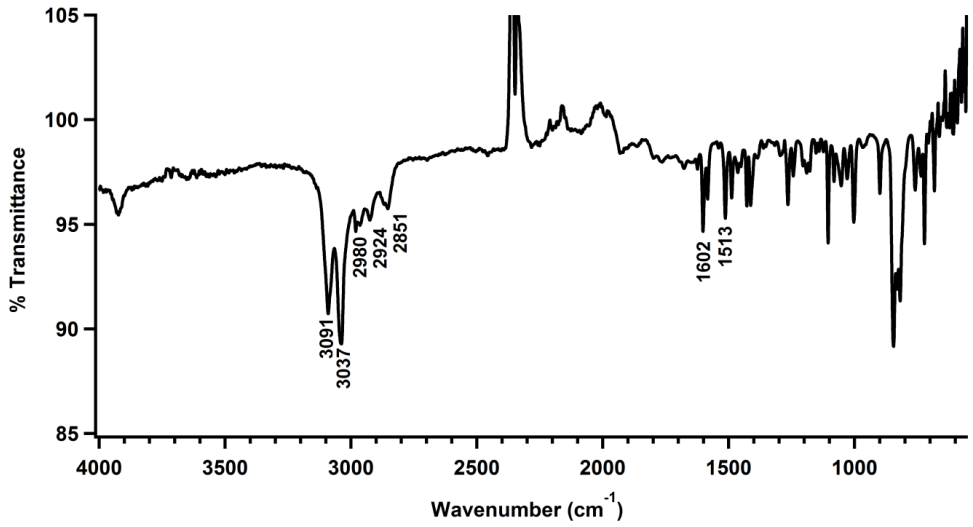

Figure 1.9: FTIR spectrum of 1-pyrenylferrocene. The stretch at 2300 - 2400 cm^{-1} is an artifact due to residual CO_2 trapped in the spectrometer. CO_2 is not present in the sample.

Similar to **2**, **3** was analyzed by cyclic voltammetry. The cyclic voltammogram of **3** has one reversible redox event at a nearly identical redox potential to ferrocene ($E_{1/2}$ = 0.055 V vs. $Cp_2Fe^{+/0}$), (Figure 1.10.a) indicating the pyrene functionality has a minimal effect on the ferrocenium/ferrocene redox couple. Scan rate dependent data of the cathodic and anodic peaks can be found in Figures 1.10.b and 1.10.c below. Plotting the peak anodic and cathodic currents versus the square root of the scan rate provides a linear trend indicating the analyte is freely diffusing in solution. The redox potential for 1-pyrenylferrocene is reversible and peak-to-peak separation of the anodic and cathodic waves is nearly ideal (~65 mV) at slow scan rates. As the scan rate is increased, the cathodic peak current decreases compared to the anodic peak current and begins to deviate away from unity, $|i_{pa}/i_{pc}| > 1$, but the peak-to-peak separation remains constant within 2 mV up to scan rates of 1000 mV/s. The deviation from unity for the peak current ratio could be due to the slight geometric rearrangement of the pyrene-functionalized ferrocene relative to ferrocene upon oxidation. Ferrocene exhibits an ideal $|i_{pa}/i_{pc}| = 1$ across the scan rates measured in acetonitrile. Cyclic voltammograms of 3 under homogeneous conditions

in acetonitrile displays a 1 e^- reversible couple. Due to the insolubility of 3 in aqueous media, we were unable to produce a similar homogeneous cyclic voltammogram in 0.1 M perchloric acid to compare to the redox event we observe after physisorption to the gold surface (*vide infra*).

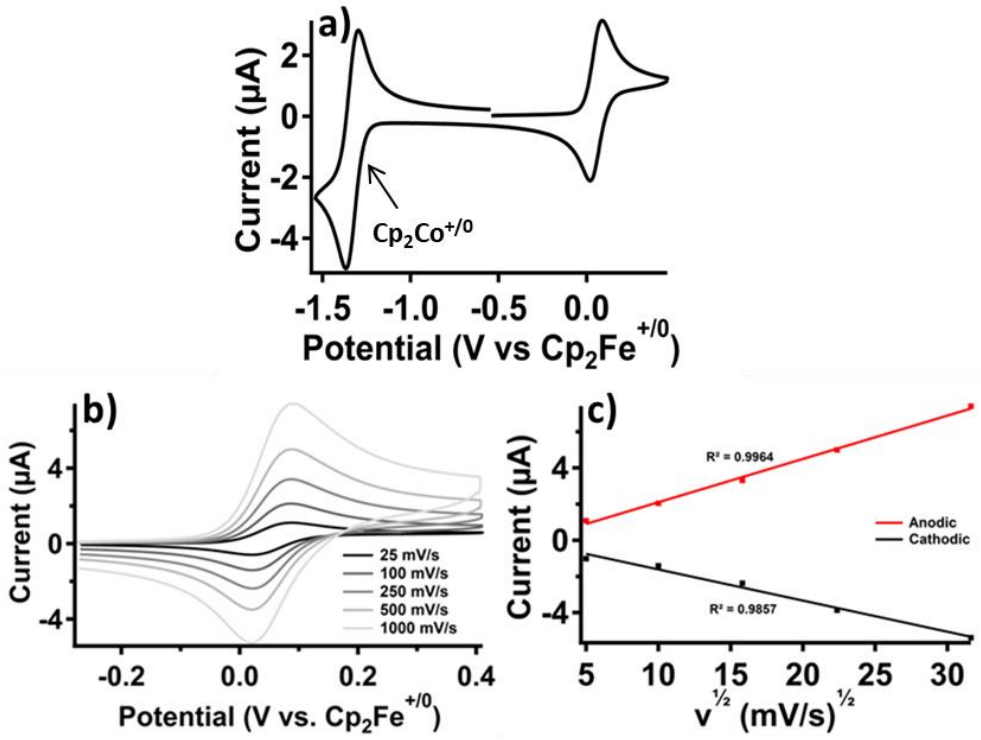

Figure 1.10: Cyclic voltammetry of 1-pyrenylferrocene (**3**) in CH_3CN ($E_{1/2}$ = 0.055 V vs. $Cp_2Fe^{+/0}$). a) Cyclic voltammogram at a scan rate of 100 mV/s with $[Cp_2Co][PF_6]$ internal reference. b) Variable scan rate cyclic voltammogram of the isolated redox couple of **3**. Scan rates varying from 25–1000 mV/s. c) Current vs. square root of the scan rate plot for anodic and cathodic peak currents indicating the analyte is freely diffusing in solution and not surface bound. 1 mM analyte in 0.1 M $[Bu_4N][PF_6]$ solution with an internal $[Cp_2Co][PF_6]$ reference. Glassy carbon working and auxiliary electrodes; Ag/Ag^+ pseudo-reference electrode. Potentials were measured against the cobatocene/cobaltocenium redox couple and then referenced to the ferrocene/ferrocenium redox couple (–1.33 V vs. $Cp_2Fe^{+/0}$) using previously reported values.[9] $[Cp_2Co][PF_6]$ was used as the internal standard because 1-pyrenylferrocene has an indistinguishable couple to ferrocene when measured together.

Table 1.1: Tabulated data regarding the isolated redox couple of 1-pyrenylferrocene in Figure 1.10.b

			Anodic wave		Cathodic wave			
Scan	v (mV/s)	√v $(mV/s)^{½}$	E_{pa} (V *vs.* $Cp_2Fe^{+/0}$)	i_{pa} (μA)	E_{pc} (V *vs.* $Cp_2Fe^{+/0}$)	i_{pc} (μA)	$\lvert i_{pa}/i_{pc} \rvert$	$E_{pa} - E_{pc}$ (mV)
1	25	5	87.9	1.082	22.1	-1.021	-1.060	65.8
2	100	10	86.6	2.042	23.4	-1.414	-1.444	63.2
3	250	15.811	87.8	3.313	22.2	-2.378	-1.393	65.6
4	500	22.361	88.6	4.998	21.4	-3.871	-1.291	67.2
5	1000	31.623	88.6	7.415	21.4	-5.394	-1.375	67.2

1.2.2 Electrode Surface Analysis by X-ray Photoelectron Spectroscopy

Each surface produced for this study was examined by X-ray photoelectron spectroscopy (XPS) and cyclic voltammetry. Additionally, some surfaces were also examined by attenuated total reflection (ATR) FTIR spectroscopy. XPS was used to determine the identity of elements present within 10 nm of the gold foil surface. There were four different conditions for surfaces that were prepared and analyzed: 1) unmodified gold substrate, 2) gold substrate functionalized with a monolayer of thiol-functionalized pyrene, 3) gold substrate functionalized with a monolayer of thiol-functionalized pyrene and **3**, and as a control 4) unmodified gold substrate *not* functionalized with a monolayer of pyrene and exposed to **3.**

1.2.2.1 Unmodified gold substrate

All gold substrates were subject to rigorous cleaning procedures prior to further experiments in order to remove any prior adsorbed organic and inorganic species. The cleaning procedure included electrochemically cycling a 1 cm^2 gold foil in 1 M H_2SO_4, followed by a boiling nitric acid bath, and solvent rinsing with electronic grade isopropanol and nanopure water

in conjunction with sonication. An unmodified gold substrate refers to a gold substrate that has undergone the cleaning procedure, but has not been otherwise chemically modified.

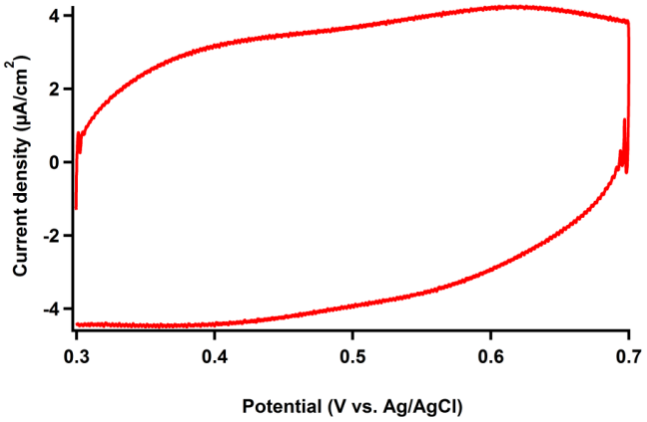

Figure 1.11: Cyclic voltammogram of an unmodified Au foil in an aqueous 0.1 M $HClO_4$ solution. Potentials measured versus a Ag/AgCl reference electrode in 1 M KCl. The 1 cm^2 Au substrate was used as the working electrode and glassy carbon as the auxiliary electrode.

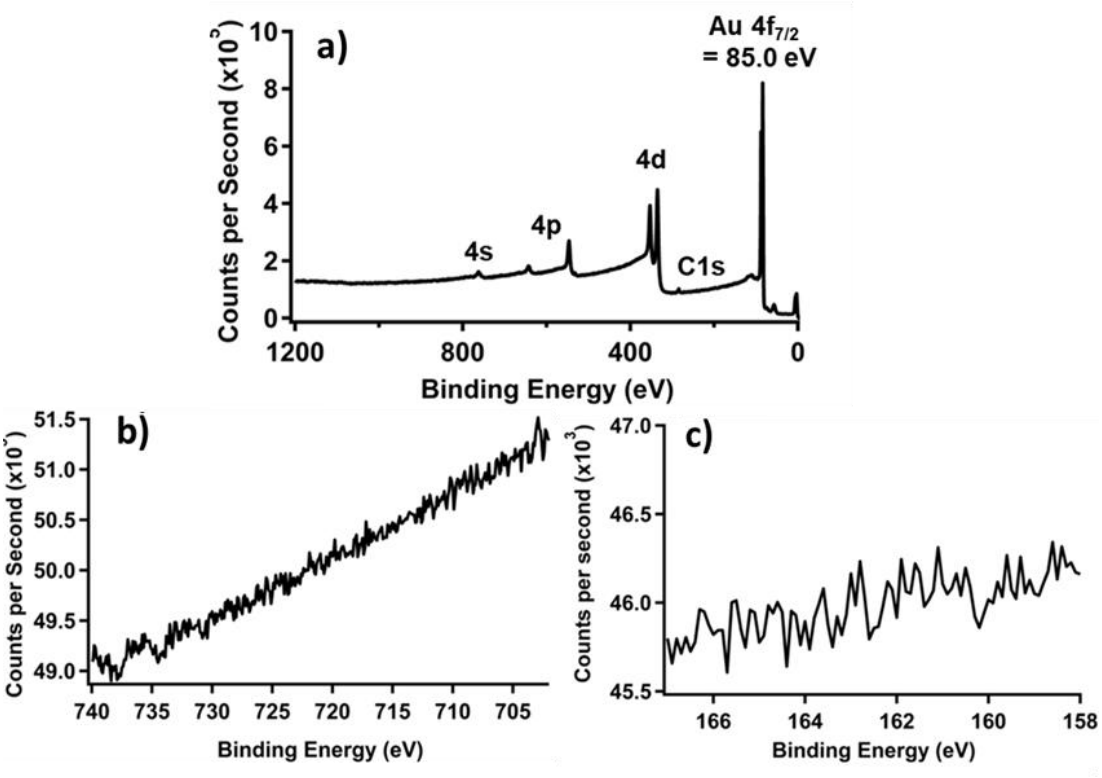

Figure 1.12: X-ray photoelectron spectroscopy of the unmodified gold substrate. a) Survey spectrum b) high resolution spectrum of the Fe 2p region, c) high resolution spectrum of the S 2p region of the spectrum.

Cyclic voltammetry of the unmodified gold substrate in 0.1 M $HClO_4$ produced no electrochemical signal beyond background capacitive current. The survey XP spectra of the unmodified gold substrate was predictable in that nothing other than peaks originating from gold were present with the $4f_{7/2}$, $4f_{5/2}$, $4d_{5/2}$, $4d_{3/2}$, $4p_{3/2}$, and $4s_{1/2}$ gold peaks all accounted for. One exception was a small amount of adventitious carbon detected through the C $1s_{1/2}$ peak in Figure 1.12.a. Additionally, high resolution XP spectra of the Fe 2p and S 2p regions (Figures 1.12.b and 1.12.c respectively) displayed only noise confirming that the surfaces of the unmodified gold substrates measured are free of those elements.

1.2.2.2 Sulfur monolayer formation

Scheme 1.6: Monolayer assembly and deprotection reaction of compound **1** onto gold

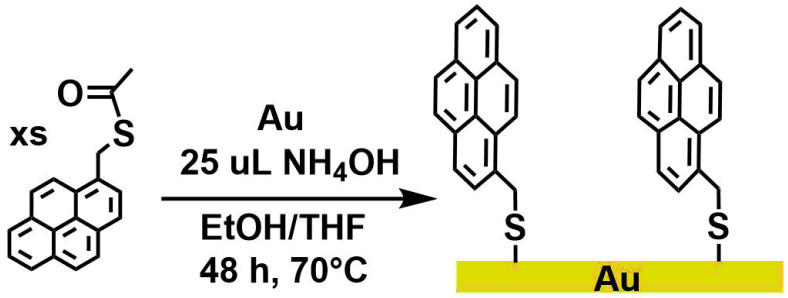

Deprotection of **1** *in situ* with ammonium hydroxide in an ethanol/tetrahydrofuran (THF) mixture resulted in formation of a thiol monolayer on the gold surface. Initial testing revealed that the deprotection reaction required a polar protic solvent, such as ethanol, to proceed. However, pyrene-functionalized molecules are notoriously insoluble in most solvents, including ethanol. Compound **1** is soluble in polar aprotic solvents such as THF. THF and ethanol are miscible, therefore a minimal amount of THF was added to the reaction until **1** was completely dissolved. Heating to 70°C without stirring over 48 hours resulted in formation of the pyrene monolayer.

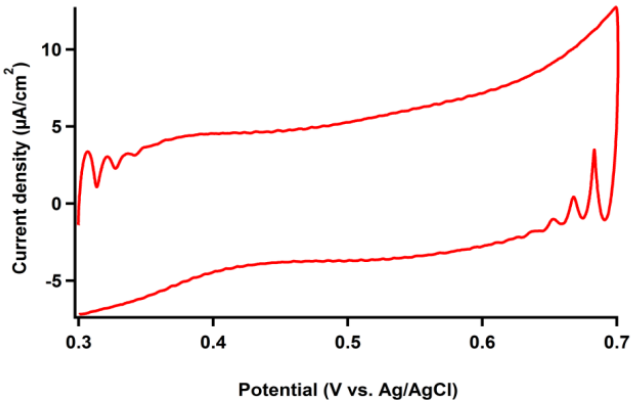

Figure 1.13: Cyclic voltammogram of a Au foil after pyrene-functionalization in an aqueous 0.1M $HClO_4$ solution. Potentials measured versus a Ag/AgCl reference electrode in 1 M KCl. The 1 cm^2 Au substrate was used as the working electrode and glassy carbon as the auxiliary electrode.

Cyclic voltammetry of the resulting gold surface seen in Figure 1.13 was featureless and displayed no redox couples within the window scanned. A rise in current is noted around 650 mV *vs*. Ag/AgCl. This rise in current is attributed to the initial oxidation of the thiol monolayer to remove it from of the surface. This feature is not seen the cyclic voltammogram of the unmodified gold surface. As a result, the electrochemical window was kept within 300-700 mV *vs*. Ag/AgCl during the course of this study.

XP spectra also showed no features in the Fe 2p (Figure 1.14.a) region with the exception of a broad peak consistent with the presence of Fe(III) oxide at approximately 715 eV. Fe_2O_3 is thought to have been acquired as an impurity in a solvent from the monolayer formation phase of the process, because all samples and controls that were not functionalized with **1** did not contain the Fe_2O_3 impurity. The green peaks in the S 2p (Figure 1.14.b) region at 162.2 and 163.8 eV were consistent with thiol covalently bound to gold, confirming the existence of the pyrene layer on the surface.[52] These features are also observed after treatment with pyrene-functionalized ferrocene, and are described in more detail below. The blue peaks in Figure 1.14.b are consistent

with a disulfide-bound gold species or other species that are not bound in the anticipated -S-Au mode.

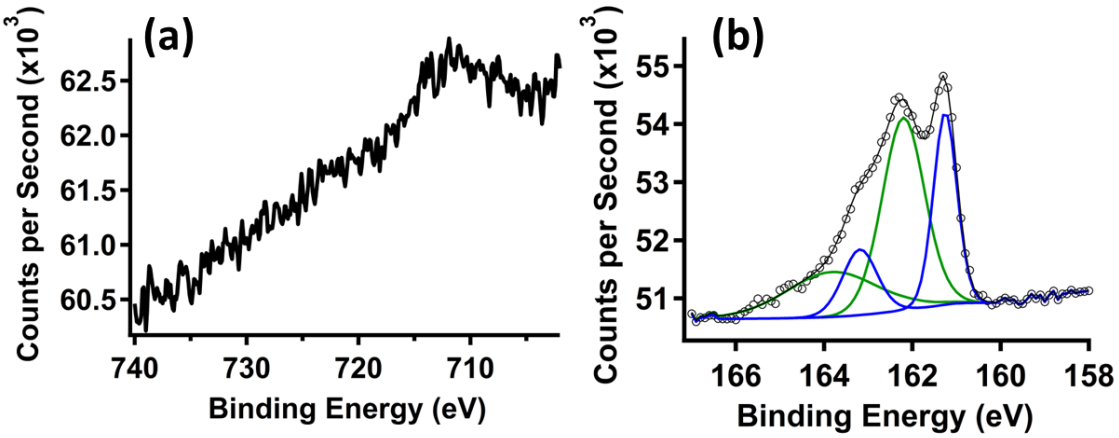

Figure 1.14: XP spectra of gold functionalized by a monolayer of the pyrene-functionalized thiol. a) high resolution spectrum of the Fe 2p region b) high resolution spectrum of the S 2p region.

1.2.2.3 Non-covalent attachment of 1-pyrenylferrocene to the pyrene-functionalized gold surface

Scheme 1.1: Non-covalent attachment of 1-pyrenylferrocene onto the pyrene-functionalized gold surface. This scheme does not depict any other potential Au-S binding modes that are suggested to be present via XPS such as Au-S-S-Au.

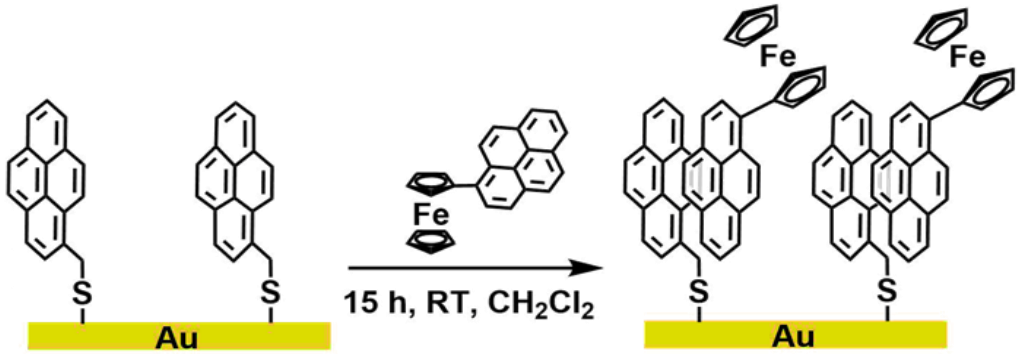

The gold substrate modified by covalent attachment of pyrene was soaked in a 1 mM solution of **3** in dichloromethane and rinsed with acetonitrile, a solvent in which **3** is also soluble. Rinsing with the acetonitrile is important because it allows for loosely bound species to be removed.

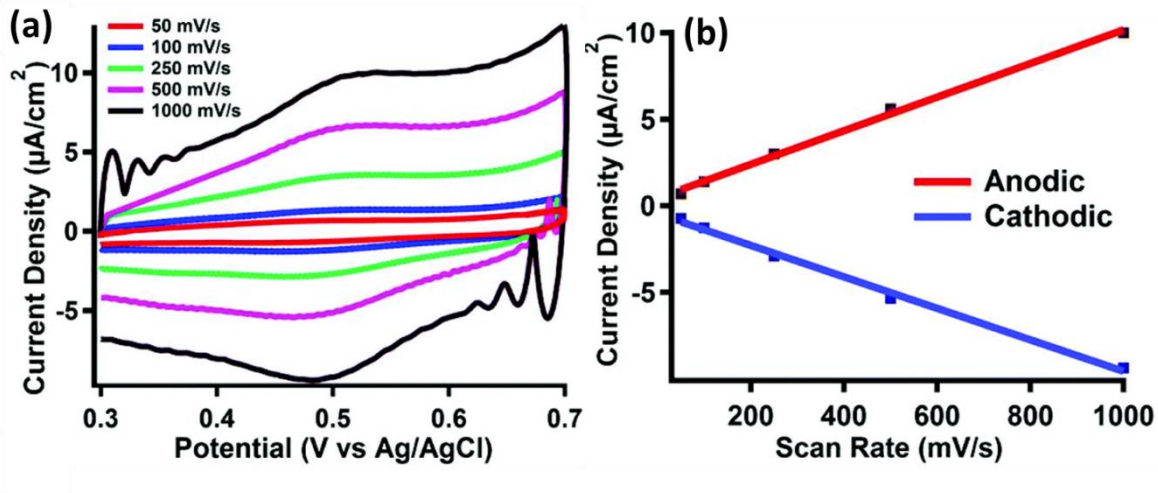

Figure 1.15: Electrochemical characterization of **3** non-covalently bound to a pyrene-modified gold surface. a) Variable scan rate cyclic voltammogram of a chemically modified gold working electrode in 0.1 M $HClO_4$ solution with Ag/AgCl reference and a glassy carbon auxiliary electrode. b) Current density vs. scan rate plot from the cyclic voltammogram in (a).

Table 1.2: Tabulated electrochemical data regarding the isolated redox peaks for **3** non-covalently bound to a pyrene-modified gold surface from Figure 1.15.

			Anodic wave		Cathodic wave			
Scan	v (mV/s)	$\sqrt{v}$ $(mV/s)^{½}$	E_{pa} (V vs. SHE)	i_{pa} (μA)	E_{pc} (V vs. SHE)	i_{pc} (μA)	$\lvert i_{pa}/i_{pc} \rvert$	$E_{pa} - E_{pc}$
1	50	7.07	507.6	0.69	442.9	-0.72	0.95	64.7
2	100	10.00	522.4	1.40	466.2	-1.28	1.09	56.1
3	250	15.81	505.8	3.00	478.3	-2.91	1.03	27.5
4	500	22.36	514.2	5.61	482.8	-5.35	1.05	31.4
5	1000	31.62	514.6	10.00	482.5	-9.39	1.07	32.1

A reversible couple is observed ($E_{1/2}$ = 495 mV, v = 100 mV/s, Figure 1.15.a) in the cyclic voltammograms of the modified electrodes. The $E_{1/2}$ value observed is consistent with similar reports of ferrocene species covalently bound to gold measured in aqueous solvents by Chidsey and coworkers.[53] The scan rate also displays a linear dependence on the peak anodic or cathodic current (Figure 1.15.b), indicating facile electron transfer to a surface-bound species. The full width at half-maximum (FWHM) of the anodic and cathodic waves are approximately

115 mV which deviates from the ideal value of 90 mV and suggests an intermolecular electrostatic interaction between neighboring ferrocenes at the surface.[53] Interestingly, there is a peak-to-peak separation ranging from 31 – 65 mV between the anodic and cathodic waves depending on scan rate (between 50 – 1000 mV/s, Table 1.2) that deviates from the ideal peak-to-peak separation of 0 V for a covalently surface bound species (versus 59 mV for a solution phase species). The deviation of the peak-to-peak separation is hypothesized to be due to either intermolecular interactions of **3** at the gold surface or electrostatic push/pull due to imbalance of surface and solution concentrations of ferrocene as seen previously with silicon electrodes.[53-54] Further experiments are required to probe the cause of this phenomenon.

The XP spectra for the chemically modified electrode are shown in Figure 1.16. The high resolution XP spectrum of the Fe 2p region in Figure 1.16.a displays two peaks at 707.6 and 720.3 eV, which correlate to the Fe $2p_{3/2}$ and Fe $2p_{1/2}$ emissions, respectively. These features are consistent with spectra taken of surfaces with covalently bound ferrocene.[55,56] A broad third peak is seen at 711.6 eV, attributed to the impurity acquired during the monolayer formation process described above (Figure 1.16.a).

The XP spectrum of the S 2p region is shown in Figure 1.16.b. A doublet in this spectrum was observed at binding energies of 161.2 and 162.2 eV. Modeling this doublet revealed two sets of doublets correlating to two different sulfur species. The doublet at binding energies of 162.2 eV and 163.4 eV, representing S $2p_{3/2}$ and $2p_{1/2}$ peaks respectively, and are consistent with sulfur species forming Au-S bonds.[52] The lower intensity doublet at 161.2 eV appears at roughly half the concentration of the covalently-bound thiol described above. The lower intensity doublet does not correlate to peaks that would result from X-ray damage, unbound thiol, or a gold metal sulfide. Another low intensity peak at 168.6 eV (not shown) is apparent in all samples, and is

attributed to a contaminant metal sulfate species that could not be removed from the surface through the cleaning procedure described. However the XPS data confirms that 1) the thiol-functionalized pyrene is covalently attached to the gold surface and 2) the pyrene-functionalized ferrocene is present on the surface.

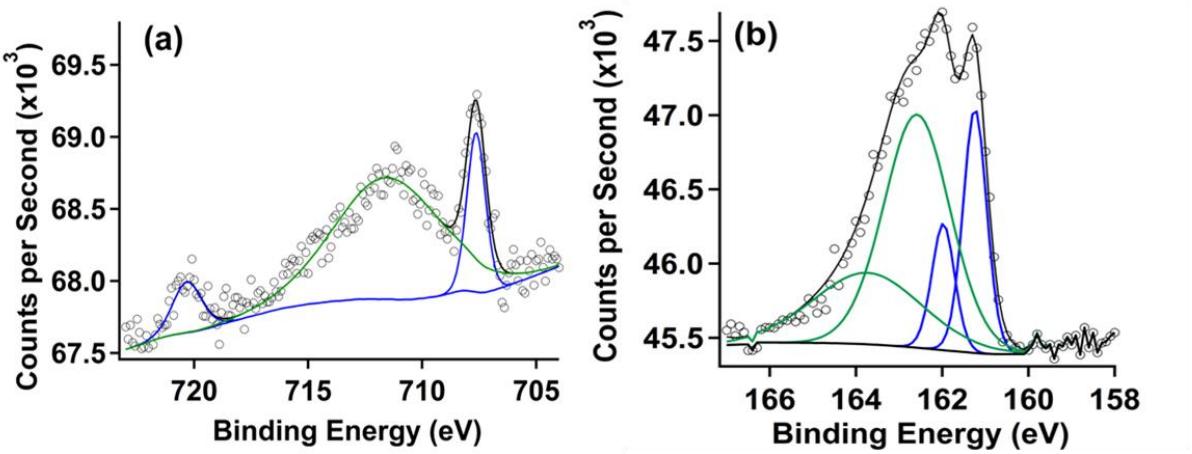

Figure 1.16: High resolution XP spectra of a gold surface functionalized with pyrene soaked in a 1 mM solution of **3** a) Fe 2p region b) S 2p region

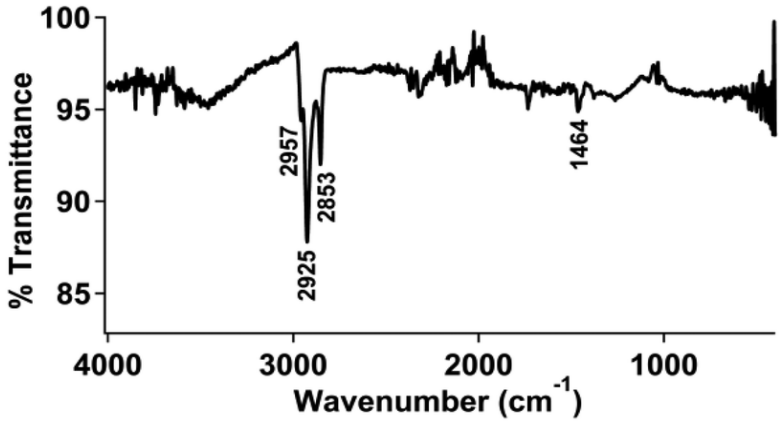

Figure 1.17: FTIR spectrum of a pyrene-modified gold electrode with **2** physisorbed to the Au surface.

ATR FTIR spectroscopy was used to probe for any organic vibrational stretching frequencies that may be present on the surface of the gold foil (Figure 1.17). The unmodified

gold substrate led to a featureless spectrum and was subsequently used as the background for future experiments. Upon addition of both **1** and **3,** stretching frequencies consistent with C-C and C-H bonds were observed at 2957, 2025, and 2853 cm^{-1}, further suggesting the presence of a surface bound species.

To confirm that physisorption of the pyrene-functionalized ferrocene is due to the presence of pyrene covalently attached to the gold surface, an unmodified gold substrate was also prepared and treated with **3** using the same procedure outlined in Scheme 1.7. A high resolution XP spectrum of the Fe 2p region (Figure 1.18.b) was featureless for both ferrocene as well as the Fe_2O_3 impurity seen in samples containing the pyrene monolayer. The vibrational spectrum of an unmodified gold substrate and an unmodified gold substrate exposed to **3** but not a pyrene monolayer further provides evidence that the latter is necessary for physisorption of **3** to the surface. The absence of **3** on the surface by XPS, and CV (Figure 1.18) indicates that **3** is washed off of the surface after solvent treatment when there is no pyrene covalently attached to the gold. The interaction between the pyrene at the surface and the pyrene functionalized on the ferrocene is sufficient to maintain physisorption to the surface, even after the acetonitrile wash.

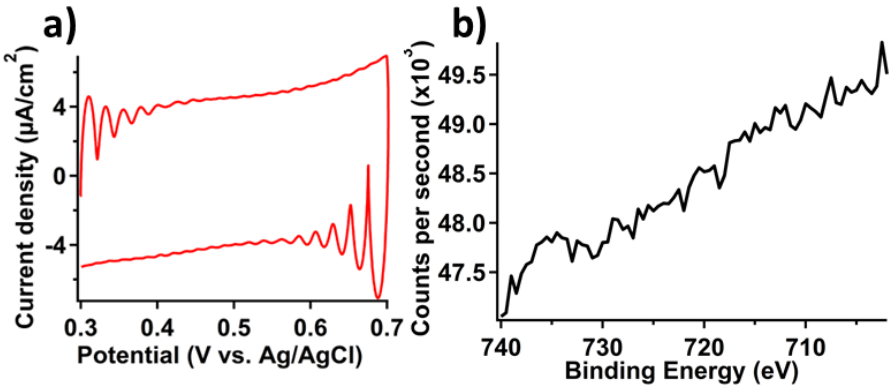

Figure 1.18: Characterization of an unmodified gold substrate exposed to a 1 mM solution of **3** and rinsed with acetonitrile. The pyrene-functionalized monolayer is not present on the sample. a) Cyclic voltammogram. The voltammogram was recorded in an aqueous 0.1 M $HClO_4$ solution. Potentials measured *versus* a Ag/AgCl reference electrode in 1 M KCl. The 1 cm^2 Au substrate was used as the working electrode and glassy carbon as the auxiliary electrode. b) High resolution XP spectrum of the Fe 2p region.

1.2.3 Surface coverage and stability experiments

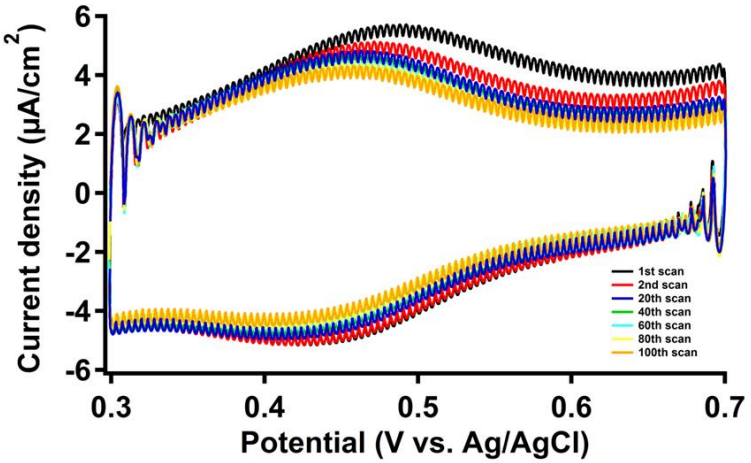

Figure 1.19: Cyclic voltammogram of a gold substrate functionalized with pyrene followed by exposure to **3**. 100 subsequent oxidation/reduction cycles were performed to probe redox stability of the π-π interactions between **3** and the surface. The voltammogram was recorded in an aqueous 0.1 M $HClO_4$ solution at 250 mV/s. Potentials were measured versus a Ag/AgCl reference electrode in 1 M KCl. The 1 cm^2 Au substrate was used as the working electrode and glassy carbon as the auxiliary electrode.

Table 1.3: Calculated surface concentrations (Γ) of **3** for oxidative (Γ_O) and reductive waves (Γ_R) for various scans from the voltammogram in Figure 1.19.

Scan #	Γ_O (pmol/cm^2)	Γ_R (pmol/cm^2)
1	17.1	8.8
2	16.8	7.5
20	16.6	9.6
40	19.8	10.4
60	13.9	8.7
80	15	9.1
100	17.5	8.4
Average	16.7	8.9
Standard deviation	1.9	0.9

Surface coverage of **3** was approximated in Microsoft Excel by manual integration *via* a left Riemann sum (> 4000 rectangles) of the faradaic current from the anodic wave with the assumption that 100% of the ferrocene at the surface of the electrode was oxidized. A baseline was manually established and non-faradaic current was subtracted from the current calculated.

The approximated faradaic current (i.e. non-capacitive current) divided by the scan rate provides the amount of coulombs or charge passed through the electrode to ferrocene. Dividing the resulting value by Faraday's constant (96,485 C/mol) provides the number of moles of electrons transferred. The oxidation of ferrocene to ferrocenium is a one electron process; therefore the moles of electrons transferred = the moles of ferrocene on the surface. Surface coverage was calculated between $\Gamma = 5 - 28$ pmol/cm^2 across all samples. The calculated surface coverage is low compared to the nmol/cm^2 theoretical maximum of a monolayer of **3** on a 1 cm^2 surface. The low coverage could be due to a suboptimal amount of the pyrene-thiol monolayer on the surface, which was noted to be lower than anticipated on gold in previous literature.[52] However, this prior study used a different procedure for formation of the monolayer and used the pyrene monolayer for intentional decomposition into carbon nanomembranes, unrelated to this study.

Redox stability of the non-covalent interaction at the surface of the electrode was analyzed via subsequent oxidation/reduction cycles (Figure 1.19). Experiments with up to 100 redox cycles did not show evidence for detachment of **3** measured by integration of the cathodic and anodic faradaic currents (Table 1.3) suggesting good stability of the π-π interactions under redox conditions in acidic media. Contrarily, visual analysis of Figure 1.19 shows a decrease in peak height with progressive scans. Given the manual nature of the methods described above used to calculate the area to determine faradaic current, there may be error associated with the values in Table 1.3 as it is possible that some amount of non-faradaic current may have been unintentionally included. However, it should be noted that every scan was treated systematically the same and errors involving the inclusion of non-faradaic current should be equally present for every scan.

1.3 Conclusions and current directions

The surface characterization studies demonstrate that modification of a gold electrode by covalent attachment of pyrene permits physisorption of a pyrene-functionalized ferrocene. Furthermore, the pyrene-functionalized ferrocene is stable on the surface even after washing with solvents in which the molecular species is soluble. The electrochemical studies demonstrate ideal reversible behavior for the ferrocene redox couple signifying that electron transfer through this interface is facile.

Since the aforementioned study on gold, there have been several advancements of note by Hanna and Yang.[57,58] This method has since been translated to indium tin oxide, a transparent semiconducting surface, where the surface was modified with vinylpyrene and subsequently non-covalently functionalized with 1-pyrenylferrocene, evident in XPS and cyclic voltammetry. Pyrene-pyrene π-π interactions were observed *via* fluorescence spectroscopy confirming the mode of interaction between the two moieties, and electron transfer kinetics studies verified facile electron transfer. Additionally, an organic anthraquinone was non-covalently bound to a pyrene-functionalized ITO surface to demonstrate proton coupled electron transfer properties were retained upon binding to the surface. These studies, in addition to the study described here on gold, strongly suggest that this method will be generally adaptable to other surfaces that can be functionalized with pyrene, and that molecules other than ferrocene can be immobilized.

1.4 Experimental Details

General Experimental Procedures

^{1}H NMR spectra were recorded on a Bruker CRYO500 (500 MHz) spectrometer at 20 °C. All ^{1}H chemical shifts have been internally calibrated to the monoprotio impurity of the deuterated solvent. ^{13}C NMR spectra were recorded on a Bruker CRYO500 (126 MHz) at 20 °C.

All heterogeneous electrochemical experiments were carried out in air in 0.1 M aqueous perchloric acid solutions with no further electrolyte added. Homogeneous experiments were carried out in a nitrogen filled glovebox in 1 mM analyte acetonitrile solutions containing 100 mM Bu_4NPF_6 as supporting electrolyte. Three electrode cyclic voltammetry experiments were performed using either a gold substrate (heterogeneous) or 1 mm diameter glassy carbon disk (homogeneous) working electrode, glassy carbon rod counter electrodes, and Ag/AgCl (heterogeneous, CH Instruments) or Ag/Ag^{+} pseudo reference (homogeneous, CH Instruments) with a Pine Wavedriver 10 potentiostat using Aftermath software. All potentials from heterogeneous experiments are referenced to Ag/AgCl and internal references for homogeneous experiments are noted in figure captions.

Electrospray ionization (ESI) mass spectra were collected using an ESI LC-TOF Micromass LCT. High resolution mass spectra were obtained from a Waters (Micromass) LCT premier #1.

Fourier transform infrared (FTIR) surface spectra of the gold electrodes and compound **1** were collected on a Jasco FTIR-4700 - ATR-PRO ONE in air. FTIR of molecular compound **2** was recorded on a Thermo Scientific Nicolet iS5 spectrometer with an iD5 ATR attachment in a nitrogen filled glovebox. Molecular samples were prepared by evaporating a dichloromethane solution of the sample onto the ATR crystal.

X-ray photoelectron spectra were acquired with a Kratos Analytical AXIS Supra spectrometer utilizing monochromatic Al Kα radiation (1486.7 eV, 250W) under ultra-high vacuum (UHV) conditions (~10^{-9} torr). The binding energies were referred to the Au $4f_{7/2}$ signal at 84.0 eV. Survey scans were used for elemental composition of the gold surface to demonstrate purity while high resolution region scans provided information on chemical shifts and position of peaks for specific elements. Spectral data was analyzed using Computer Aided Surface Analysis for X-ray Photoelectron Spectroscopy (CasaXPS). Shirley or linear backgrounds were used and Gaussian-Lorentzian lineshapes were used to model peaks. An offset Shirley background was required only for the Fe 2p XP spectrum shown in Figure 1.16.a.

Synthesis and Materials

All reactions and manipulations were performed under a nitrogen atmosphere using standard Schlenk techniques or a Vacuum Atmospheres glovebox unless otherwise indicated. Gold foil, 0.01 mm thickness, 99.9% pure, was purchased from Goodfellow. Solvents, with the exception of isopropanol and methanol, were dried using an activated alumina column. Water was purified by a Barnstead NANOpure ultrapure water system. All glassware was cleaned by immersion in concentrated chromic acid solution prepared using a literature procedure.[59] Sonication was performed in a SPER scientific ultrasonic cleaner (42 MHz). 1-(bromomethyl)pyrene[60] and ferrocenoyl chloride[51] were prepared using previously published procedures. All other chemicals were purchased and used without further purification.

Synthesis of Molecular Precursors

***S*-(pyren-1-ylmethyl) ethanethioate (1).** 1-bromomethylpyrene (295 mg, 1.00 mmol) was added to a vial with acetone (20 mL), forming a red suspension upon stirring. After addition of potassium thioacetate (137 mg, 1.20 mmol) in two portions, the suspension turned yellow. The resulting mixture was stirred for two days before the solvent was removed *in vacuo*. The solid was redissolved in dichoromethane and filtered through celite to remove a white solid impurity. The solvent was removed from the filtrate to furnish a light red solid, which was washed with pentane in order to isolate the light peach product (232 mg, 0.800 mmol, 80% yield). ^{1}H NMR (500 MHz, $CDCl_3$): δ = 2.38 (s, 3H, -C*H*$_3$), 4.88 (s, 2H, -C*H*$_2$-), 8.00-8.21(m, 9H, Pyr-*H*). ^{13}C NMR (126 MHz, $CDCl_3$): δ = 30.45, 31.76, 122.91, 124.79, 124.91, 125.11, 125.38, 125.46, 126.13, 127.45, 127.50, 128.01, 128.11, 128.93, 130.54, 130.83, 131.10, 131.33, 195.35. HR-MS: *m/z* calc. for $[C_{19}H_{14}OS]Na^{+}$: 313.0660; found: 313.0663.

***N*-(pyren-1-ylmethyl)ferrocenyl-1-carboxamide (2)**. Ferrocenoyl chloride (180 mg, 0.723 mmol) was added to a Schlenk flask (250 mL) equipped with a stirbar in MeCN (10 mL) and cooled to 0°C. In a separate flask, 1-pyrenemethylamine hydrochloride (199 mg, 0.744 mmol) was dissolved in MeCN (100 mL) after the addition of 1,8-diazabicycloundec-7-ene (0.43 mL, 2.88 mmol). The resulting solution was transferred via cannula to **1** forming a black mixture. The reaction was stirred overnight before solvent was removed *in vacuo*. The resulting black solid was washed with toluene to remove starting material and the black impurity was subsequently removed by silica gel column chromatography using 1:1 EtOAc:hexanes yielding the pure orange product. Yield: 210 mg, 0.48 mmol, 66%. ^{1}H NMR (500 MHz, DMSO-d6): δ = 8.52 (d, 1H, Ar-*H*); 8.50 (br, 1H, N-*H*); 8.28-8.24 (m, 4H, Ar-*H*)); 8.13-8.10 ppm (m, 3H, Ar-

H); 8.03 ppm (t, 1H, Ar-*H*); 5.11 ppm (d, C(O)NC*H*$_2$); 4.83 ppm (t, 2H, Cp-*H*); 4.31 ppm (t, 2H, Cp-*H*); 4.02 ppm (s, 5H, Cp-*H*). CV (Bu_4NBF_4 in MeCN): $E_{1/2}$, V *vs*. ferrocene (ΔEp, mV) = -0.19 (84); $\Delta Ep_{ferrocene}$ = 86 mV. ESI-MS *m/z*: 444.07 ($M\text{-}H^+$).

1-pyrenylferrocene (3). Ferroceneboronic acid (100 mg, 0.435 mmol), 1-bromopyrene (120 mg, 0.427 mmol), and Pd(dppf)Cl_2 • CH_2Cl_2 (32 mg, 0.044 mmol, 10 mol%) (dppf = 1,1'-bis(diphenylphosphino)ferrocene) were added to dimethoxyethane (8 mL) in a Schlenk tube charged with a stirbar. NaOH (1.2 g, 30 mmol) was added to the flask in H_2O (2 mL) to make a 10 mL, 3 M solution. The tube was sealed and heated at 85°C in an oil bath for 5 days. Dichloromethane was added to the resulting brown sludge, which was filtered through a silica plug to remove the residual catalyst and water. The resulting mixture was purified by column chromatography using *n*-hexane as the eluent, and the second fraction (red) was collected and the solvent removed *in vacuo*. The resulting solid was washed in cold *n*-hexane to yield the pure 1-pyrenylferrocene as a red/orange solid (30 mg, 0.08 mmol, 20% yield). ^{1}H NMR (500 MHz, $CDCl_3$): δ = 4.22 (s, 5H, C_5H_5), 4.49 (t, 2H, Cp-*H*), 4.84 (t, 2H, Cp-*H*), 7.99 (t, 1H, Pyr-*H*), 8.06 (t, 3H, Pyr-*H*), 8.16 (qd, 3H, Pyr-*H*), 8.41 (d, 1H, Pyr-*H*), 8.76 (d, 1H, Pyr-*H*). ^{13}C NMR (126 MHz, $CDCl_3$): δ = 68.71, 69.92, 71.07, 87.38, 124.48, 124.69, 125.00, 125.07, 125.12, 125.54, 126.08, 126.95, 127.09, 127.60, 128.82, 128.88, 129.93, 131.09, 131.77, 134.22. HR-MS: *m/z* calc. for [$C_{26}H_{18}Fe$]: 386.0758; found: 386.0764.

Preparation of Chemically Modified Gold Electrodes

All glassware used in the following preparations was cleaned in a concentrated chromic acid bath solution (chromerge) for at least 1 hour and then rinsed thoroughly with water before being dried in an oven.

Gold substrate preparation. In air, a square 1 cm^2 Au foil electrode was cleaned by electrochemical cycling between -0.3 V and 1.7 V in 1 M H_2SO_4. The foil was then boiled in nitric acid for 1 hour to remove organic residue and sequentially rinsed with water and electronic grade isopropanol (99.999%). The Au electrode was then sonicated for 15 minutes in water and re-rinsed with water and isopropanol.

Pyrene chemisorbed monolayer formation. Ethanol (2 mL) was added to *S*-(pyren-1-ylmethyl) ethanethioate (**1**) to make a suspension. Tetrahydrofuran was added drop-wise to the suspension until **1** was completely dissolved. The Au electrode was added to this solution along with 25 μL of 18 M aqueous NH_4OH. The sample heated to 70 °C under a nitrogen atmosphere for 48 hours. The Au electrode was then rinsed with dichloromethane and methanol before being dried in air under a stream of nitrogen.

Physisorption of pyrene-functionalized ferrocene. The pyrene functionalized Au electrodes were soaked in a 1 mM solution of **3** in dichloromethane (3 mL) for 48 hours. The Au was rinsed (5 x 2 mL) with acetonitrile and dried *in vacuo* for at least 1 hour before analysis.

1.5 References

(1) Murray, R. W. *Acc. Chem. Res.* **1980**, *13*, 135.

(2) Murray, R. W.; Ewing, A. G.; Durst, R. A. *Anal. Chem.* **1987**, *59*, 379A.

(3) Ulgut, B.; Abruña, H. D. *Chem. Rev.* **2008**, *108*, 2721.

(4) Bakker, E.; Qin, Y. *Anal. Chem.* **2006**, *78*, 3965.

(5) Chidsey, C. E. D. *Science* **1991**, *251*, 919.

(6) Amatore, C.; Maisonhaute, E.; Schöllhorn, B.; Wadhawan, J. *ChemPhysChem* **2007**, *8*, 1321.

(7) Sikes, H. D.; Smalley, J. F.; Dudek, S. P.; Cook, A. R.; Newton, M. D.; Chidsey, C. E. D.; Feldberg, S. W. *Science* **2001**, *291*, 1519.

(8) Richard, A. D.; Elmo, A. B. In *Fundamentals and Applications of Chemical Sensors*; American Chemical Society: 1986; Vol. 309, p 245.

(9) Connelly, N. G.; Geiger, W. E. *Chem. Rev.* **1996**, *96*, 877.

(10) Sirisha, V. L.; Jain, A.; Jain, A. In *Advances in Food and Nutrition Research*; Kim, S.-K., Toldrá, F., Eds.; Academic Press: 2016; Vol. 79, p 179.

(11) Ye, R.; Zhao, J.; Wickemeyer, B. B.; Toste, F. D.; Somorjai, G. A. *Nat. Catal.* **2018**, *1*, 318.

(12) Hartley, F. R. *Supported Metal Complexes: A New Generation of Catalysts*; D. Reidel: Dordrecht, 1985; Vol. 6.

(13) Schley, N. D.; Blakemore, J. D.; Subbaiyan, N. K.; Incarvito, C. D.; D'Souza, F.; Crabtree, R. H.; Brudvig, G. W. *J. Am. Chem. Soc.* **2011**, *133*, 10473.

(14) Collman, J. P.; Denisevich, P.; Konai, Y.; Marrocco, M.; Koval, C.; Anson, F. C. *J. Am. Chem. Soc.* **1980**, *102*, 6027.

(15) Yao, S. A.; Ruther, R. E.; Zhang, L.; Franking, R. A.; Hamers, R. J.; Berry, J. F. *J. Am. Chem. Soc.* **2012**, *134*, 15632.

(16) Krawicz, A.; Yang, J.; Anzenberg, E.; Yano, J.; Sharp, I. D.; Moore, G. F. *J. Am. Chem. Soc.* **2013**, *135*, 11861.

(17) Love, J. C.; Estroff, L. A.; Kriebel, J. K.; Nuzzo, R. G.; Whitesides, G. M. *Chem. Rev.* **2005**, *105*, 1103.

(18) Lakowicz, J. R. *Principles of Fluorescence Spectroscopy*; 3rd ed.; Plenum Press: New York, 1999.

(19) Lee, J.; Park, J. *Org. Lett.* **2015**, *17*, 3960.

(20) Yang, J.; Li, L.; Yu, Y.; Ren, Z.; Peng, Q.; Ye, S.; Li, Q.; Li, Z. *Mater. Chem. Front.* **2017**, *1*, 91.

(21) Förster, T.; Kasper, K. *Z. Phys. Chem.* **1954**, *1*, 275.

(22) Birks, J. B.; Christophorou, L. G. *Nature* **1962**, *196*, 33.

(23) Hunter, C. A.; Sanders, J. K. M. *J. Am. Chem. Soc.* **1990**, *112*, 5525.

(24) Rashkin, M. J.; Waters, M. L. *J. Am. Chem. Soc.* **2002**, *124*, 1860.

(25) Cockroft, S. L.; Perkins, J.; Zonta, C.; Adams, H.; Spey, S. E.; Low, C. M. R.; Vinter, J. G.; Lawson, K. R.; Urch, C. J.; Hunter, C. A. *Org. Biomol. Chem.* **2007**, *5*, 1062.

(26) Wheeler, S. E.; Houk, K. N. *J. Am. Chem. Soc.* **2008**, *130*, 10854.

(27) Kataev, E. A.; Shumilova, T. A.; Fiedler, B.; Anacker, T.; Friedrich, J. *J. Org. Chem.* **2016**, *81*, 6505.

(28) Brown, A. P.; Koval, C.; Anson, F. C. *J. Electroanal. Chem.* **1976**, *72*, 379.

(29) Zhang, Y.; Liu, C.; Shi, W.; Wang, Z.; Dai, L.; Zhang, X. *Langmuir* **2007**, *23*, 7911.

(30) Udit, A. K.; Hill, M. G.; Bittner, V. G.; Arnold, F. H.; Gray, H. B. *J. Am. Chem. Soc.* **2004**, *126*, 10218.

(31) Ehli, C.; Rahman, G. M. A.; Jux, N.; Balbinot, D.; Guldi, D. M.; Paolucci, F.; Marcaccio, M.; Paolucci, D.; Melle-Franco, M.; Zerbetto, F.; Campidelli, S.; Prato, M. *J. Am. Chem. Soc.* **2006**, *128*, 11222.

(32) Liu, J.; Bibari, O.; Mailley, P.; Dijon, J.; Rouviere, E.; Sauter-Starace, F.; Caillat, P.; Vinet, F.; Marchand, G. *New J. Chem.* **2009**, *33*, 1017.

(33) Bartelmess, J.; Ballesteros, B.; de la Torre, G.; Kiessling, D.; Campidelli, S.; Prato, M.; Torres, T.; Guldi, D. M. *J. Am. Chem. Soc.* **2010**, *132*, 16202.

(34) Mhaske, S. D.; Ray, M.; Mazumdar, S. *Inorg. Chim. Acta* **2010**, *363*, 2804.

(35) Tran, P. D.; Le Goff, A.; Heidkamp, J.; Jousselme, B.; Guillet, N.; Palacin, S.; Dau, H.; Fontecave, M.; Artero, V. *Angew. Chem. Int. Ed.* **2011**, *50*, 1371.

(36) Le Goff, A.; Gorgy, K.; Holzinger, M.; Haddad, R.; Zimmerman, M.; Cosnier, S. *Chem. Eur. J.* **2011**, *17*, 10216.

(37) Ding, S.-N.; Shan, D.; Cosnier, S.; Le Goff, A. *Chem.-Eur. J.* **2012**, *18*, 11564.

(38) Le Goff, A.; Reuillard, B.; Cosnier, S. *Langmuir* **2013**, *29*, 8736.

(39) Walgama, C.; Krishnan, S. *J. Electrochem. Soc.* **2014**, *161*, H47.

(40) Sabater, S.; Mata, J. A.; Peris, E. *Organometallics* **2015**, *34*, 1186.

(41) Navaee, A.; Salimi, A. *J. Mater. Chem. A*, **2015**, *3*, 7623.

(42) Blakemore, J. D.; Gupta, A.; Warren, J. J.; Brunschwig, B. S.; Gray, H. B. *J. Am. Chem. Soc.* **2013**, *135*, 18288.

(43) Yang, L.; Ozawa, H.; Koumoto, M.; Yoshikawa, K.; Matsunaga, M.; Haga, M.-a. *Chem. Lett.* **2015**, *44*, 160.

(44) Kong, N.; Gooding, J. J.; Liu, J. *J. Solid State Electrochem.* **2014**, *18*, 3379.

(45) Reuillard, B.; Le Goff, A.; Cosnier, S. *Chem. Commun.* **2014**, *50*, 11731.

(46) Lalaoui, N.; Elouarzaki, K.; Goff, A. L.; Holzinger, M.; Cosnier, S. *Chem. Commun.* **2013**, *49*, 9281.

(47) Parra, E. J.; Rius, F. X.; Blondeau, P. *Analyst* **2013**, *138*, 2698.

(48) Ipe, B. I.; Thomas, K. G. *J. Phys. Chem. B* **2004**, *108*, 13265.

(49) Tour, J. M.; Jones, L.; Pearson, D. L.; Lamba, J. J. S.; Burgin, T. P.; Whitesides, G. M.; Allara, D. L.; Parikh, A. N.; Atre, S. *J. Am. Chem. Soc.* **1995**, *117*, 9529.

(50) Gritzner, G.; Kuta, J. In *Pure and Applied Chemistry* 1984; Vol. 56, p 461.

(51) C. Grossel, M.; G. Hamilton, D.; I. Fuller, J.; Millan-Barios, E. *J. Chem. Soc., Dalton Trans.* **1997**, 3471.

(52) Angelova, P.; Vieker, H.; Weber, N.-E.; Matei, D.; Reimer, O.; Meier, I.; Kurasch, S.; Biskupek, J.; Lorbach, D.; Wunderlich, K.; Chen, L.; Terfort, A.; Klapper, M.; Müllen, K.; Kaiser, U.; Gölzhäuser, A.; Turchanin, A. *ACS Nano* **2013**, *7*, 6489.

(53) Chidsey, C. E. D.; Bertozzi, C. R.; Putvinski, T. M.; Mujsce, A. M. *J. Am. Chem. Soc.* **1990**, *112*, 4301.

(54) Vogel, Y. B.; Zhang, L.; Darwish, N.; Gonçales, V. R.; Le Brun, A.; Gooding, J. J.; Molina, A.; Wallace, G. G.; Coote, M. L.; Gonzalez, J.; Ciampi, S. *Nature Communications* **2017**, *8*, 2066.

(55) Trasobares, J.; Vaurette, F.; François, M.; Romijn, H.; Codron, J.-L.; Vuillaume, D.; Théron, D.; Clément, N. *Beilstein J. Nanotechnol.* **2014**, *5*, 1918.

(56) Méndez De Leo, L. P.; de la Llave, E.; Scherlis, D.; Williams, F. J. *J. Chem. Phys.* **2013**, *138*, 114707.

(57) Hanna, C. M.; Sanborn, C. D.; Ardo, S.; Yang, J. Y. *ACS Appl. Mater. Interfaces* **2018**, *10*, 13211.

(58) Hanna, C. M.; Luu, A.; Yang, J. Y. *ACS Appl. Energy Mater.* **2019**, *2*, 59.

(59) Birch, W.; Carré, A.; Mittal, K. L. In *Developments in Surface Contamination and Cleaning*; Mittal, R. K. L., Ed.; William Andrew Publishing: Norwich, NY, 2008, p 693.

(60) Bartels, J. L.; Lu, P.; Walker, A.; Maurer, K.; Moeller, K. D. *Chem. Commun.* **2009**, 5573.

Chapter 2

Electrochemical characterization of isolated nitrogenase cofactors from *Azotobacter vinelandii*

Portions of this chapter have been submitted for publication.

This work was performed in collaboration with Professors Markus Ribbe and Yilin Hu. Dr. Chi Chung Lee, Dr. Kazuki Tanifuji, Dr. Nathaniel Sickerman, and Megan Newcomb prepared, isolated, and performed biochemical assays for the nitrogenase cofactors used in this study.

2.1 Introduction

Nitrogenase is a unique metalloenzyme system found in bacteria that catalyzes the reduction of dinitrogen (N_2) to ammonia (NH_3).[1] Of the three variants of nitrogenases known thus far, the most well-characterized is the molybdenum nitrogenase, which consists of a reductase component, NifH (*nifH*-encoded Fe protein), and a catalytic component, NifDK (*nifDK*-encoded MoFe protein, Figure 2.1, left).[2] Two other members of the nitrogenase family, designated the vanadium and iron-only nitrogenases, are also two-component systems comprising a reductase component, VnfH or AnfH (*vnfH*- or *anfH*-encoded Fe protein), and a catalytic component, VnfDGK (Figure 2.1, right) or AnfDGK (*vnfDGK*-encoded VFe protein or *anfDGK*-encoded FeFe protein).

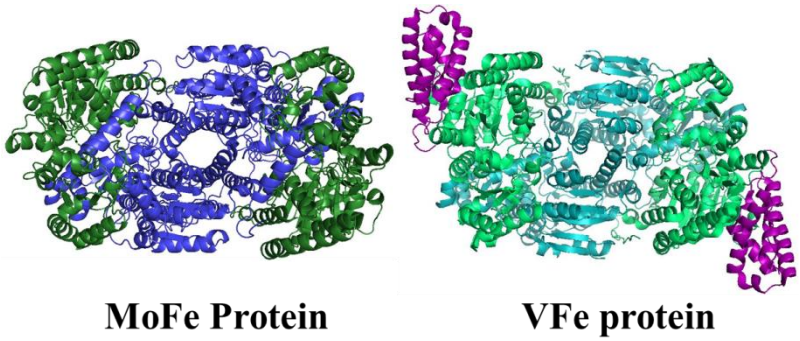

Figure 2.1: X-ray crystallographic structures of the MoFe and VFe proteins.
PDB IDs: 1N2C and 5N6Y for MoFe and VFe proteins respectively.

Both alternative nitrogenases are competent towards N_2 reduction, albeit at lower activities compared to their Mo counterpart.[3,4] Owing to the close sequence homology of the nitrogenase systems,[5] the difference in enzymatic activity must derive from the nature of the metallocofactors (Figure 2.2) housed in the active sites of each catalytic component protein. Within the active sites of the MoFe protein resides an [(*R*-homocitrate)$MoFe_7S_9C$]-core cofactor (M-cluster) which is responsible for the unique catalytic activity of the enzyme. Similarly, X-ray methods have recently established that VFe protein contains a [VFe_7S_nC]-core cluster (n is proposed to be 8 or 9; for n = 8, a sulfur in the belt region of the cofactor is replaced by a carbonate moiety), the V-cluster.[6,7] In addition, the scaffold protein NifEN has been shown to house an iron-only [Fe_8S_9C]-core precursor (L-cluster) that can be matured via biosynthetic pathways to the M-cluster and delivered to the cofactor-deficient MoFe protein ($NifDK^{apo}$) to form a fully functional MoFe protein.[8,9]

Notably, cofactors isolated from the nitrogenase proteins maintain catalytic activity toward a variety of substrates.[10,11] For example, in the absence of their respective protein scaffolds, the isolated clusters in Figure 2.2 can facilitate catalytic conversion of CO_2, CO, and CN^- to C1−C4 hydrocarbons. This activity has not otherwise been observed in molecular

catalytic systems.[12,13] Functional and structural mimics of the metallocofactors are a common synthetic target in order to access the cofactors' unique reactivity and to understand their properties and mechanisms, but exact structural or functional mimics of the cofactors have yet to be reported.[14-22] As there are no direct synthetic mimics of the nitrogenase cofactors, measurements on the isolated cofactors are invaluable to elucidating properties of their catalytic functions.

The distinctive reduction chemistry enabled by the nitrogenase proteins has spurred interest in evaluating their redox properties. In this context, it is important to note that the catalytic MoFe and VFe proteins can be reduced with or without their respective reductase partners, NifH and VnfH. Over the past 45 years, oxidative and reductive midpoint potentials for the MoFe protein,[23-27] the VFe protein,[28] the Fe protein,[29,30] the MoFe/Fe protein complex,[30-33] and the VFe/Fe protein complex[33] have been measured through electrochemical titration in tandem with electron paramagnetic resonance (EPR) spectroscopy or magnetic circular dichroism (MCD) spectroscopy. While none of the isolated nitrogenase proteins can directly exchange electrons with an electrode,[34] each proteins' reduced states have been accessed via redox mediators and chemical reductants.[27,35-37]

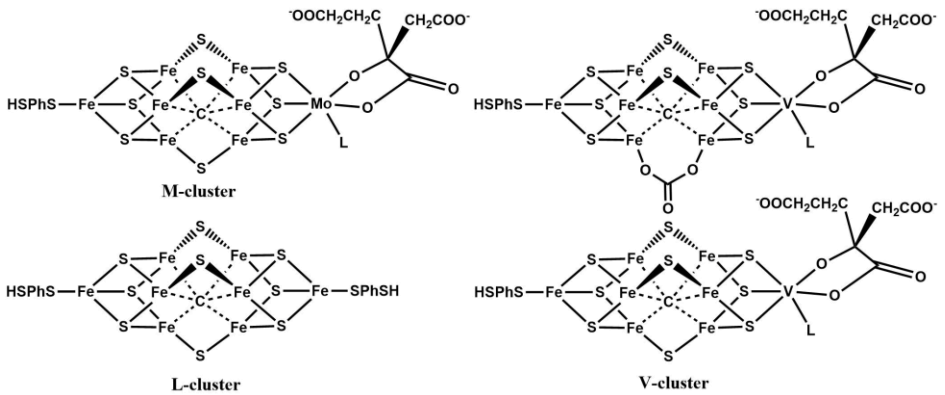

Figure 2.2: Molecular structures of the isolated nitrogenase cofactors.

In contrast, measuring the electrochemical properties of the isolated metallocofactors does not require the use of mediators and can be interrogated directly at an electrode.[38-40] Studies of the electrochemical properties of the isolated cofactor systems are important to correlating the redox potentials of the cofactor to those of the holoprotein, and to understanding the effect the primary and secondary coordination spheres within the holoprotein have on the cofactor. The reactivity of nitrogenase enzymes is contingent upon the accessible redox states of the cofactors. As a result, direct measurement of the electrochemical properties of each cluster provides insight into how the core cluster composition of the cofactors influences electron transfer and catalysis during enzymatic reductive turnover.

The redox potentials of the M-cluster have been thoroughly studied via cyclic voltammetry (CV). The CO and N_2 binding properties of the cofactor have also been explored through infrared spectroelectrochemistry.[38,40-42] The isolated M-cluster was first electrochemically characterized by Schultz and coworkers who identified its two reduction potentials and correlated the resulting complexes' spin states via EPR spectroscopy.[38] Upon chemical reduction by dithionite, the cofactor's semi-reduced or reduced states (S = integer by EPR) were regenerated. The isolated cofactor could then be installed into $NifDK^{apo}$ and the reversibility of the chemical redox process was verified by acetylene reduction assay experiments. Further studies by Schultz and coworkers determined that ligand environment, oxidation state, and solvent preparation can alter the electrochemical properties of the cluster.[42]

Although the electrochemical properties of the extracted M-cluster have been reported under a variety of conditions, no equivalent studies of the isolated V-cluster or L-cluster have ever been performed. Discernible differences in the electrochemical properties of the different clusters would provide useful context for their biases towards the catalytic reduction of

substrates. This study describes the first electrochemical study of the V- and L-clusters and compares their redox potentials to those previously reported for the M-cluster and the native proteins housing these cofactors.

2.2 Results and Discussion

2.2.1 Control experiments

To ensure that all measured electrochemical potentials originated from the nitrogenase cofactors isolated for this study, a series of controls were performed. The *N*-methylformamide solvent that is used to extract the nitrogenase cofactors contains numerous additional reagents such as 1,4-benzenedithiol, sodium bicarbonate, and sodium dithionite that needed to have their electrochemical properties analyzed before definitive assignment of redox potentials to the cofactors. Additionally, nitrogenase proteins, and the cells that they were extracted from, contain other sources of potentially redox active metal ions (e.g. the Fe_8S_7 P-cluster within the MoFe and VFe proteins).

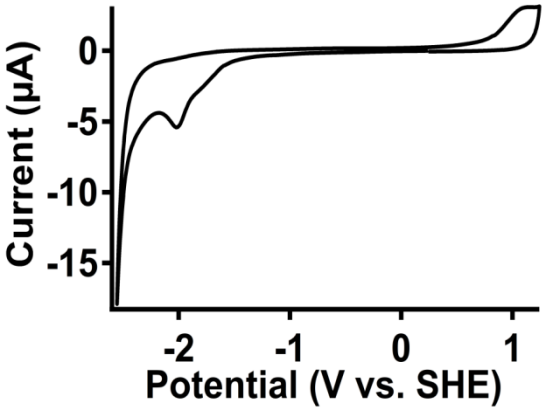

Figure 2.3: Cyclic voltammogram of *N*-methylformamide distilled over $NaHCO_3$. with 100 mM tetrabutylammonium hexafluorophosphate as supporting electrolyte. Working electrode: 1 mm glassy carbon disk; counter electrode: glassy carbon rod; reference electrode: SCE. E_{pc} = –2.01V *vs.* SHE.

The cyclic voltammogram of the NMF solvent used in this study is presented in Figure 2.3. The solvent was both distilled over and treated with sodium bicarbonate until an aliquot in water provided a pH reading of 9. The solvent does not provide any redox activity except for a large irreversible reduction at –2.01 V *vs*. SHE as well as an oxidation at 1 V vs. SHE.

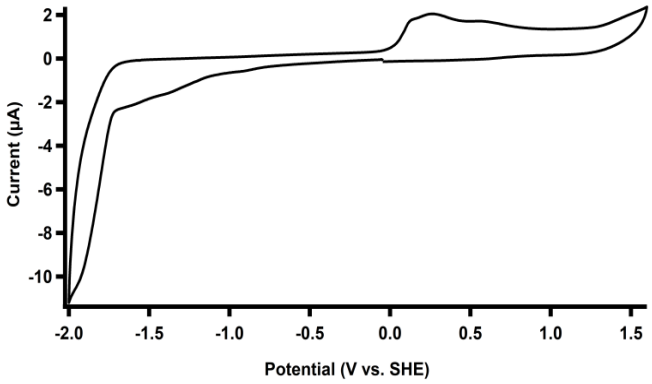

Figure 2.4: Cyclic voltammogram of a 1 mM solution of 1,4-benzenedithiol in *N*-methylformamide with 100 mM tetrabutylammonium hexafluorophosphate as supporting electrolyte. Working electrode: 1 mm glassy carbon disk; counter electrode: glassy carbon rod; reference electrode: saturated Ag/AgCl.

1,4-Benzendithiol is added as a stabilization and capping agent to the nitrogenase cofactors. The use of the dithiol in the extract provides greater extraction recovery yields than the monothiol. However, due to the presence of base and an excess of dithiol in solution as well as an unprotected thiol on the opposite end of the molecule in solution, the redox properties were independently examined. Cyclic voltammetry of 1,4-benzendithiol in NMF, shown in Figure 2.4, demonstrate no new reduction events from those seen in Figure 2.3 and does not show any redox character in the electrochemical window of the nitrogenase cofactors (*vide infra*). An

irreversible oxidation is observed between 0 - 0.5 V *vs.* SHE attributed to the oxidation of the thiol moieties, likely to a dithiol.

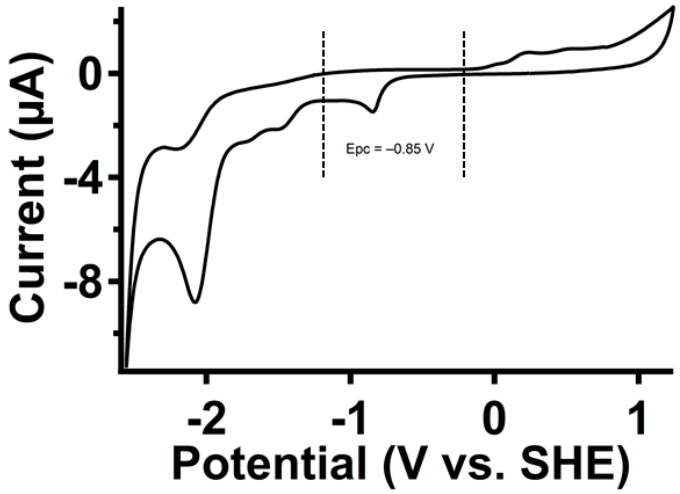

Figure 2.5: Cyclic voltammogram of an NMF solution containing 1,4-benzenedithiol, sodium dithionite, and sodium bicarbonate prior to cofactor extraction. 100 mM tetrabutylammonium hexafluorophosphate added as supporting electrolyte. Working electrode: 1 mm glassy carbon disk; counter electrode: glassy carbon rod; reference electrode: SCE. Sodium dithionite - E_{pc} = –0.85V *vs.* SHE. The area between the dashed lines indicates the window in which cofactors possessed redox events for this study.

To test the redox properties of the NMF solution used for cluster extraction, a cyclic voltammogram of the NMF solvent containing sodium bicarbonate, 1,4-benzenedithiol, and sodium dithionite was analyzed (Figure 2.5). The reduction at –2 V and the broad oxidation between 0.5 - 1 V *vs.* SHE from Figures 2.3 and 2.4 respectively are observed. The addition of an excess of sodium dithionite to the extraction mixture is required to prevent incidental oxidation by dioxygen during extraction as the process is performed on the bench top using air-free Schlenk techniques. A consequence of using sodium dithionite for this purpose is that it possesses an irreversible reduction at –0.85 V vs. SHE in NMF shown in Figure 2.5. This reduction event is in the window of interest for this study. Additionally, the spontaneous decomposition of sodium dithionite into its radical decomposition products is hypothesized to be

a source of instability, resulting in a short lifetime of the isolated cofactors at room temperature. Fortunately in this study nearly all of the sodium dithionite was consumed by the cofactors, leading to the cofactors' isolation in their semi-reduced state, as its reductive event is absent for the M- and L-cluster.[38-40,42] One exception to this is noted in Figure 2.8.a. Samples containing V-cluster presented a small broad reductive feature at –0.85 V vs. SHE and has been assigned to the presence of excess sodium dithionite.

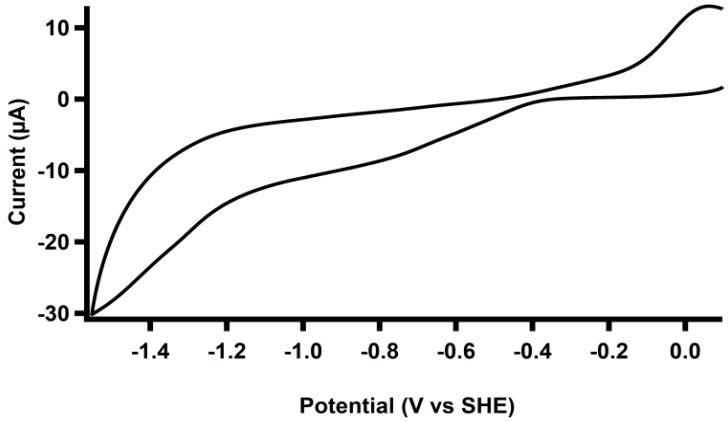

Figure 2.6: Cyclic voltammogram of an NMF solution that was obtained through the cofactor extraction procedure using the cofactor-deficient apo MoFe protein ($NifDK^{apo}$) as the source protein. Working electrode: 1 mm glassy carbon disk; counter electrode: glassy carbon rod; reference electrode: saturated Ag/AgCl.

Finally, to verify that all reductions reported in this work were cofactor-derived and did not originate from other electroactive species accumulated in the solution from the extraction process, a negative control experiment was performed utilizing a cofactor-deficient but P-cluster-replete variant of NifDK ($NifDK^{apo}$). The $NifDK^{apo}$ protein was subjected to the same procedure used to isolate the M/V/L-clusters and the resulting extract was subsequently analyzed by CV experiments. Measurements from this solution did not produce any reduction events between 0

and −1.6 V vs. SHE (Figure 2.6), confirming that the potential window relevant for this study contains only cofactor-derived reduction events.

2.2.2 Electrochemical characterization of the M-cluster

Cyclic voltammetry of the M-cluster (Figure 2.7.a) revealed two reduction events at $E_{1/2}$ = −0.27 V and E_{pc} = −0.94 V *versus* the standard hydrogen electrode (SHE), respectively. Previously, Pickett and coworkers assigned three reduction events using CO binding and ligand exchange experiments. The first reduction event was assigned to the terminal iron center opposite to the molybdenum center within the cluster, and the second reduction event was assigned as delocalized over the iron-sulfur core of the cofactor.

An observed third reduction event was hypothesized to be localized on the molybdenum center; this redox event has not been observed in any other electrochemical study of the M-cluster. The first redox process observed in this study is reversible (Table 2.1) and its redox potentials are in agreement with those measured by Schultz and Pickett (Table 2.2).[38,40,43,44] However, a few differences were observed with our study compared to the prior work. In this work, the second reduction (E_{pc2}, Table 2.2) is irreversible, whereas it was previously described as quasi-reversible. The differences may be due to changes in preparation of the cofactor. The cofactors in this work utilized 1,4-benzendithiol as capping agents for the terminal iron centers while the cofactor used by Pickett et al. employed a monothiophenol modification to the terminal iron center. A cyclic voltammogram of 1,4-benzendithiol in NMF shows an irreversible oxidation event positive of the redox potentials assigned to the nitrogenase cofactors (Figure 2.4). While the direct oxidation of the dithiol is present in the cofactor samples, its oxidation

potential is sufficiently positive such that it does not interfere with the assignment of the redox potentials of the cofactors.

To verify reversibility of the couples observed in all cluster experiments, the anodic and cathodic peak currents were plotted versus the square root of the variable scan rates measured for each cluster. The linear relationship between the peak currents and the scan rate of the measurement is dictated by the Randles-Sevcik equation:

$$i_p = 0.4463nFAC\left(\frac{nFvD}{RT}\right)^{\frac{1}{2}} \quad (1)$$

Where i_p is the peak current, n is the number of electrons passed in the redox process, F is Faraday's constant, A is the electrode surface area, C is the concentration of analyte, D is the diffusion coefficient, R is the ideal gas constant, T is the temperature, and *v* is the scan rate. In an ideal diffusion-controlled, electrochemically reversible cyclic voltammetry experiment, all parameters should remain constant except the independent variable, *v*, leading to a linear relationship between $v^{½}$ and i_p. Differences in slope between the fitted lines of the anodic and cathodic peak currents can only be attributed to an irreversible or quasi-reversible electrochemical process. An irreversible process infers that is n is not the same for forward and reverse redox processes. Additionally, because equation 1 does not have a y-intercept, the fitted lines should, according to theory, pass through the origin. Therefore, in each cluster data set, the fitted line was forced to pass through the origin. The peak current vs. square root of scan rate plot for the M-cluster, Figure 2.6.c, presents curves for both anodic and cathodic peak currents which correlate strongly to a linear fit. Similarly, as tabulated in Table 2.1, $|i_{pa}/i_{pc}|$ is approximately equal to unity indicating similar slopes and a reversible electrochemical process.

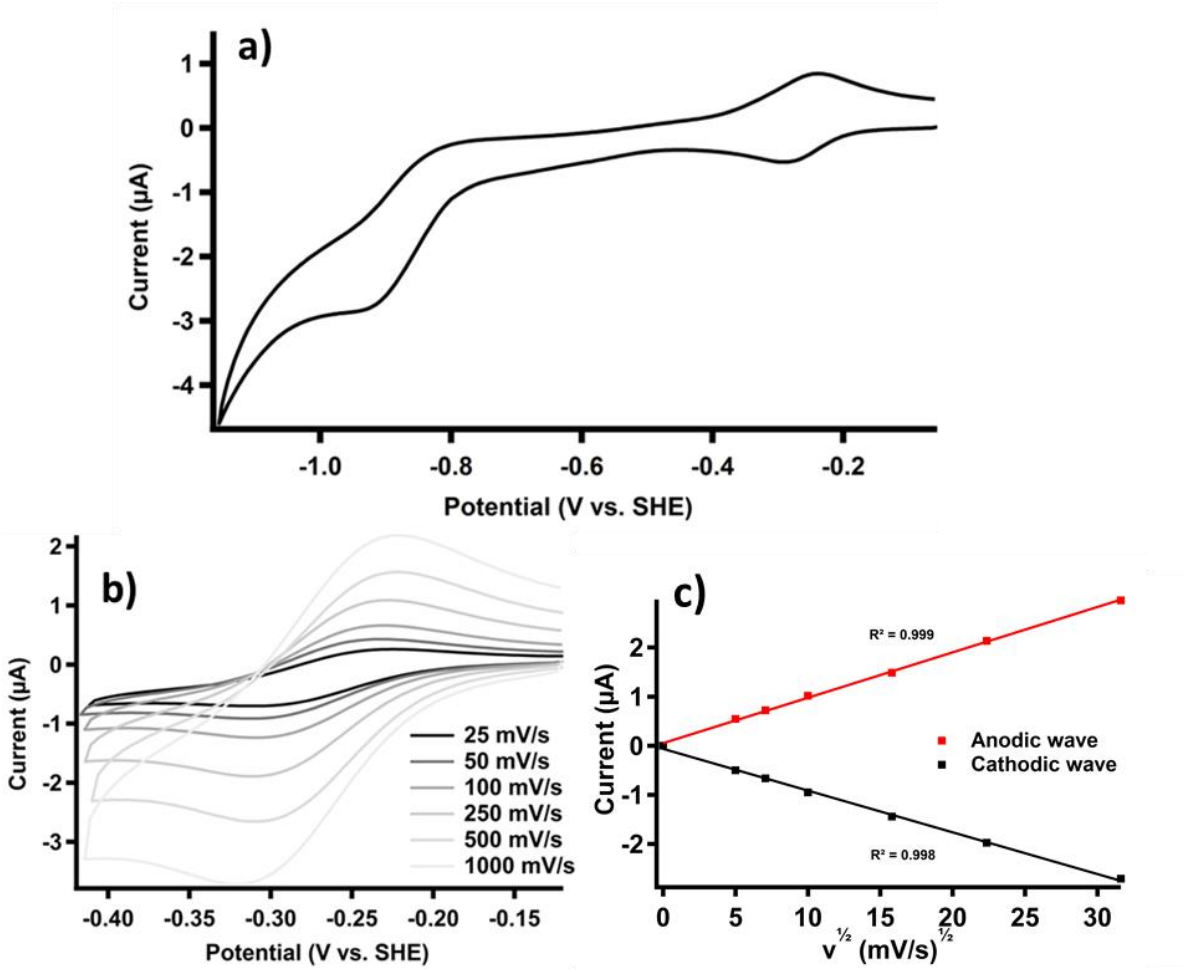

Figure 2.7: Cyclic voltammograms of 0.8 mM M-cluster in NMF in the presence of 1,4-benzenedithiol. a) Full electrochemical scan at a scan rate of 25 mV/s. b) Variable scan rate cyclic voltammogram of the first redox potential, ranging from scan rates of 25 to 1000 mV/s. c) Peak current vs. square root of scan rate plot for anodic and cathodic peak currents from data in Table 2.1 for the isolated first reduction potential of the M-cluster. Potentials are reported *versus* the standard hydrogen electrode. Glassy carbon working and auxiliary electrodes were used for these measurements.

Table 2.1: Variable scan-rate peak data for the isolated first reduction potential of the M-cluster.

			Anodic wave		Cathodic wave			
Scan	v (mV/s)	√v $(mV/s)^{½}$	E_{pa} (mV *vs.* SHE)	i_{pa} (μA)	E_{pc} (mV *vs.* SHE)	i_{pc} (μA)	$\lvert i_{pa}/i_{pc} \rvert$	$E_{pa} - E_{pc}$ (mV)
1	25	5	−227	0.544	−313	−0.501	1.086	86
2	50	7.071	−232	0.722	−313	−0.666	1.084	81
3	100	10	−229	1.014	−311	−0.952	1.065	82
4	250	15.811	−230	1.486	−310	−1.444	1.029	80
5	500	22.361	−225	2.135	−311	−1.976	1.081	86
6	1000	31.623	−222	2.957	−322	−2.708	1.092	100

Table 2.2: Redox potentials of the M-cluster, referenced *versus* the standard hydrogen electrode (SHE). $E^{o'}_1$ refers to the $E_{1/2}$ of the first measured redox process. E_{pc2} and E_{pc3} refer to the potential where the peak cathodic current is observed for the second and third irreversible reduction events, respectively.

MoFe protein or M-cluster voltammetric study	$E^{o'}_1$ (V)	E_{pc2} (V)	E_{pc3} (V)	Ref
MoFe protein	−0.17	−0.465	–	43, 44
Shultz (1985)	−0.33	−0.96	–	38
Pickett (2003)	−0.31	−0.94	−1.09	40
This work	−0.27	−0.94	–	

2.2.3 Electrochemical characterization of the V-cluster

The extracted V-cluster yielded a quasi-reversible redox event at $E_{1/2} = -0.414$ V vs. SHE with a peak-to-peak separation (ΔE_p) of approximately 0.09 V (Table 2.3). An irreversible reduction event was also observed at $E_{pc} = -1.06$ V vs. SHE (Figure 2.8.a). The increasing ΔE_p for the first reduction of the V-cluster with increasing scan rates is consistent with a quasi-reversible redox event. Figure 2.8.c displays the current *vs.* square root of the scan rate plot for the reversible couple seen in Figure 2.8.b. The linear regression of the resulting points were forced to pass through the origin and provided a sub-optimal fit. Anodic and cathodic peak currents resulting from scan rates at 12.5 and 25 mV/s were omitted from the linear regression in an attempt to plot only the most electrochemically reversible points, but are still reported in Table 2.3. Despite omission of the 4 mentioned points, correlation to the linear regression still reamined lower than ideal at 0.95 and 0.97 for the anodic and cathodic peak currents respectively. A low correlation as well as $|ipa/ipc| \neq 1$ (Table 2.3) supports the argument for a quasi-reversible assignment of the isolated first reduction potential of the V-cluster indicating that either the number of electrons (n) is different for the forward and reverse redox process, electron transfer is sluggish, or the cluster is undergoing a structural rearrangement upon reduction.

The peak of the irreversible reduction potential of the V-cluster is less resolved relative to its M-cluster analogue. In addition to the quasi-reversible and irreversible reduction potentials discussed above, there are two broad reductive features observed ca. −0.8 V and −0.9 V vs. SHE (in Figure 2.8.a), and are likely due to excess sodium dithionite (Figure 2.5).

The cyclic voltammogram in Figure 2.8.a displays redox events with a $\Delta E = 0.647$ V (the difference between the $E_{1/2}$ of the first reduction potential and the E_{pc} of the second reduction potential) and is nearly identical to the equivalent difference (ΔE) for the redox events of the M-cluster. Substituting the molybdenum ion center for vanadium shifted both peak potentials approximately 100 mV more negative. This shift in reduction potential may offer an explanation as to why the VFe protein is able to effectively catalyze the reduction of CO to hydrocarbons as seen by Ribbe and coworkers, while the M-cluster can only bind the CO substrate.[5,45] The intrinsically more reducing V-cluster is able to more easily activate the C-O bond to facilitate reactivity upon accessing its reduced states. These findings highlight the significant impact the protein environment along with the intrinsic redox properties of the cofactor have on CO activation. Two recent studies of nitrogenase hybrid systems, where the M- or V-cluster is 'heterologously' combined with the apo VFe or MoFe protein scaffold, further illustrate the combined effects of the cofactor properties and the protein environment on the differential reactivity of the VFe and MoFe proteins toward CO.[46,47] The V-cluster in its native protein environment is a significantly better catalyst for CO reduction than the holo MoFe protein, M-cluster reconstituted in the apo VFe protein, or V-cluster reconstituted in the apo MoFe protein. The differential reactivity indicated that both the vanadium cofactor and vanadium protein environment are necessary for efficient reduction of CO.

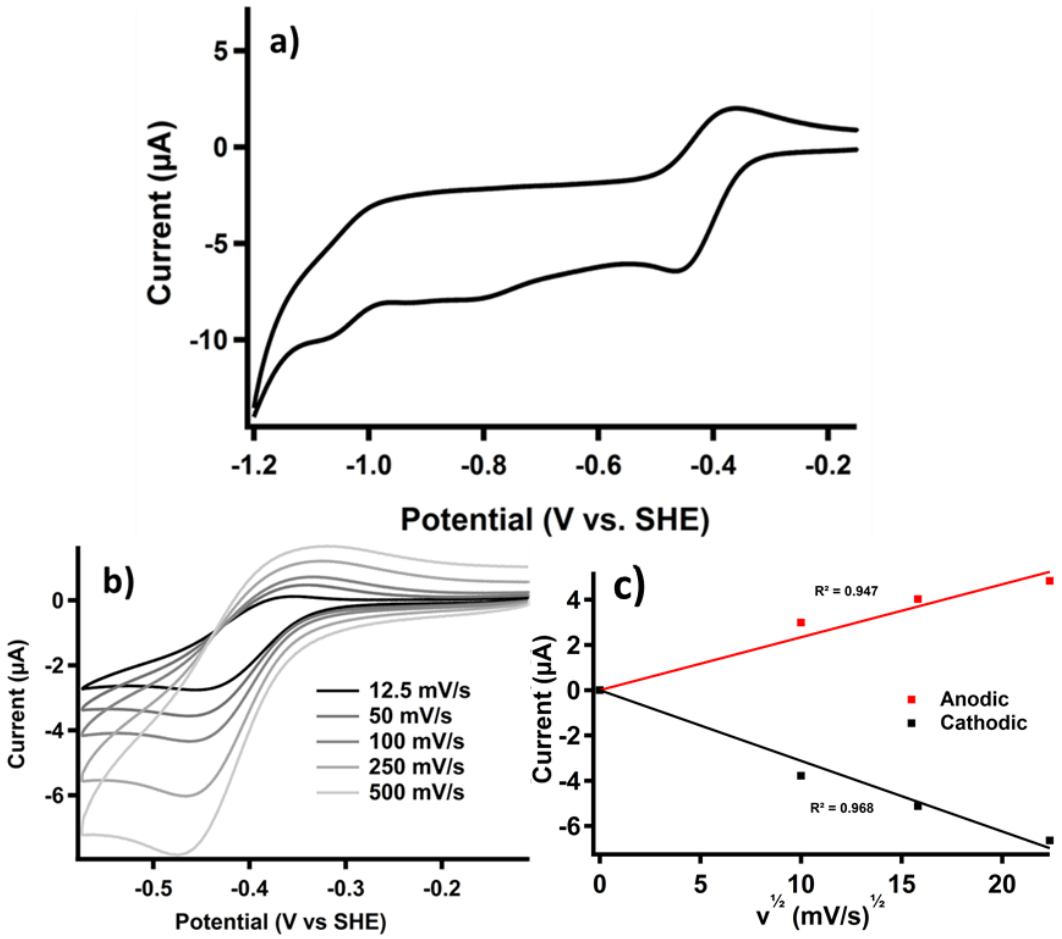

Figure 2.8: Cyclic voltammograms of the isolated V-cluster in an NMF solution. 1.3 mM V-cluster measured against an Ag/AgCl reference electrode. a) Full electrochemical scan at a scan rate of 100 mV/s. b) Variable scan rate cyclic voltammograms of the first reduction potential of V-cluster ranging from scan rates of 12.5 – 500 mV/s. c) Peak current vs. square root of scan rate plot from anodic and cathodic peak currents in Table 2.3 for the isolated first reduction potential of the V-cluster. Data from 12.5 and 25 mV/s were omitted to provide a meaningful fit with the Randles-Sevcik equation. Potentials are reported *versus* the standard hydrogen electrode. Glassy carbon working and auxiliary electrodes were used for these measurements.

Table 2.3: Variable scan-rate peak data for the isolated first reduction potential of V-cluster.

			Anodic wave		Cathodic wave			
Scan	ν (mV/s)	$\sqrt{\nu}$ $(mV/s)^{½}$	E_{pa} (mV vs. SHE)	i_{pa} (μA)	E_{pc} (mV vs. SHE)	i_{pc} (μA)	$\lvert i_{pa}/i_{pc} \rvert$	$E_{pa} - E_{pc}$ (mV)
1	12.5	3.536	−309	1.719	−403	−2.551	0.674	94
2	25	5	−304	2.001	−406	−2.760	0.725	102
3	50	7.071	−297	2.366	−419	−3.069	0.771	122
4	100	10	−289	2.987	−413	−3.783	0.790	124
5	250	15.811	−283	4.020	−419	−5.124	0.785	136
6	500	22.361	−273	4.824	−428	−6.640	0.726	155

Oxidative features were not analyzed in this study as all clusters and controls contain multiple oxidation events, making it impossible to assign redox potentials to the isolated cofactors without further tandem spectroscopic experiments. Figure 2.9 gives an example of the oxidative region of both the V-cluster (black) and cofactor-deficient apo MoFe protein. The apo MoFe protein extract presents a large irreversible oxidation near 0 V vs. SHE. The V-cluster similarly shows oxidative activity slightly more positive near 0.12 V vs. SHE and 0.44 V vs. SHE.

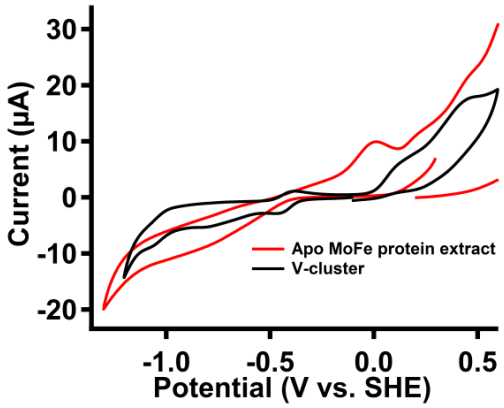

Figure 2.9: Cyclic voltammogram with the oxidative region shown of an NMF solution that was obtained through the cofactor extraction procedure using the cofactor-deficient apo MoFe protein ($NifDK^{apo}$) as the source protein (black) and the V-cluster (red). Working electrode: 1 mm glassy carbon disk; counter electrode: glassy carbon rod; reference electrode: saturated Ag/AgCl.

2.2.4 Electrochemical Characterization of the L-cluster

The L-cluster (Figure 2.2), an iron-only biosynthetic precursor to the M-cluster, was isolated from the scaffold protein NifEN.[8,9] The electrochemistry of this cluster is very similar to the M-cluster, with some notable differences. The extracted L-cluster possesses two electrochemical events. The L-cluster, when scanned cathodically in the same potential window as the M-cluster, displays one reversible (Table 2.4) and one irreversible redox event (Figure

2.4); however, it should be noted that an open circuit potential (i.e. the resting electrochemical potential of the cluster solution) of −0.57 V vs. SHE was measured, indicating that the L-cluster, as isolated, rests in a semi-reduced state. The redox event at −0.27 V vs. SHE is electrochemically reversible upon isolating the redox waves (Figure 2.10.b), although scanning to more negative potentials causes the anodic event to pass significantly more current than the original reduction. The large oxidation suggests that the L-cluster is being chemically altered upon accessing the larger reduction at E_{pc} = −0.92 V vs. SHE, which could indicate degradation of the cluster. Reversibility of the isolated reduction potential in Figure 2.10.b was confirmed by the peak current *vs.* square root of scan rate plot in Figure 2.10.c and tabulated data in Table 2.4. Good correlation of the linear fit, similar slopes of the anodic and cathodic peak currents, and $|i_{pa}/i_{pc}| \approx 1$ all indicate that the first redox process is reversible.

The reduction potentials measured for the L-cluster are nearly identical to those measured for the M-cluster (Table 2.5), suggesting that the molybdenum center does not significantly impact the energy of the molecular orbital(s) involved in the first two reductions of the iron-sulfur core. This observation contrasts with that observed with the V-cluster, which shows a significant cathodic shift of the redox potentials.

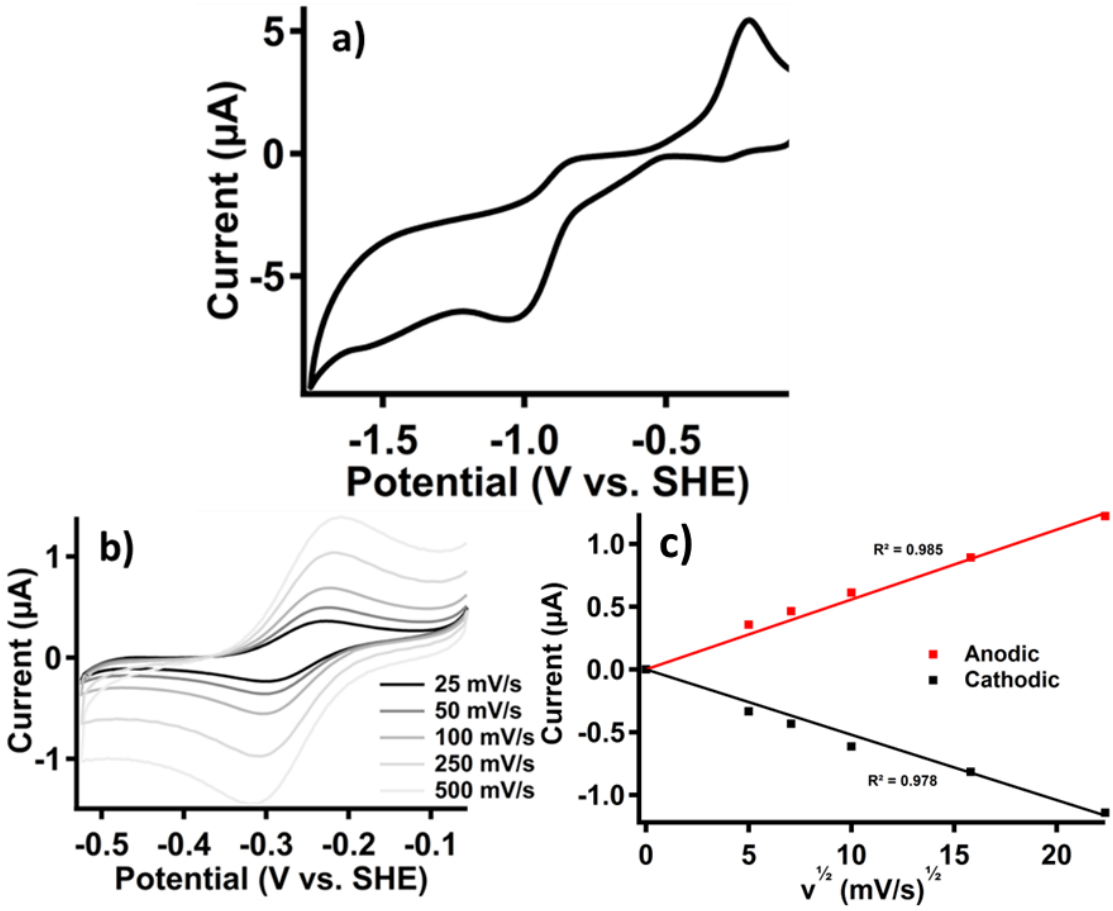

Figure 2.10: Cyclic voltammograms of 0.58 mM isolated L-cluster in an NMF solution. a) Full reductive scan. b) Variable scan rate cyclic voltammogram of the first reduction potential. c) Peak current vs. square root of scan rate plot from anodic and cathodic peak currents in Table 2.4 for the isolated first reduction potential of the V-cluster. Potentials were measured against an SCE reference electrode and reported *versus* the standard hydrogen electrode. Glassy carbon disk working electrode and auxiliary electrode were used for these measurements.

Table 2.4: Variable scan rate peak data for the isolated first reduction potential of L-cluster.

			Anodic wave		Cathodic wave			
Scan	v (mV/s)	√v $(mV/s)^{½}$	E_{pa} (mV vs. SHE)	i_{pa} (μA)	E_{pc} (mV vs. SHE)	i_{pc} (μA)	$\lvert i_{pa}/i_{pc} \rvert$	$E_{pa} - E_{pc}$ (mV)
1	25	5	−223	0.357	−301	−0.334	1.067	78
2	50	7.071	−224	0.464	−301	−0.433	1.072	77
3	100	10	−224	0.627	−306	−0.611	1.026	82
4	250	15.811	−220	0.892	−307	−0.816	1.092	87
5	500	22.361	−209	1.222	−317	−1.142	1.070	108

2.2.5 Overall comparison of cofactors

With the experimental data collected in Table 2.5, comparisons between the redox properties of the cofactors and their respective protein scaffolds can be made. As seen in Table 2.5,[28,33,43,44,48,49] all measured isolated cofactor reduction potentials are significantly more negative than those reported previously for any protein. Electron transfer to the nitrogenase cofactors is gated by the [Fe_8S_7] P-cluster and assigning reductions to the cofactors beyond their first reduction potentials is not possible without binding of the Fe protein-MgATP complex; however, it is clear that housing the cofactor within the protein dramatically decreases the potential required to access the electronic states needed to initiate catalysis.

Prior studies have found that the redox potentials of most cofactors, including cytochromes, Fe–S and Cu redox centers, are highly dependent on their cellular environment.[50] Additionally, the redox potentials of synthetic Fe—S clusters measured in organic solvents are often negative of those measured in proteins.[51] It is possible that effects from the secondary coordination sphere of the protein-housed nitrogenase cofactors can aid in substrate binding and can be a factor for the more positive reduction potentials observed. Although relatively few studies have been performed to probe secondary coordination sphere effects in the nitrogenase proteins,[52] hydrogen bonding from amino acid residue His-195 has been observed to be necessary for the reduction of dinitrogen as well as binding of CO in MoFe protein as observed in single crystal X-ray structures.[53-54] Future studies investigating the reduction potentials of the nitrogenase proteins should focus on mutant proteins with His-195 substituted in order to observe its effect on protein reduction potential.

Table 2.5: Tabulated reduction potentials of the isolated M-, V-, and L-clusters of *Azotobacter vinelandii* in the presence of 1,4-benzenedithiol. Shown are midpoint potential values reported for the VFe protein from *Azotobacter chroococum* (Ac1*). Values for the VFe protein from *Azotobacter vinelandii* (Av1*) have not been reported. All potentials are referenced to the standard hydrogen electrode.

Nitrogenase Protein or cluster	E_1 (V)	E_2 (V)	Ref
Fe Protein (Av2)	−0.310		47
$FeP(MgADP)_2$ (Av2)	−0.430		47
$FeP(MgATP)_2$ (Av2)	−0.490		47
$FeP(MgADP)_2$ (Ac2)	−0.450		33
$FeP(MgADP)_2$ (VNifH, Ac2*)	−0.463		33
MoFe Protein (Av1)	−0.042		47
	−0.17	−0.465	43, 44
VFe protein (Ac1*)	−0.125	−0.390	28
M-cluster	−0.27	−0.94	
V-cluster	−0.414	−1.06	
L-cluster	−0.27	−0.92	

Based on the results of this work, the L-ligand in Figure 2.2 is speculated to have a larger effect than the identity of the heterometal on the redox potential of the cluster. The nearly identical redox potentials of the M- and L-clusters suggest the molybdenum center does not have a direct effect on the molecular orbital energies involved in the first two reduction events. However, given the propensity of the tetrahedral Fe centers of the nitrogenase cofactors to coordinate sulfur-based ligands (e.g., cysteine or thiolates), we hypothesize that the Fe termini of the L-cluster are both capped with 1,4-benzenedithiol, while the heterometal in the M- and V-clusters are ligated by anionic NMF. In addition, as seen in Schultz et al.,[42] there is an anodic shift of the reduction potential of these clusters due to the thiophenolate ligation.

2.3 Conclusions

Electrochemical potentials were measured for the extracted cofactors of molybdenum and vanadium nitrogenase, as well as an all-iron, M-cluster precursor similar in structure to the Fe-only cluster. The results of these measurements provide interesting insights into the effect that the molybdenum or vanadium heterometal has on the electronic structure of the iron-sulfur core of the respective cofactor. The M- and L-clusters, when capped with a dithiophenolate, display nearly identical electrochemical characteristics, while the V-cluster shows cathodic shifts in the redox potentials of its iron-sulfur core. These studies contextualize the different reaction patterns of the nitrogenase cofactors while highlighting the impact of the secondary coordination sphere on redox properties.

2.4 Experimental Details

General considerations

Unless otherwise specified, all chemicals were purchased from Sigma-Aldrich (St. Louis, MO) and Thermo Fisher Scientific (Waltham, MA). Solvents were purified before use by passing through columns of activated alumina and a supported copper catalyst. All experiments were conducted under an Ar or N_2 atmosphere using Schlenk techniques and a Vacuum Atmospheres (Hawthorne, CA) Omni-lab glovebox with an Ar atmosphere and an O_2 level of < 2 ppm. Metal ion concentrations were determined via inductively-coupled plasma–optical emission spectroscopy (ICP–OES) using an iCAP 7200 DUO system (Thermo Fisher Scientific Inc., Waltham, MA). ^{1}H NMR spectroscopy was

performed on a 500 MHz Bruker Avance GN500 with a BBO probe. Chemical shifts have been internally calibrated to the monoprotio impurity of the deuterated chloroform.

Protein Purification and M-Cluster Extraction

Procedures in this section, except ^{1}H NMR spectroscopy, were performed by collaborators in the Ribbe and Hu Laboratories

Azotobacter vinelandii strains expressing the His-tagged Mo-nitrogenase (DJ1141), His-tagged V-nitrogenase (YM68A), and His-tagged scaffold protein NifEN (DJ1041), respectively, were grown as described elsewhere.[55,56] Published methods were used for the purification of these nitrogenase proteins.[55,56] A total of 1.5 g of MoFe protein, VFe protein and NifEN, respectively, were used for the extraction of M-, V- and L-clusters. The M-cluster, V-cluster and L-cluster were extracted into N-methylformamide (NMF) distilled using a previously established protocol.[7,57,58] Although distilled NMF is commonly used to extract nitrogenase cofactors, characterization of the distillate has never been performed. Pickett et al. speculated it contained deprotonated NMF, which could potentially serve as a ligand. We validated Pickett's hypothesis by performing ^{1}H NMR spectroscopy on the distillate and found evidence for a small amount of deprotonated NMF (Figure 2.11) and no other impurities that may have been hypothesized to be present.

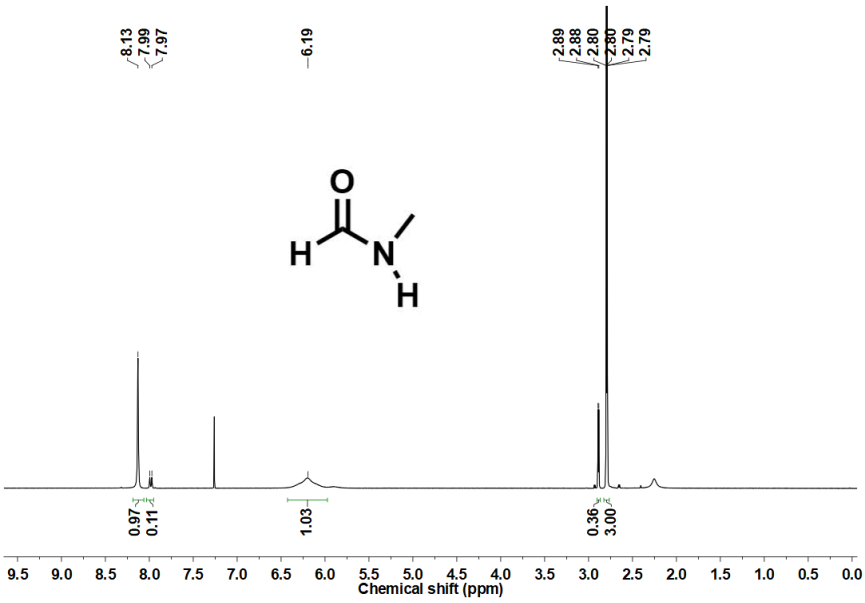

Figure 2.11: ^{1}H NMR spectrum of NMF treated with $NaHCO_3$ in $CDCl_3$

Cluster concentration determination with ICP-OES

<u>These procedures were performed by collaborators in the Ribbe and Hu Laboratories</u>

Aliquots of cluster were digested for 30 min in 20% HNO_3 at 250°C. Metal ion concentrations were determined with ICP–OES, and samples were calibrated against diluted Fe/S/Mo/V standard solutions. The concentrations of the M- and V-clusters were calculated on the basis of the determined concentrations of Mo and V, respectively. The concentration of the L-cluster was estimated by dividing the determined concentration of Fe by 8.[46]

Electrochemical experiments

All electrochemical measurements were performed on a Pine Wavedriver 10 potentiostat with AfterMath software. Measurements were obtained using a 1 mm diameter vitreous carbon disc working electrode and a vitreous carbon rod auxiliary electrode. A saturated calomel reference

electrode (CH Instruments) or an Ag/AgCl reference electrode (CH Instruments) in a saturated KCl solution, separated from the bulk solution by a Teflon tip, was used. Potentials measured against the saturated Ag/AgCl reference electrode were adjusted +0.197 V *vs*. the standard hydrogen electrode (SHE). Potentials measured against the saturated calomel electrode were adjusted +0.244 V vs. SHE. No additional supporting electrolyte was required for measurements. Electrodes were fitted and immobilized into an oven-dried half-dram shell vial cell, where measurements were taken on 100-200 μL cluster samples in a Vacuum Atmospheres glovebox filled with Ar. Samples were removed from a −78°C freezer where they were stored after isolation. Samples were thawed and subsequently warmed to room temperature before measurement. Samples of the NMF solvent used prior to the extractions were measured by cyclic voltammetry (Figure 2.5).

2.5 References

(1) Ferguson, S. J. *Curr. Opin. Chem. Biol.* **1998**, *2*, 182.

(2) Lee, C. C.; Wiig, J. A.; Hu, Y.; Ribbe, M. W. In *Bioinspired Catalysis*; Weigand, W., Schollhammer, P., Eds.; Wiley-VCH Verlag GmbH & Co. KGaA: 2014.

(3) Eady, R. R.; Robson, R. L.; Richardson, T. H.; Miller, R. W.; Hawkins, M. *Biochem. J.* **1987**, *244*, 197.

(4) Miller, R. W.; Eady, R. R. *Biochem. J.* **1988**, *256*, 429.

(5) Hu, Y.; Lee, C. C.; Ribbe, M. W. *Dalton Trans.* **2012**, *41*, 1118.

(6) Sippel, D.; Einsle, O. *Nat Chem Biol* **2017**, *13*, 956.

(7) Fay, A. W.; Blank, M. A.; Lee, C. C.; Hu, Y.; Hodgson, K. O.; Hedman, B.; Ribbe, M. W. *J. Am. Chem. Soc.* **2010**, *132*, 12612.

(8) Sickerman, N. S.; Rettberg, L. A.; Lee, C. C.; Hu, Y.; Ribbe, M. W. *Essays Biochem.* **2017**, *61*, 271.

(9) Fay, A. W.; Blank, M. A.; Rebelein, J. G.; Lee, C. C.; Ribbe, M. W.; Hedman, B.; Hodgson, K. O.; Hu, Y. *Proc. Natl. Acad. Sci. U.S.A.* **2016**, *113*, 9504.

(10) Eady, R. R.; Leigh, G. J. *J. Chem. Soc., Dalton Trans.* **1994**, 2739.

(11) Rees, J. A.; Bjornsson, R.; Schlesier, J.; Sippel, D.; Einsle, O.; DeBeer, S. *Angew. Chem. Int. Ed.* **2015**, *54*, 13249.

(12) Lee, C. C.; Hu, Y.; Ribbe, M. W. *Angew. Chem. Int. Ed.* **2015**, *54*, 1219.

(13) Lee, C. C.; Hu, Y.; Ribbe, M. W. *Angew. Chem. Int. Ed.* **2012**, *51*, 1947.

(14) Dance, I. *Dalton Trans.* **2010**, *39*, 2972.

(15) Tanifuji, K.; Sickerman, N.; Lee, C. C.; Nagasawa, T.; Miyazaki, K.; Ohki, Y.; Tatsumi, K.; Hu, Y.; Ribbe, M. W. *Angew. Chem. Int. Ed.* **2016**, n/a.

(16) Liu, J.; Kelley, M. S.; Wu, W.; Banerjee, A.; Douvalis, A. P.; Wu, J.; Zhang, Y.; Schatz, G. C.; Kanatzidis, M. G. *Proc. Natl. Acad. Sci. U.S.A.* **2016**.

(17) Scott, T. A.; Holm, R. H. *Inorg Chem* **2008**, *47*, 3426.

(18) Zuo, J.-L.; Zhou, H.-C.; Holm, R. H. *Inorg. Chem.* **2003**, *42*, 4624.

(19) Fomitchev, D. V.; McLauchlan, C. C.; Holm, R. H. *Inorg. Chem.* **2002**, *41*, 958.

(20) Smith, J. M.; Lachicotte, R. J.; Pittard, K. A.; Cundari, T. R.; Lukat-Rodgers, G.; Rodgers, K. R.; Holland, P. L. *J. Am. Chem. Soc.* **2001**, *123*, 9222.

(21) Čorić, I.; Holland, P. L. *J. Am. Chem. Soc.* **2016**, *138*, 7200.

(22) Anderson, J. S.; Rittle, J.; Peters, J. C. *Nature* **2013**, *501*, 84.

(23) Albrecht, S. L.; Evans, M. C. W. *Biochem. Biophys. Res. Commun.* **1973**, *55*, 1009.

(24) O'Donnell, M. J.; Smith, B. E. *Biochem. J.* **1978**, *173*, 831.

(25) Zimmermann, R.; Münck, E.; Brill, W. J.; Shah, V. K.; Henzl, M. T.; Rawlings, J.; Orme-Johnson, W. H. *Biochim. Biophys. Acta* **1978**, *537*, 185.

(26) Watt, G. D.; Burns, A.; Lough, S.; Tennent, D. L. *Biochemistry* **1980**, *19*, 4926.

(27) Watt, G. D.; Burns, A.; Tennent, D. L. *Biochemistry* **1981**, *20*, 7272.

(28) Pierik, A. J.; Lowe, D. J.; Eldridge, M. E.; Marritt, S.; Farrar, J. A.; Thomson, A. J.; Eady, R. R. *In New Horizons in Nitrogen Fixation*; Kluwer Academic Publishers: Dordrecht, 1993.

(29) Morgan, T. V.; Prince, R. C.; Mortenson, L. E. *FEBS Lett.* **1986**, *206*, 4.

(30) Lanzilotta, W. N.; Seefeldt, L. C. *Biochemistry* **1997**, *36*, 12976.

(31) Evans, M. C. W.; Albrecht, S. L. *Biochem. Biophys. Res. Commun.* **1974**, *61*, 1187.

(32) Lough, S.; Burns, A.; Watt, G. D. *Biochemistry* **1983**, *22*, 4062.

(33) Bergström, J.; Eady, R. R.; Thorneley, R. N. *Biochem. J.* **1988**, *251*, 165.

(34) Fourmond, V.; Léger, C. *Angew. Chem. Int. Ed.* **2017**, *56*, 4388.

(35) Milton, R. D.; Abdellaoui, S.; Khadka, N.; Dean, D. R.; Leech, D.; Seefeldt, L. C.; Minteer, S. D. *Energy Environ. Sci.* **2016**, *9*, 2550.

(36) Hu, B.; Harris, D. F.; Dean, D. R.; Liu, T. L.; Yang, Z.-Y.; Seefeldt, L. C. *Bioelectrochemistry* **2018**, *120*, 104.

(37) Vincent, K. A.; Tilley, G. J.; Quammie, N. C.; Streeter, I.; Burgess, B. K.; Cheesman, M. R.; Armstrong, F. A. *Chem. Commun.* **2003**, 2590.

(38) Schultz, F. A.; Gheller, S. F.; Burgess, B. K.; Lough, S.; Newton, W. E. *J. Am. Chem. Soc.* **1985**, *107*, 5364.

(39) Schultz, F. A.; Gheller, S. F.; Newton, W. E. *Biochem. Biophys. Res. Commun.* **1988**, *152*, 629.

(40) Pickett, C. J.; Vincent, K. A.; Ibrahim, S. K.; Gormal, C. A.; Smith, B. E.; Best, S. P. *Chem. Eur. J.* **2003**, *9*, 76.

(41) Pickett, C. J.; Vincent, K. A.; Ibrahim, S. K.; Gormal, C. A.; Smith, B. E.; Fairhurst, S. A.; Best, S. P. *Chem. Eur. J.* **2004**, *10*, 4770.

(42) Schultz, F. A.; Feldman, B. J.; Gheller, S. F.; Newton, W. E. *Inorganica Chim. Acta* **1990**, *170*, 115.

(43) Watt, G. D.; Bulen, W. A. *Nitrogen Fixation*; Washington State University Press: Seattle, 1976.

(44) Braaksma, A.; Haaker, H.; Grande, H. J.; Veeger, C. *Eur. J. Biochem.* **1982**, *121*, 483.

(45) Lee, C. C.; Hu, Y.; Ribbe, M. W. *Science* **2010**, *329*, 642.

(46) Rebelein, J. G.; Lee, C. C.; Newcomb, M.; Hu, Y.; Ribbe, M. W. *mBio* **2018**, *9*.

(47) Lee, C. C.; Tanifuji, K.; Newcomb, M.; Liedtke, J.; Hu, Y.; Ribbe, M. W. *ChemBioChem* **2018**, *19*, 649.

(48) Watt, G. D.; Wang, Z. C.; Knotts, R. R. *Biochemistry* **1986**, *25*, 8156.

(49) Pierik, A. J.; Wassink, H.; Haaker, H.; Hagen, W. R. *Eur. J. Biochem.* **1993**, *212*, 51.

(50) Liu, J.; Chakraborty, S.; Hosseinzadeh, P.; Yu, Y.; Tian, S.; Petrik, I.; Bhagi, A.; Lu, Y. *Chem. Rev.* **2014**, *114*, 4366.

(51) DePamphilis, B. V.; Averill, B. A.; Herskovitz, T.; Que, L.; Holm, R. H. *J. Am. Chem. Soc.* **1974**, *96*, 4159.

(52) Creutz, S. E.; Peters, J. C. *Chem. Sci.* **2017**, *8*, 2321.

(53) Kim, C.-H.; Newton, W. E.; Dean, D. R. *Biochemistry* **1995**, *34*, 2798.

(54) Spatzal, T.; Perez, K. A.; Einsle, O.; Howard, J. B.; Rees, D. C. *Science* **2014**, *345*, 1620.

(55) Hu, Y.; Fay, A. W.; Ribbe, M. W. *Proc. Natl. Acad. Sci. U.S.A.* **2005**, *102*, 3236.

(56) Lee, C. C.; Hu, Y.; Ribbe, M. W. *Proc. Natl. Acad. Sci. U.S.A.* **2009**, *106*, 9209.

(57) Fay, A. W.; Blank, M. A.; Lee, C. C.; Hu, Y.; Hodgson, K. O.; Hedman, B.; Ribbe, M. W. *Angew. Chem. Int. Ed.* **2011**, *50*, 7787.

(58) Burgess, B. K. *Chem. Rev.* **1990**, *90*, 1377.

Chapter 3

Electrocatalytic Conversion of C1 Substrates to Reduced Products Using Nitrogenase Bioelectrodes

This work was performed in collaboration with Professors Markus Ribbe and Yilin Hu. Dr. Johannes Rebelein, Dr. Nathaniel Sickerman, and Megan Newcomb prepared, isolated, and performed biochemical assays for the nitrogenase proteins used in this study.

3.1 Introduction

Nature utilizes complex biological enzymes to catalyze very specific reactions with a narrow scope of substrates.[1] The reactions can vary in speed, but are often performed at neutral pH, and ambient temperatures and pressures. Of the different classes of enzymes, metalloenzymes are among those that can perform oxidation/reduction reactions by transferring electrons through the metal centers at their active sites .[2-5]

To take advantage of their ability to perform unique redox reactions, enzymes have been integrated into electrochemical systems.[6-10] Integration of enzymes into electrochemical systems typically involves immobilizing the enzyme at the surface of an electrode.[11-16] Depending on the function of the enzyme, the electrode either acts as an anode (oxidizing the active site), or as a cathode (reducing the active site), which can then react with the substrate, turnover the catalyst, and generate product.

If the electronic communication between an electrode and an enzyme occurs directly from the electrode to the electroactive center of the enzyme, it is referred to as direct electron transfer (DET).[17-22] Alternatively, a small molecule with a reversible redox couple can shuttle

electrons between the electrode and the enzyme in a process called mediated electron transfer (MET).[23,24] MET is necessary when the electroactive center of the enzyme is deeply buried within the hydrophobic tertiary structure of the protein, and when there is no electron transport chain built into the enzyme to transfer an electron between a site at the surface of the protein and the active site. When the enzyme is performing an oxidative process, ferrocene and its derivatives are often the small molecule mediators of choice as its redox couple is reversible, adjustable to the oxidation potential of the enzyme through modification of its cyclopentadienyl rings, and is a stable under redox conditions.[25,26] Ferrocene can also be incorporated into redox active polymers used to immobilize enzymes on an electrode in order to mediate charge.[27] The mediator chosen for reductive processes is dependent on the reduction potential of the enzyme active site. Transition metal complexes containing Fe, Co, and Os metal ions, as well as organic compounds such as viologens or quinones, are known to be effective redox mediators for cathodic processes.[28-32]

An application for bioelectrodes in electrochemical cells is enzymatic biofuel cells, or fuel cells that utilize an enzyme as the catalyst to store or extract electrons in chemical fuels.[29,33-36] An advantage of these systems over commercial fuel cells utilizing synthetic catalysts is that the enzyme often demonstrates superior substrate and product specificity. Enzymatic biofuel cells also typically do not suffer from catalyst poisoning due to fuel-crossover between the membrane separating cathodic and anodic chambers, because the substrate for enzymatic biofuel cells are often biological molecules such as sugars, pyruvate, lactate, ethanol, or methanol;[35] in contrast, platinum cathodes in direct methanol fuel cells (DMFCs) are subject to catalyst poisoning by CO or fuel-crossover across the electrochemical cell membrane.[35,37,38]

Additionally, biofuel cells operate at ambient temperature, pressure, and neutral pH while synthetic systems often require elevated temperatures and highly acidic or basic conditions.[35]

Glucose oxidase is the model target enzyme in the study of anodic biofuel cells utilizing glucose as a fuel and can use ferrocene derivatives as a redox mediator to transport charge from the electrode surface to the enzyme.[8,29,39,40] In cathodic enzymatic fuel cells, it has been shown that multicopper enzymes such as bilirubin oxidase, laccase, and ascorbate oxidase can be used to reduce O_2 to H_2O.[41] Hydrogenase enzymes have also been utilized with DET systems to store electrons in H_2 by reducing H^+.[42-44] Recently the scope of cathodic enzymatic fuel cells were expanded by Minteer et al. to include nitrogenase proteins by adsorbing the component MoFe protein onto a glassy carbon electrode surface. Adsorption of the protein was accomplished by cross-linking the MoFe protein with a polymer, then utilizing the resulting protein bioelectrode to store electrons from an electrode into NO_2^- and N_3^- by forming NH_3.[45] To mediate charge from the electrode surface to the protein, cobaltocenium hexafluorophosphate (Cc^+) ($E_{½}$ = –1.21 V vs. SCE, pH 7.4)[46] was used.

As mentioned at the beginning of Chapter 2, Ribbe and coworkers demonstrated that the following C1 substrates: carbon monoxide, carbon dioxide, and sodium cyanide can be reduced by nitrogenase enzymes to hydrocarbon products using lanthanide reductants.[47-52] Over the last nine years, the Ribbe Lab has developed three different systems in which the nitrogenase enzymes can perform these transformations. An example of each system is depicted in Figure 3.1.

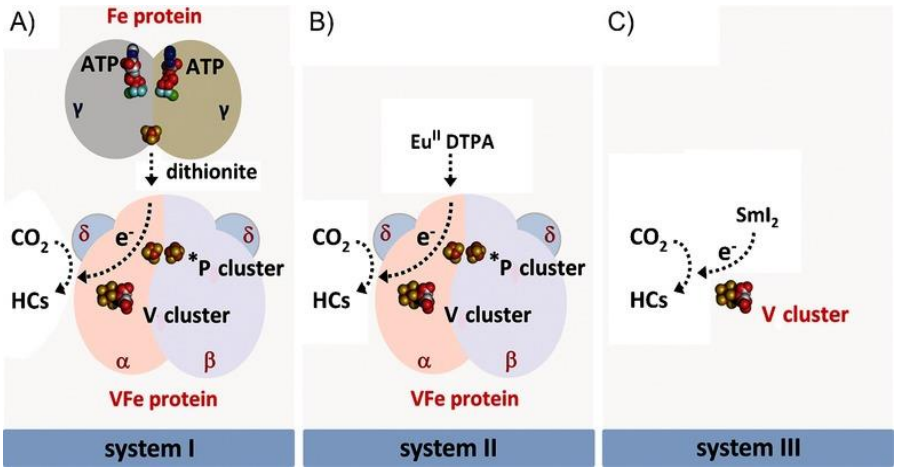

Figure 3.1: Examples of the three different nitrogenase systems used to reduce C1 substrates to hydrocarbons developed by Ribbe and coworkers. A) Full nitrogenase enzyme using sodium dithionite as a reductant. B) 1 component nitrogenase protein using a europium(II) reductant. C) Isolated nitrogenase metallocofactor using samarium(II) iodide as a reductant.

The system that is active under the mildest conditions, system 1 (Figure 3.1.A), utilizes the full nitrogenase protein, which includes the MoFe/Fe protein or the VFe/Fe protein complexes. Even though a mild chemical reductant such as sodium dithionite is used to reduce the enzyme, the hydrolysis of 2MgATP to 2MgADP + $2P_i$ is required to form the VFe/Fe protein complex. The formation of the VFe/Fe protein complex effects a conformational change driving electron transfer, making the overall process energetically expensive. Without the hydrolysis of ATP, the reduction potentials of the isolated VFe and MoFe proteins are shifted to more negative values resulting in the need for a much stronger reductant. System two (Figure 3.1.B) utilizes the isolated VFe, MoFe, or Fe component proteins individually. This model system does not use ATP to aid electron transfer to the protein. As a consequence, highly reducing lanthanide(II) reductants, such as Eu^{II}(DTPA) (DPTA = diethylenetriaminepentaacetic acid) (E_{pc} = –1.38 V vs. SCE),[53] are needed to transfer an electron to the P-cluster and subsequently to the V/M-clusters

to facilitate catalysis. Differential reactivity with C1 substrates between the nitrogenase proteins are observed in this system where VFe protein can much more efficiently convert CO, CO_2, and CN^- to hydrocarbons whereas MoFe protein and Fe protein can only reduce CO_2 to CO, mimicking the reactivity of a CO dehydrogenase.[52] Finally system three (Figure 3.1.C) utilizes just the isolated cofactors that were electrochemically studied in Chapter 2. All nitrogenase cofactors (M/V/L-clusters) are able to convert CO and CO_2 to hydrocarbons upon addition of SmI_2 ($E_{½}$ = –1.3 V vs. SCE (THF))[54] as a reductant and 2,6-lutidinium triflate as an acid source in organic solvent.[50,55] In all three systems described, the major catalytic product (~99% yield based on reductant) is H_2 from the direct reduction of protons.

The ATP requirement of system 1 makes the full nitrogenase protein much less useful in an electrocatalytic system unless a technique is developed to regenerate ATP *in situ* using ATP synthase. Homogeneous electrolysis of the metallocofactors used in system 3 is theoretically possible, but would be very challenging due to the inability to isolate high quantities of the metallocofactors as well as the metallocofactors' instability at room temperature. Therefore, system 2 is the ideal system with which to perform electrocatalytic studies by replacing the chemical reductant with an electrode and redox mediator. Because NO_2^- and N_3^- were already reduced in the previously mentioned study by a nitrogenase MoFe protein bioelectrode in a polymer-anchored system utilizing a redox mediator,[45] it was hypothesized that if VFe protein can be interfaced with an electrode using this same technique, then CO and CO_2 reduction to hydrocarbons will be possible.

Interfacing nitrogenase proteins with an electrode presents unique challenges. Direct electron transfer from an electrode to any of the nitrogenase protein metalloclusters is not possible due to the insulating amino acid residues surrounding them. Although the europium(II)

reductants used in Figure 3.1.B are electrochemically reversible, their $Eu^{3+/2+}$ reduction potentials are too negative for aqueous buffers compatible with nitrogenase proteins when using non-mercury electrodes between pH 7-8. The negative potentials required to reduce Eu^{III}DTPA causes competition with the reduction of protons to dihydrogen when reduction is attempted with carbon-based electrodes that are required for immobilization of nitrogenase proteins.

To decouple the requirement of lanthanide-based chemical reductants from the catalytic reduction of C1 substrates to hydrocarbons using nitrogenase proteins, electrocatalytic reduction of CO and CO_2 with nitrogenase component proteins using the polymer immobilization technique that was previously successful with the MoFe protein was performed. Characterization of the products of reduction was also attempted. It was originally unknown whether VFe protein would be a good candidate for the polymer immobilization technique initially used by Minteer et al. due to the differences in quarternary structure between the MoFe and VFe proteins. The additional delta proteins (seen in Figure 3.1.A-B) that VFe protein possesses are not present in MoFe protein and led to uncertainty in the application of the technique.[56,57] Therefore in order to verify that VFe protein could be used with the polymer adsorption technique its reactivity with NO_2^- and N_3^- was first examined. Additionally, MoFe protein's reactivity with these substrates was also reproduced from previous literature to verify that the surfaces were fabricated correctly and are functional in this study.

When interpreting the voltammograms in this work, note that the observed current response is solely due to electronic communication between the cobaltocenium cation used to mediate electron transfer and the electrode (Figure 3.2). The glassy carbon electrode has no observable direct electron transfer with the protein that is adsorbed to its surface through the cross-linked poly(vinylamine) polymer.

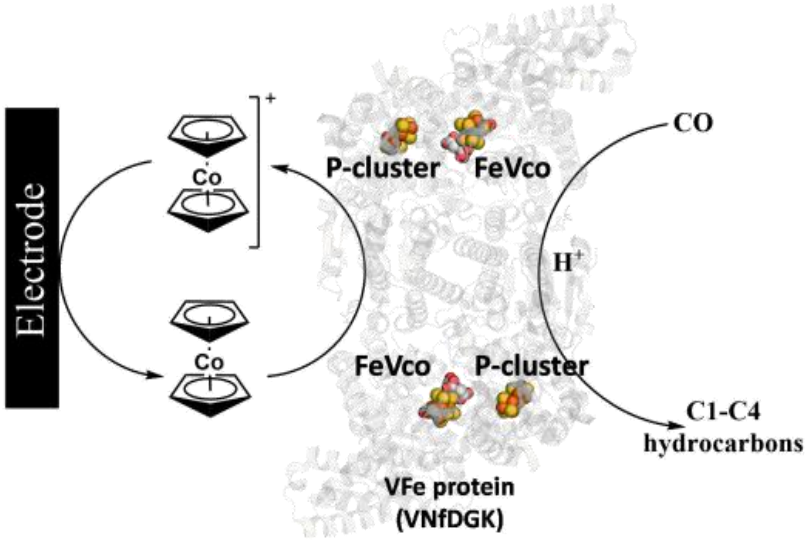

Figure 3.2: Electron transfer between a glassy carbon electrode and VFe protein mediated by Cc^{+} in order to reduce CO and H^{+} into proposed hydrocarbon products.

3.2 Results and discussion

3.2.1 Reduction of sodium nitrite

Sodium nitrite is a known alternative substrate for nitrogenase proteins. Upon 6 proton, 7 electron reduction of NO_2^- with the nitrogenase enzymes (eq 1), NH_3 is generated with concomitant formation of water instead of H_2, in contrast to Mo-nitrogenase's normal function (eq 2).[58,59]

$$NO_2^- + 6e^- + 12MgATP + 7H^+ \longrightarrow NH_3 + 2H_2O + 12MgADP + 12P_i \quad (1)$$

$$N_2 + 8e^- + 16MgATP + 8H^+ \longrightarrow 2NH_3 + H_2 + 16MgADP + 16P_i \quad (2)$$

Electrocatalytic reduction of sodium nitrite by three different nitrogenase component proteins and a glassy carbon control are shown in Figure 3.3. The dark red traces in Figure 3.3 represent the prepared bioelectrode exposed to the buffered aqueous solution with no electron mediator or substrate. In each example, this dark red trace presented a low level of current

density, consistent with no electron transfer at the electrode surface. When the NO_2^- substrate is added to each system (light red trace), a similar current density ca. 50 uA/cm^2 across each condition is observed. An exception to this is MoFe protein which displays a voltammogram with significant current density at –1.36 V vs. SCE, but still presents a similar trend relative to the other proteins. This exception with NO_2^- and MoFe protein was also observed by Minteer and coworkers.[45] When mediator was present but in the absence of substrate (dark blue trace), the glassy carbon electrode (Figure 3.3.d) demonstrates ideal reversible behavior. In contrast, when the NO_2^- substrate is added in the presence of mediator, every prepared electrode produces an increase in cathodic current density. Although there is a slight increase in cathodic current density upon addition of $NaNO_2$ to the control using polished glassy carbon as the electrode in the presence of Cc^+, the change in net current density is negligible to the samples probed containing the protein bioelectrodes.

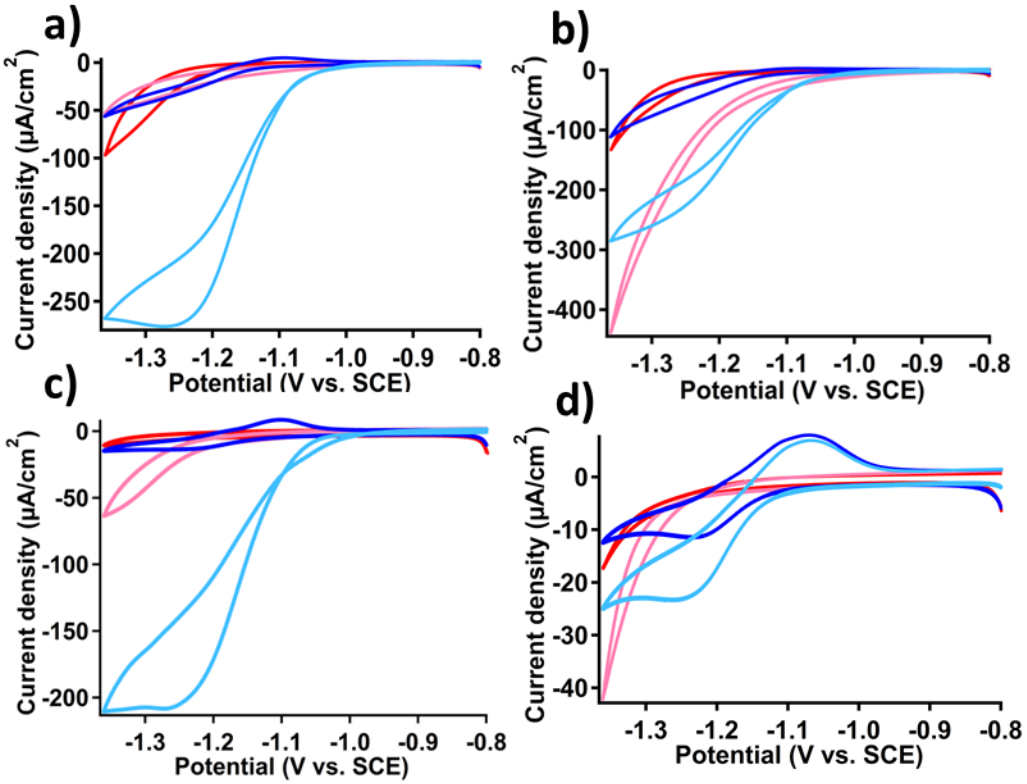

Figure 3.3: Cyclic voltammograms of nitrogenase bioelectrodes using $NaNO_2$ as a substrate and $[(C_5H_5)_2Co][PF_6]$ (Cc^+) as an electron mediator. a) VFe protein, b) MoFe protein, c) apo MoFe protein, and d) No protein, glassy carbon control. Working electrode: protein bioelectrode specified in the figure caption; counter electrode: glassy carbon rod; reference electrode: saturated calomel electrode. Electrochemical cell contains 50 mM $NaNO_2$, 50 mM pH 7.4 HEPES buffer, 180 µM Cc^+ and 500 mM NaCl. Voltammograms were obtained at a scan rate of 2 mV/s. **Dark red**: no substrate and no mediator. **Light red**: with substrate and no mediator. **Dark blue**: no substrate and with mediator. **Light blue**: with substrate and with mediator.

Table 3.1: Tabulated onset and peak potential current densities of the $Cc^{+/0}$ reduction potential for nitrogenase protein bioelectrodes and polished glassy carbon in the presence of sodium nitrite. H^+ as a substrate refers to the reduction of the aqueous media in the absence of sodium nitrite.

Substrate	H^+		$NaNO_2$		Net current density $ipc_{NaNO2} - ipc_{H+}$ ($\mu A/cm^2$)
Protein	Onset Potential (V vs. SCE)	i_{pc} ($\mu A/cm^2$) at E= –1.26 V	Onset Potential (V vs. SCE)	i_{pc} ($\mu A/cm^2$) at E= –1.26 V	
VFe	–1.17	–36	–1.04	–276	–240
MoFe	–1.12	–61	–1.04	–239	–178
Apo MoFe	–	–14	–1.04	–208	–194
Control: No Protein	–	–11	–	–23	–12

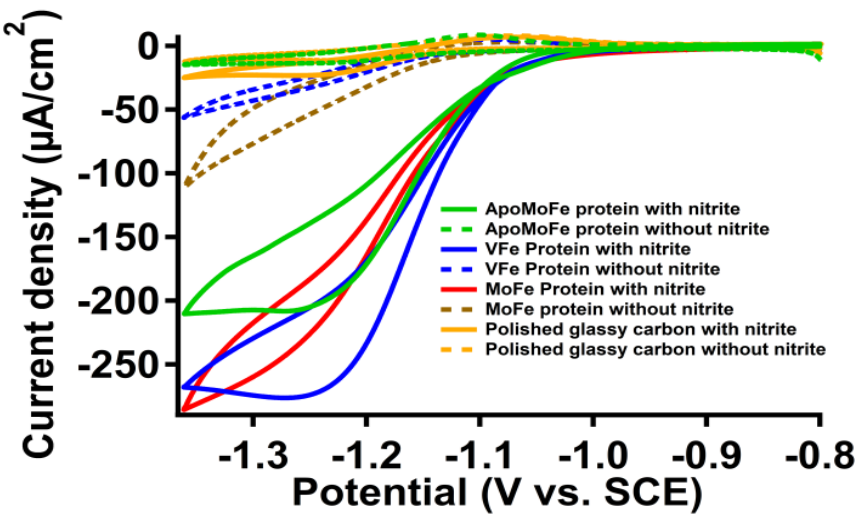

Figure 3.4: Cyclic voltammograms for the electrocatalytic reduction of sodium nitrite. Dashed lines represent conditions in which the electrode is not in the presence of nitrite anion. Solid lines represent the electrode conditions with substrate. Working electrode: protein bioelectrode specified in the figure legend; counter electrode: glassy carbon rod; reference electrode: saturated calomel electrode. Electrochemical cell contains 50 mM pH 7.4 HEPES buffer, 180 μM Cc^{+} and 500 mM NaCl. Voltammograms were obtained at a scan rate of 2 mV/s.

Table 3.1 provides tabulated values for onset potential (i.e. the potential at which the current density begins to increase in magnitude) and peak current densities for the reduction of NO_2^-. The net current density is the peak current density in the presence of substrate subtracted by the peak current density in the absence of substrate at the potential in which the peak current density in the presence of substrate was measured. Across all substrates in this study, if an increase in current density is observed with mediator, but in the absence of substrate, the increase in current is attributed to proton reduction of the aqueous medium to dihydrogen (eq 3) facilitated by the protein bioelectrode.

$$2H^+ + 2e^- \longrightarrow H_2 \quad (3)$$

Among the three proteins tested, VFe protein has the highest net current density with the substrate NO_2^-, with a value of –240 μA/cm^2. Similarly to what was observed in Minteer et al., apo MoFe protein provided an increase in current density suggesting that the M-cluster is not

required for this transformation. Furthermore in this study, apo MoFe protein performed better (i.e. had a larger net current density) than MoFe protein, but not compared to the VFe protein. Figure 3.4 shows a direct comparison of the three protein bioelectrodes using sodium nitrite as a substrate. The dashed traces in Figure 3.4, show both the partially reversible redox event of the Cc^{+}.

Application of a cathodic potential on a 50 mM $NaNO_2$ solution with a polished glassy carbon electrode provided an inaccurate cathodic current density signified by the presence of multiple current crossover events and uncharacteristically high current values obtained. The inaccurate current density was likely due to the 1:10 analyte:electrolyte concentration causing mass transport problems to the electrode; for proper diffusion of the electroactive analyte species to an electrode, an ideal analyte:electrolyte ratio of 1:100 should be employed to negate the effects of mass transfer by migration.[60] Problems with diffusion were not observed in the experiments utilizing bioelectrodes, likely due to the thin polymer/protein film on the surface of the electrode. In order to remedy the diffusion issue, the concentration of $NaNO_2$, when only exposed to glassy carbon (Figure 3.3.d), was lowered from 50 mM to 10 mM to help maintain a diffusion-controlled system at the electrode. Although the change in concentration is not ideal for using polished glassy carbon as a control for the protein systems with the $NaNO_2$ substrate, the lack of electrocatalytic current from the experiments utilizing a glassy carbon electrode suggests the reductive current observed in Figures 3.3.a-c is caused by electrocatalysis facilitated by the protein bioelectrodes and not the carbon surface. Slight diffusion/mass transport issues were observed in the bioelectrode examples as seen in the crossover of anodic and cathodic waves at –1.08 V vs. SCE in the VFe protein bioelectrode, but do not interfere with conclusions from the data.

3.2.2 Reduction of sodium azide

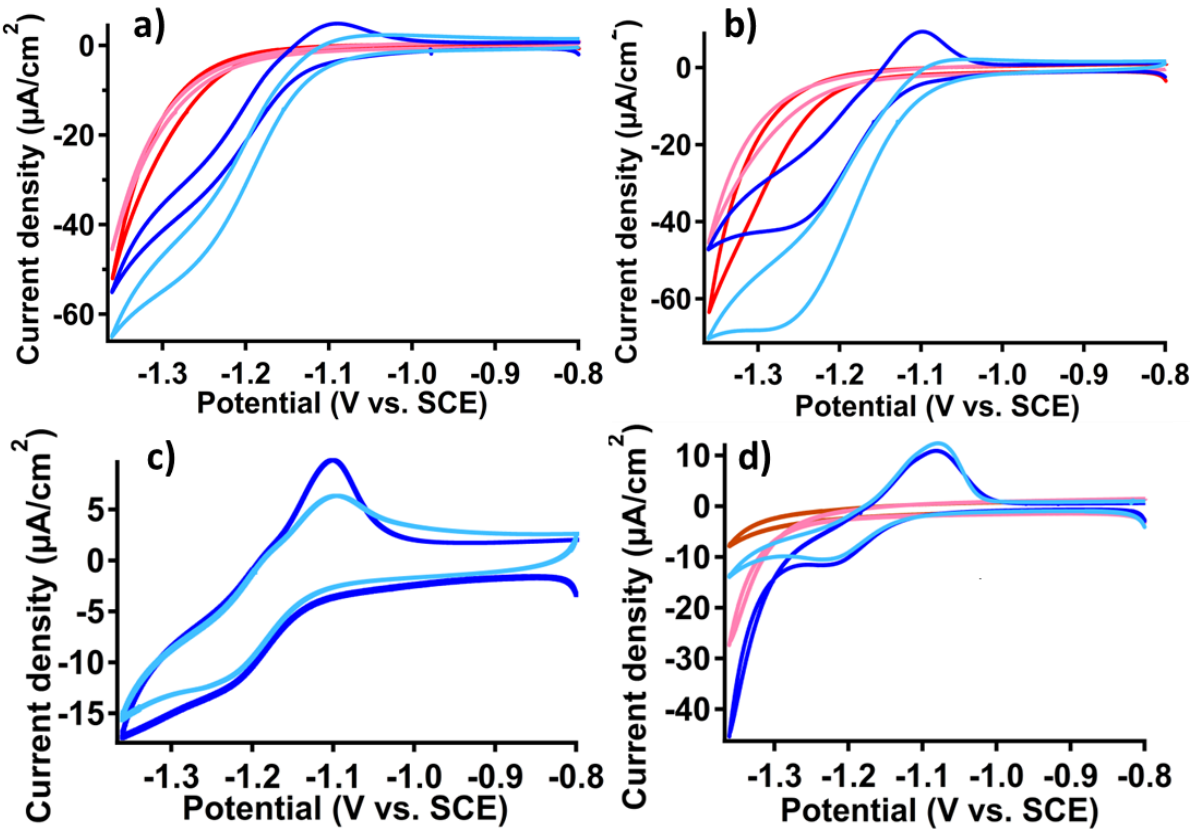

Figure 3.5: Cyclic voltammograms of nitrogenase bioelectrodes using NaN_3 as a substrate and $[(C_5H_5)Co][PF_6]$ as an electron mediator. a) VFe protein, b) MoFe protein, c) apo MoFe protein (data for the absence of mediator was not obtained for this substrate with apo MoFe protein), and d) No protein, glassy carbon control. Working electrode: protein bioelectrode specified in the figure caption; counter electrode: glassy carbon rod; reference electrode: saturated calomel electrode. Electrochemical cell contains 50 mM NaN_3, 50 mM pH 7.4 HEPES buffer, 180 µM Cc^+ and 500 mM NaCl. Voltammograms were obtained at a scan rate of 2 mV/s. **Dark red**: no substrate and no mediator. **Light red**: with substrate and no mediator. **Dark blue**: no substrate and with mediator. **Light blue**: with substrate and with mediator.

Table 3.2: Tabulated onset and peak potential current densities for the $Cc^{+/0}$ reduction potential for nitrogenase protein bioelectrodes and polished glassy carbon in the presence of sodium azide. H^+ as a substrate refers to the reduction of the aqueous media in the absence of sodium azide.

Substrate	H^+		NaN_3		Net peak current density ipc_{NaN3} - ipc_{H+} (µA/cm^2)
Protein	Onset Potential (V vs. SCE)	i_{pc} (µA/cm^2) at E= –1.29 V	Onset Potential (V vs. SCE)	i_{pc} (µA/cm^2) at E= –1.29 V	
VFe	–1.15	–39	–1.11	–54	–15
MoFe	–1.12	–42	–1.08	–68	–26
Apo MoFe	–	–15	–	–13	2
Control: No Protein	–	–11	–	–10	1

Sodium azide was used as the second substrate for this study. Sodium azide's ATP-dependent reduction to NH_3, facilitated by Mo- and V-nitrogenase, proceeds through the 8 electron, 9 proton pathway shown in eq 4.[61,62] During the chemical reduction of sodium azide, Mo- and V-nitrogenase require the hydrolysis of 5.3 and 5.6 MgATP:$2e^-$ for turnover respectively.

$$N_3^- + 8e^- + 9H^+ \longrightarrow 3NH_3 \quad (4)$$

The ATP-independent current response during the electrocatalytic reduction of sodium azide was measured using VFe, MoFe, apo MoFe protein bioelectrodes. A polished glassy carbon electrode was again used as a control. Cyclic voltammetry of each protein is seen in Figure 3.5. The dark red and light red traces in the voltammograms of Figure 3.5.a and 3.5.b are nearly identical, indicating that sodium azide is not reduced at the electrode surface in the electrochemical window of the experiment. However, it should be noted that in the control experiment utilizing a glassy carbon electrode that the electrochemical window is shifted anodically after the addition of sodium azide. The anodic shift of the electrochemical window is similar to what was observed with sodium nitrite and indicates that proton reduction to dihydrogen is occurring at a milder potential than prior to the addition of substrate. The shift of the electrochemical window does not affect the onset potential of the Cc^+ mediator for electrocatalysis with the protein bioelectrodes and the maximum current density recorded for the glassy carbon control does not exceed the peak current densities observed for MoFe and VFe protein bioelectrodes in the presence of NaN_3.

Upon addition of Cc^+ to the aqueous buffer containing the bioelectrodes, changes in the electrochemical response are observed. In the glassy carbon control shown in Figure 3.5.d, the addition of sodium azide had no effect on the reduction and oxidation of the $Cc^{+/0}$ redox couple

indicating no electrocatalysis is taking place. Similarly in apo MoFe protein, shown in Figure 3.5.c, the addition of the N_3^- substrate did not affect the electrochemical response of the $Cc^{+/0}$ couple, indicating that apo MoFe protein is not a catalyst for this reaction, differing from NO_2^-. In contrast to the glassy carbon and apo MoFe protein results, addition of Cc^+ and the azide substrate to the electrochemical cells containing VFe and MoFe protein bioelectrodes resulted in catalytic current upon sweeping the potential from –0.8 to –1.36 V *vs.* SCE. Prior to the addition of sodium azide to these electrochemical cells, the dark blue traces in Figure 3.5.a and 3.5.b show a drop in current density and retain their oxidative waves, consistent with proton reduction in these electrochemical cells across all substrates.

As mentioned before, the current response is only an interaction between the mediator and the electrode. When the oxidative wave is no longer observed (Figures 3.5.a-b), it indicates that upon reduction of the mediator by the electrode, the mediator subsequently transfers that electron directly to the protein to perform catalysis. The protein oxidizes the mediator back to cobaltocenium. Therefore upon reversing the potential at a scan rate of 2 mV/s, there was no detectable amount of reduced mediator present in solution to be reoxidized at the electrode. Loss of the anodic signal is only present in samples containing mediator, substrate, and MoFe/VFe proteins indicating an electrocatalytic process.

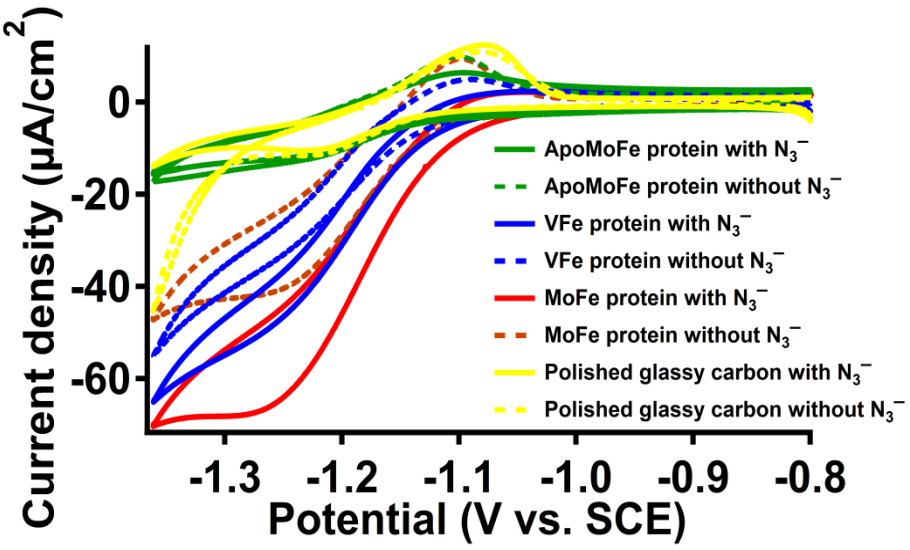

Figure 3.6: Cyclic voltammograms for the electrocatalytic reduction of sodium azide. Dashed lines represent conditions in which the electrode is not in the presence of azide anion. Solid lines represent the electrode conditions with substrate. Working electrode: protein bioelectrode specified in the figure legend; counter electrode: glassy carbon rod; reference electrode: saturated calomel electrode. Electrochemical cell contains 50 mM pH 7.4 HEPES buffer, 180 μM Cc^+ and 500 mM NaCl. Voltammograms were obtained at a scan rate of 2 mV/s.

The MoFe protein demonstrated more activity towards the reduction of sodium azide than the VFe protein. These results are consistent with a prior study from Newton et al. who found that approximately 4 times more NH_3 is produced from ATP-dependent Mo-nitrogenase than V-nitrogenase systems when sodium azide is the substrate.[62] In this electrocatalytic ATP-independent system, MoFe protein displayed approximately 2 times the current density of VFe protein (Table 3.2). The cyclic voltammograms using sodium nitrite and sodium azide as substrates show that VFe protein can be applied as a bioelectrode through this technique despite its structural differences from MoFe protein. Results with and without Cc^+ are overlaid in Figure 3.6.

3.2.3 Reduction of carbon monoxide

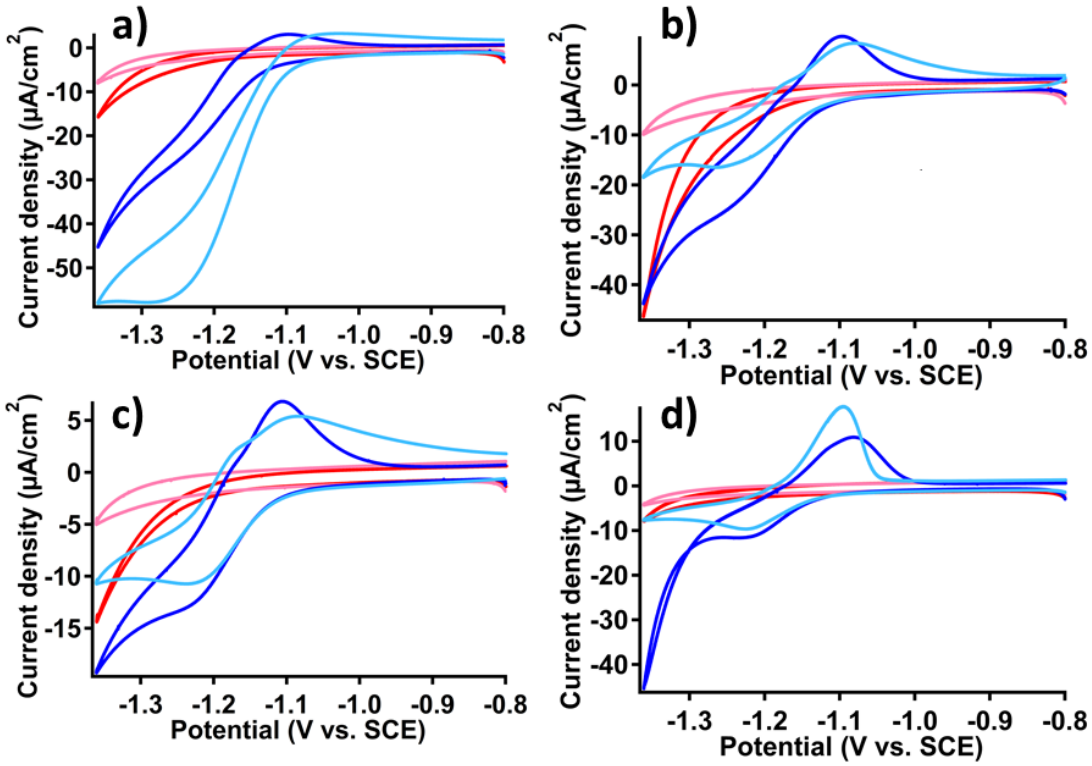

Figure 3.7: Cyclic voltammograms of nitrogenase bioelectrodes using CO as a substrate and $[(C_5H_5)Co][PF_6]$ as an electron mediator. a) VFe protein, b) MoFe protein, **c)** apo MoFe protein, and **d)** No protein, glassy carbon control. Working electrode: protein bioelectrode specified in the figure caption; counter electrode: glassy carbon rod; reference electrode: saturated calomel electrode. Electrochemical cell contains saturated CO, 50 mM pH 7.4 HEPES buffer, 180 μM Cc^+ and 500 mM NaCl. Voltammograms were obtained at a scan rate of 2 mV/s. **Dark red**: no substrate and no mediator. **Light red**: with substrate and no mediator. **Dark blue**: no substrate and with mediator. **Light blue**: with substrate and with mediator.

Table 3.3 Tabulated onset and peak potential current densities for the $Cc^{+/0}$ reduction potential for nitrogenase protein bioelectrodes and polished glassy carbon in the presence of CO. H^+ as a substrate refers to the reduction of the aqueous media in the absence of CO.

Substrate	H^+		CO		Net peak current density ipc_{CO} - ipc_{H+} ($\mu A/cm^2$)
Protein	Onset Potential (V)	i_{pc} ($\mu A/cm^2$) at E= –1.28 V	Onset Potential (V)	i_{pc} ($\mu A/cm^2$) at E= –1.28 V	
VFe	–1.15	–28.3	–1.10	–57.8	–29.5
MoFe	–1.15	–27.9	–1.16	–16.2	11.7
ApoMoFe	–1.16	–14.2	–1.16	–10.4	3.8
Control: No protein	–	–12.2	–	–8.0	4.2

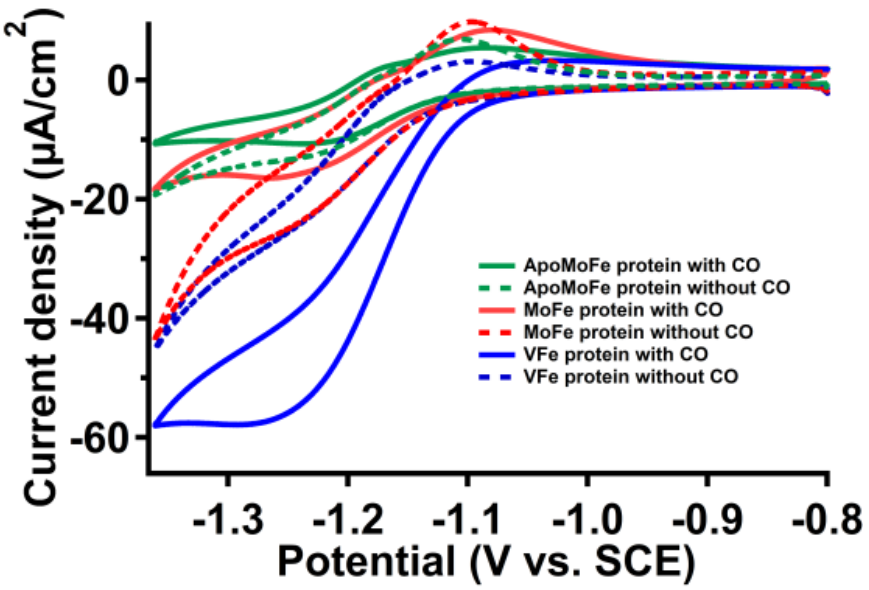

Figure 3.8: Cyclic voltammograms of the reduction of carbon monoxide. Dashed lines represent conditions in which the protein bioelectrode is not in the presence of CO. Solid lines represent protein bioelectrode with substrate. Working electrode: specific protein bioelectrode described in the figure legend; counter electrode: glassy carbon rod; reference electrode: saturated calomel electrode. Cell contains 50 mM pH 7.4 HEPES buffer, 180 μM Cc^+ and 500 mM NaCl. Voltammograms were obtained at a scan rate of 2 mV/s.

Successful adaptation of this bioelectrode technique to the VFe protein allows for expansion of this study to include substrates of interest for energy storage research. Nitrogenase protein bioelectrodes used for the reduction of CO produced results that were consistent with the experiments using lanthanide(II) chemical reductants mentioned previously. When no substrate is added (Figure 3.7, dark red traces) similar behavior to the previously prepared electrodes was noted. Interestingly, in all examples with no mediator present (red), the current density decreased to –1.36 V. vs. SCE upon addition of CO, suggesting inhibition of the proton reduction reaction near the electrochemical window of the buffer. Our first thought was that CO bubbles were potentially passivating the surface of the electrode causing this effect, however the analyte solution was saturated with CO prior to introduction of the electrodes. Another hypothesis was that CO, a known competitive inhibitor of nitrogenase, was binding to the nitrogenase enzymes

and preventing proton reduction. In nitrogenase systems, H^+ is the only substrate not inhibited by the presence of CO at the active site, therefore a decrease in current density by introduction of CO would not be explained by inhibition.[63] The decrease in current density is also seen in the glassy carbon control (Figure 3.7.d) indicating that the cause of the effect is not protein-based. The cause of this effect is still unknown.

When CO was introduced to the MoFe and apo MoFe protein (Figure 3.7.b and Figure 3.7.c), the net current density became more positive upon addition of CO by 11.7 and 3.8 $\mu A/cm^2$ respectively. The decrease in cathodic current density after substrate was added and in the presence of mediator with the MoFe and apo MoFe bioelectrode experiments behaved in the same manner as the dark/light red traces in Figure 3.8, or without the addition of mediator. Additionally, lack of an increase of current density of the cathodic peak with and without substrate, retention of the anodic wave of the Cc^+ mediator, and no significant change in onset potential confirmed that no electrocatalytic activity was occurring at the surfaces of these electrodes.

VFe protein is the only protein that demonstrated activity toward the CO substrate. Upon addition of the CO substrate, the net current density for the VFe protein bioelectrode became shifted by –29.5 $\mu A/cm^2$ (Figure 3.7.a). Additionally, the anodic wave was completely absent, suggesting Cc^+ was continuously oxidized by the protein facilitating catalysis and not the electrode on the return sweep of the potential. The overlaid voltammogram of each protein system is seen in Figure 3.8 to further demonstrate the lone reactivity of the VFe protein with CO. This result is significant because it mirrors reactivity seen in biological assays using chemical reductants.[51] Although the full molybdenum nitrogenase can convert CO to hydrocarbons in an ATP-dependent system, it does so at a much lesser rate than vanadium

nitrogenase.[64] Consistent with assays involving chemical reductants, the MoFe protein does not facilitate the transformation of CO to reduced products.

3.2.4 Reduction of carbon dioxide

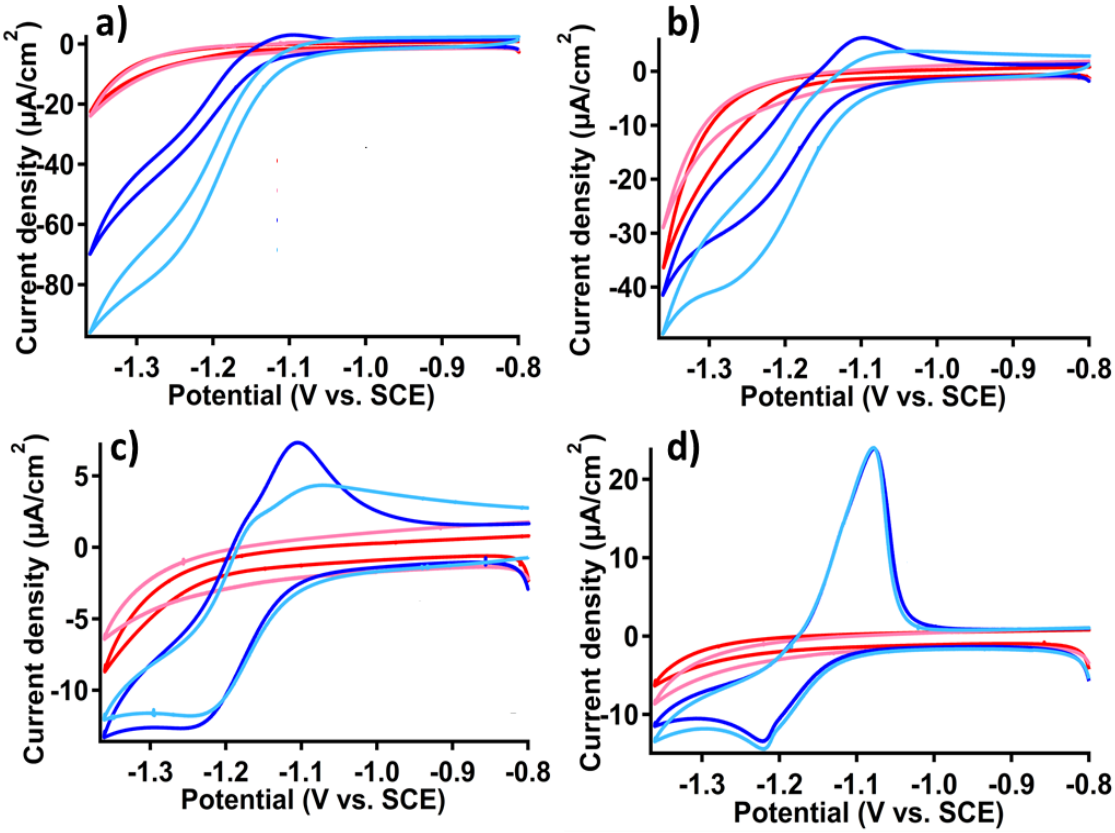

Figure 3.9: Cyclic voltammograms of nitrogenase bioelectrodes using CO_2 as a substrate and $[(C_5H_5)Co][PF_6]$ as an electron mediator. a) VFe protein, b) MoFe protein, c) apo MoFe protein, and d) No protein, glassy carbon control. Working electrode: protein bioelectrode specified in the figure caption; counter electrode: glassy carbon rod; reference electrode: saturated calomel electrode. Cell contains saturated CO_2, 50 mM pH 7.4 HEPES buffer, 180 μM Cc^+ and 500 mM NaCl. Voltammograms were obtained at a scan rate of 2 mV/s. **Dark red**: no substrate and no mediator. **Light red**: with substrate and no mediator. **Dark blue**: no substrate and with mediator. **Light blue**: with substrate and with mediator.

Table 3.4: Tabulated onset and peak potential current densities for the $Cc^{+/0}$ reduction potential for nitrogenase protein bioelectrodes and polished glassy carbon in the presence of carbon dioxide. H^+ as a substrate refers to the reduction of the aqueous media in the absence of CO.

Substrate	H^+		CO_2		Net peak current density ipc_{CO2} - ipc_{H+} ($\mu A/cm^2$)
Protein	Onset Potential (V)	i_{pc} ($\mu A/cm^2$) at E= –1.30 V	Onset Potential (V)	i_{pc} ($\mu A/cm^2$) at E= –1.30 V	
VFe	–1.15	–50	–1.09	–81.5	–31.5
MoFe	–1.10	–31.5	–1.06	–41	–9.5
apo MoFe	–	–12.6	–	–11.6	1
Control: No protein	–	–13	–	–14	–1

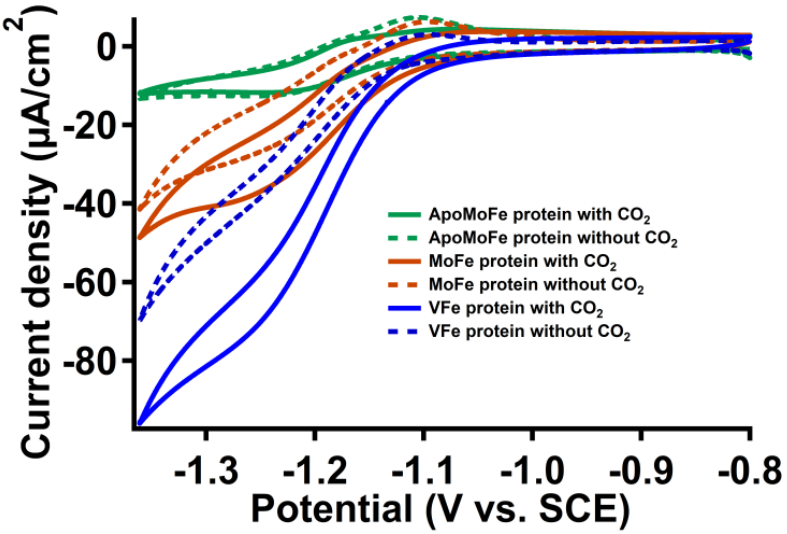

Figure 3.10: Cyclic voltammograms of the reduction of carbon dioxide. Dashed lines represent conditions in which the protein bioelectrode is not in the presence of nitrite anion. Solid lines represent protein bioelectrode with substrate. Working electrode: specific protein bioelectrode specified in the figure legend; counter electrode: glassy carbon rod; reference electrode: saturated calomel electrode. Electrochemical cell contains 50 mM pH 7.4 HEPES buffer, 180 μM Cc^+ and 500 mM NaCl. Voltammograms were obtained at a scan rate of 2 mV/s.

The last substrate analyzed with the nitrogenase bioelectrode system was carbon dioxide. Cyclic voltammograms for electrocatalytic reduction of CO_2 can be found in Figure 3.9. Like with the previous substrates, addition of CO_2 to the analyte solutions, without mediator, results in no change in net current density of the system. Similarly, studies using apo MoFe protein and

polished glassy carbon alone (Figure 3.9.c and 3.9.d respectively) were unchanged upon addition of CO_2 when mediator was present in the solution suggesting no reactivity or interaction with the substrate took place. VFe and MoFe protein bioelectrodes demonstrate an increased current in the presence of CO_2 compared to when it is not present, loss of the anodic return waves, and positive shifts in the onset potential by 60 and 40 mV respectively consistent with electrocatalysis (Table 3.4). CO_2 does not appear to cause the same "inhibiting" effect on H^+ reduction as CO described in the previous section. Figure 3.9 shows cyclic voltammograms before and after the addition of CO_2. While some conditions in Figure 3.9 experienced no change in cathodic current density indicative of no electrocatalysis taking place, there were no conditions where cathodic current density was significantly decreased upon addition of CO_2. A concern while running reactions with CO_2 is acidification of the buffered media; however testing the pH before and after addition of CO_2 confirmed that the pH remained constant. Also, no change in the behavior of the electrochemical window of the apo MoFe protein and polished glassy carbon control were observed, further suggesting that a change in pH of the analyte solution is not the cause of the increased cathodic current density upon adding CO_2 to the VFe and MoFe protein bioelectrode systems. The electrochemical activity observed here is consistent with biological assays for CO_2 reduction using these proteins.[64]

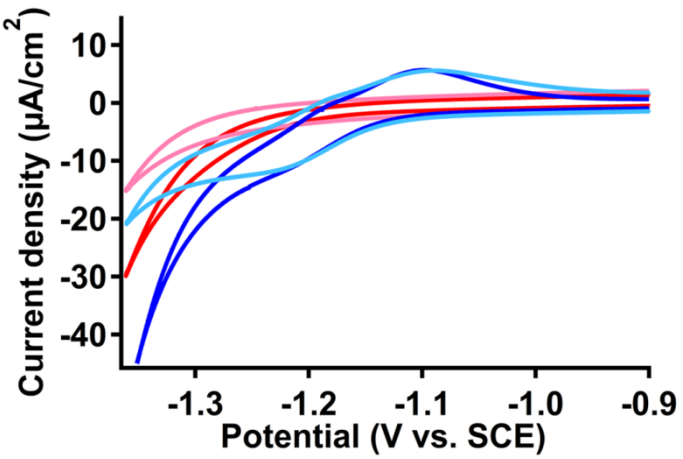

Figure 3.11: Cyclic voltammograms for the electrocatalytic reduction of carbon dioxide using an Fe protein bioelectrode as the working electrode. **Dark red**: no substrate and no mediator. **Light red**: with substrate and no mediator. **Dark blue**: no substrate and with mediator. **Light blue**: with substrate and with mediator. Counter electrode: glassy carbon rod; reference electrode: saturated calomel electrode. Electrochemical cell contains 50 mM pH 7.4 HEPES buffer, 180 μM Cc^+ and 500 mM NaCl. Voltammograms were obtained at a scan rate of 2 mV/s.

Ribbe and coworkers have observed catalytic CO_2 reduction activity with the Fe protein.[65] Therefore it was tested for its ability to reduce CO_2 using the bioelectrocatalysis technique utilized in this study. Figure 3.11 shows that the Fe protein, when prepared as a bioelectrode in the same fashion as the VFe and MoFe protein does not exhibit any electrocatalytic current in the presence of CO_2. The lack of enhanced reductive current does not necessarily mean the Fe protein is inactive towards CO_2 reduction. Reformulating the ratio of polymer:cross-linking-agent:protein may be required as the protocol is currently optimized for the VFe and MoFe proteins. Additionally, use of a different mediator for the Fe protein may required.

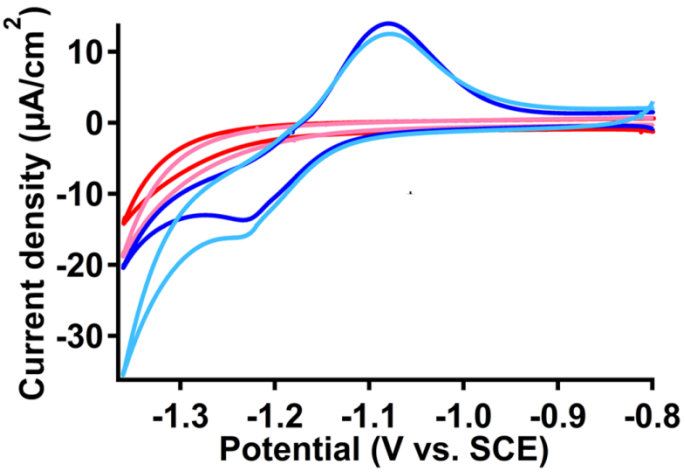

Figure 3.12: Cyclic voltammograms for the electrocatalytic reduction of carbon dioxide using a polymer coated carbon working electrode. **Dark red**: no substrate and no mediator. **Light red**: with substrate and no mediator. **Dark blue**: no substrate and with mediator. **Light blue**: with substrate and with mediator. Counter electrode: glassy carbon rod; reference electrode: saturated calomel electrode. Electrochemical cell contains 50 mM pH 7.4 HEPES buffer, 180 μM Cc^+ and 500 mM NaCl. Voltammograms were obtained at a scan rate of 2 mV/s.

As a negative control, a mixture containing two portions of polymer and one portion of crosslinking agent, without protein, was drop cast onto a glassy carbon electrode. This electrode was analyzed in the same manner as the protein bioelectrodes to rule out any potential non-innocent reactivity toward the substrates by the polymer. Figure 3.12 shows that upon addition of CO_2 there is a slight drop in current density. However if the current is measured from the peak cathodic current of Cc^+ as was the case with the bioelectrodes, it is noted that the slight increase in cathodic current density is consistent with the glassy carbon control. This result suggests that the polymer mixture adsorbing the proteins to the glassy carbon electrode surface is not reacting with the cobaltocenium mediator or the substrates added in this study. This control and the experiments using only glassy carbon confirm the hypothesis that that the proteins utilized in the bioelectrode systems are responsible for the reactivity seen in this study.

3.2.5 Attempts at product characterization from carbon monoxide reduction

Although cyclic voltammetry is a useful technique for determining whether catalytic activity is occurring at an electrode, it cannot characterize the products that are being formed during oxidation or reduction. Controlled potential electrolysis was performed in tandem with gas chromatography in an attempt to characterize the gaseous products of CO reduction.

A typical electrochemical cell for electrolysis requires two chambers, one chamber containing the working electrode (i.e. the bioelectrode in this study) with the reference electrode (separated from the bulk analyte solution by a frit), and a second chamber containing the counter electrode. These two chambers are separated by a fine frit or salt bridge to allow the exchange of ions to maintain charge balance, but not the reactants or products of electrolysis. Initial attempts at controlled potential electrolysis involved a single chambered cell because the hydrocarbon products that were hypothesized to form from CO reduction are not redox active and therefore would not be reoxidized at the counter electrode upon formation. Early attempts also used the same 3 mm glassy carbon electrodes used for the cyclic voltammetry experiments, but they did not contain enough bioelectrode surface area to generate sufficient current for product detection.

Glassy carbon rods with more surface area were coated with the cross-linked protein-polymer suspension and used for electrolysis. Although not quantified, hydrocarbon products ranging from methane to butane were detected *via* gas chromatography with methane as the major carbonaceous product seen in Figure 3.13. Unfortunately the results of these electrolyses were inconsistent over multiple trials producing variable relative areas of the gaseous products. The variance in the results has been attributed to multiple possible sources including cobalt nanoparticle formation at the electrode from the Cc^{+} mediator, inconsistent application of the protein-polymer suspension to the electrode due to the change in geometry from a disk to a rod,

oxygen contamination from adding CO, and/or leaks in the electrolysis cell or syringes used for chromatography. Despite variable quantities of products measured from electrolysis using the VFe protein bioelectrode, no hydrocarbon products were detected if 1) no CO was added, 2) no Cc^+ mediator was added, or 3) an apo MoFe protein bioelectrode was used in the presence of CO and the mediator. In should be noted that in control experiments that contained any combination of protein and mediator, significant current was still passed during electrolysis due to the generation of dihydrogen *via* equation 3 confirmed through gas chromatography. The above controls indicate that the hydrocarbons measured originate from the CO substrate and that the VFe protein and the mediator are required to produce them.

In an attempt to solve the problem of variability in the product distribution by gas chromatography, a new two-chambered low-volume cell was designed containing a compartment for low volumes of mercury to amalgamate Co nanoparticles formed during electrolysis. This new electrochemical cell produced much lower quantities of hydrocarbons than previously observed and still resulted in inconsistent product quantities. A study by Seefeldt and coworkers was published during this work that validated reduction of CO_2 to formate by the MoFe protein using this bioelectrode methodology.[66] In this study, the authors added a small amount of pyrene as a stabilizer to prevent Cc^+ from depositing onto the electrode upon reduction.

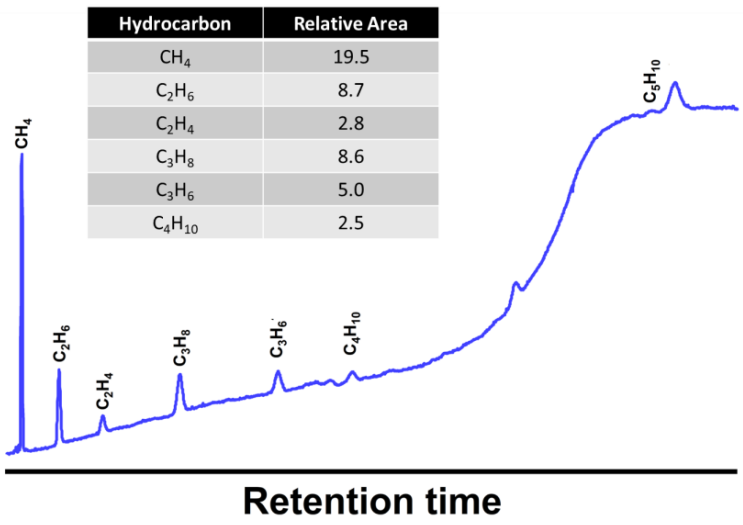

Figure 3.13: Example post-controlled potential electrolysis gas chromatograph utilizing a VFe protein bioelectrode and CO as the substrate. Potential set to –1.27 V vs. SCE for 15.5 hours. Total charge passed: –1.742 C.

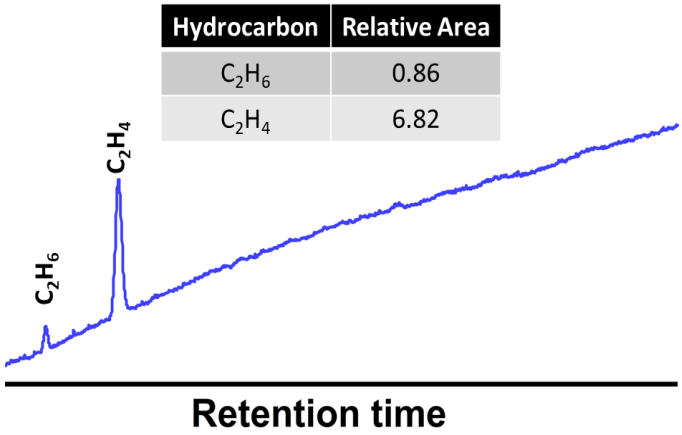

Figure 3.14: Example post-controlled potential gas utilizing a two-chambered electrochemical cell with a VFe protein bioelectrode and CO as the substrate with addition of pyrene into the bioelectrode suspension. Potential set to –1.26 V vs. SCE for 17 hours. Total charge passed: –5.220 C.

Pyrene was added into the VFe protein bioelectrode suspension to coat onto a glassy carbon rod electrode. Electrolysis experiments utilizing the addition of pyrene into the bioelectrode suspension produced two peaks *via* gas chromatography after electrolysis. Ethylene

and ethane were detected (Figure 3.14) and their relative quantities are consistent with product profiles from biological assays utilizing VFe protein and lanthanide reductants. To ensure that pyrene was not the source of the hydrocarbons detected, the electrolysis was again run in the absence of CO, but in the presence of pyrene. The resulting post-electrolysis gas chromatograph was negative for all hydrocarbons. Inconsistencies and variability between experiments made definitively characterizing and quantifying the products of reduction difficult to finalize so additional experiments are still required.

3.3 Conclusion

VFe, MoFe, and apo MoFe protein bioelectrodes were fabricated and used for the reduction of $NaNO_2$, NaN_3, CO and CO_2. Results from cyclic voltammetry using cobaltocenium hexafluorophoshpate as a mediator are consistent with electrocatalytic reduction of CO by VFe protein. Additionally, VFe and MoFe protein both appear active toward CO_2 reduction, albeit to a lesser extent. Analysis of products from controlled potential electrolysis found short chain C1-C3 hydrocarbons consistent with chemical reduction assays that mimic Fisher-Tropsch reactivity, but with inconsistent quantification of products. Future experiments are required to fully characterize the products of electrolysis.

3.4 Experimental Details

General considerations

All electrochemical experiments were carried out under an argon atmosphere in a Vacuum Atmospheres glovebox. All scans were obtained in a 75 mM, pH 7.4 HEPES (2-[4-(2-hydroxyethyl)piperazin-1-yl]ethanesulfonic acid) buffer containing 500 mM NaCl. All

experiments were performed with a Pine Wavedriver 10 potentiostat using Aftermath software. All potentials are referenced to the saturated calomel electrode (SCE, CH instruments) unless otherwise noted. All chemicals were purchased and used without further purification except water, ethylene glycol diglycidyl ether (EGDGE), HEPES buffer and Tris buffer, which were degassed, and CO_2 which is passed through a drying column before use. Glassy carbon electrodes were polished with 0.05 um alumina slurry before use.

Bioelectrode preparation

Isolated protein samples in this section were produced and provided by Dr. Johannes Rebelein, Dr. Nathaniel Sickerman, and Megan Newcomb from the Ribbe and Hu Laboratories.

To a 200 uL Eppendorf tube, poly(vinyl)amine hydrochloride (15 uL, 10 mg/mL aqueous solution) was mixed with MoFe, VFe, or apo MoFe protein (15 uL, 11.3 mg/mL Tris buffer) resulting in an off-white suspension. To this suspension, EGDGE (2 uL, 10% aqueous suspension) was added and mixed thoroughly. For cyclic voltammetry experiments, 1 uL of this mixture was added per 7.068 mm^2 (area of a 3 mm diameter disk) of polished glassy carbon electrode and spread with the tip of a micropipette. For electrolysis experiments, the protein-polymer cross-linked suspension was added in 1.25 uL portions to a polished glassy carbon rod and spread with a micropipette tip until full coverage was visually verified. The electrode was allowed to dry under argon for 1 hour and was then ready for use. In experiments where no protein is used, either an extra 15 uL portion of poly(vinyl)amine hydrochloride was used without protein, or a polished glassy carbon electrode was used.

Cyclic voltammetry experiments

Each electrode surface was prepared individually, meaning the consistency of the electrode surface is not identical for each sample. As a result, CV experiments were performed in a quadruplet series to maintain an internal consistency with each prepared electrode set. Using two identically prepared 3 mm disk glassy carbon electrodes CV experiments were performed in the order: 1) No Cc^+, no substrate, 2) No Cc^+, with substrate; second electrode: 3) with Cc^+, no substrate, 4) with Cc^+, with substrate. Experiments were performed in 10 mL of buffered solution with solid substrates at a 50 mM concentration. CV experiments with polished glassy carbon were performed with substrate at a 10 mM concentration with 500 mM supporting electrolyte to prevent problems encountered with diffusion. Gaseous substrates were vigorously bubbled into 10 mL of the analyte solution for 5 minutes prior to use. All scans contained the same electrode materials. Working electrode: 3 mm glassy carbon disk (CH Instruments), counter electrode: glassy carbon rod, and reference electrode: SCE (CH Instruments). Scans were run from –0.8 V to –1.36 V vs. SCE at a scan rate of 2 mV/s.

Controlled potential electrolysis experiments

Controlled potential electrolysis experiments were performed either in a single electrochemical cell 20 mL scintillation vial with a septa top or in a custom two compartment H-cell separated by a fine frit leaving 1-2 mL of headspace on the working electrode compartment to analyze gaseous products. A glassy carbon rod was coated with the protein-polymer suspension as described above. All electrolysis experiments contained less than or equal to 0.1 mL of Hg in the working electrode compartment to amalgamate potential heterogeneous products of electrolysis such as cobalt nanoparticles. The solution was scanned with cyclic

voltammetry at 50 mV/s to verify connectivity of the electrochemical cell and then stirred and electrolyzed at –1.26 V vs. SCE for 15.5 hours, before being analyzed via gas chromatography for hydrocarbons and dihydrogen.

3.5 References

(1) Robinson, P. K. *Essays Biochem.* **2015**, *59*, 1.

(2) Holm, R. H.; Kennepohl, P.; Solomon, E. I. *Chem. Rev.* **1996**, *96*, 2239.

(3) Solomon, E. I.; Heppner, D. E.; Johnston, E. M.; Ginsbach, J. W.; Cirera, J.; Qayyum, M.; Kieber-Emmons, M. T.; Kjaergaard, C. H.; Hadt, R. G.; Tian, L. *Chem. Rev.* **2014**, *114*, 3659.

(4) Karlin, K. D. *Science* **1993**, *261*, 701.

(5) Schwarz, G.; Mendel, R. R.; Ribbe, M. W. *Nature* **2009**, *460*, 839.

(6) Hitchman, M. L.; Nyasulu, F. W. M.; Aziz, A.; Chingakule, D. D. K. *Anal. Chim. Acta* **1983**, *155*, 219.

(7) Karyakin, A. A. *Bioelectrochemistry* **2012**, *88*, 70.

(8) Yahiro, A. T.; Lee, S. M.; Kimble, D. O. *Biochim. Biophys. Acta* **1964**, *88*, 375.

(9) Hill, H. A. *Biochem Soc Trans* **1983**, *11*, 453.

(10) Saveant, J.-M. *Elements of Molecular and Biomolecular Electrochemistry: An Electrochemical Approach to Electron Transfer Chemistry*; John Wiley & Sons, Inc.: Hoboken, N. J., 2006

(11) Cosnier, S. *Biosens. Bioelectron.* **1999**, *14*, 443.

(12) Heller, A. *Acc. Chem. Res.* **1990**, *23*, 128.

(13) Sheldon, R. A.; van Pelt, S. *Chem. Soc. Rev.* **2013**, *42*, 6223.

(14) Sheldon, R. A. *Adv. Synth. Catal.* **2007**, *349*, 1289.

(15) Wang, J. *Anal. Chim. Acta* **1999**, *399*, 21.

(16) Bourdillon, C.; Demaille, C.; Gueris, J.; Moiroux, J.; Saveant, J. M. *J. Am. Chem. Soc.* **1993**, *115*, 12264.

(17) Wollenberger, U.; Spricigo, R.; Leimkühler, S.; Schröder, K. In *Biosensing for the 21st Century*; Renneberg, R., Lisdat, F., Eds.; Springer Berlin Heidelberg: Berlin, Heidelberg, 2008, p 19.

(18) Ghindilis, A. L.; Atanasov, P.; Wilkins, E. *Electroanalysis* **1997**, *9*, 661.

(19) Léger, C.; Bertrand, P. *Chem. Rev.* **2008**, *108*, 2379.

(20) Shleev, S.; Tkac, J.; Christenson, A.; Ruzgas, T.; Yaropolov, A. I.; Whittaker, J. W.; Gorton, L. *Biosens. Bioelectron.* **2005**, *20*, 2517.

(21) Gorton, L.; Lindgren, A.; Larsson, T.; Munteanu, F. D.; Ruzgas, T.; Gazaryan, I. *Anal. Chim. Acta* **1999**, *400*, 91.

(22) Armstrong, F. A.; Hill, H. A. O.; Oliver, B. N.; Walton, N. J. *J. Am. Chem. Soc.* **1984**, *106*, 921.

(23) Armstrong, F. A.; Wilson, G. S. *Electrochim. Acta* **2000**, *45*, 2623.

(24) Frew, J. E.; Hill, H. A. O. *Eur. J. Biochem.* **1988**, *172*, 261.

(25) Cass, A. E. G.; Davis, G.; Francis, G. D.; Hill, H. A. O.; Aston, W. J.; Higgins, I. J.; Plotkin, E. V.; Scott, L. D. L.; Turner, A. P. F. *Anal. Chem.* **1984**, *56*, 667.

(26) Waniek, S. D.; Klett, J.; Forster, C.; Heinze, K. *Beilstein J Org Chem* **2018**, *14*, 1004.

(27) Şenel, M.; Çevik, E.; Abasıyanık, M. F. *Sensor. Actuat. B-Chem.* **2010**, *145*, 444.

(28) Krieger, A.; Rutherford, A. W.; Johnson, G. N. *Biochim. Biophys. Acta* **1995**, *1229*, 193.

(29) Milton, R. D.; Hickey, D. P.; Abdellaoui, S.; Lim, K.; Wu, F.; Tan, B.; Minteer, S. D. *Chem. Sci.* **2015**, *6*, 4867.

(30) Chamupathi, V. G.; Tollin, G. *Photochem. Photobiol.* **1990**, *51*, 611.

(31) Ackermann, Y.; Guschin, D. A.; Eckhard, K.; Shleev, S.; Schuhmann, W. *Electrochem. Commun.* **2010**, *12*, 640.

(32) He, Z.; Angenent, L. T. *Electroanalysis* **2006**, *18*, 2009.

(33) Ikeda, T.; Kano, K. *J. Biosci. Bioeng.* **2001**, *92*, 9.

(34) Cooney, M. J.; Svoboda, V.; Lau, C.; Martin, G.; Minteer, S. D. *Energy Environ. Sci.* **2008**, *1*, 320.

(35) Meredith, M. T.; Minteer, S. D. *Annu. Rev. Anal. Chem.* **2012**, *5*, 157.

(36) Minteer, S. D.; Liaw, B. Y.; Cooney, M. J. *Curr.Opin. Biotech.* **2007**, *18*, 228.

(37) Yu, H.; Hebling, C.; Revathi, S. In *Reference Module in Materials Science and Materials Engineering*; Elsevier: 2016.

(38) Lee, H.-S.; Yu, J.-K.; Kim, J.-Y.; Kim, K.-H.; Rhee, Y.-W. In *Studies in Surface Science and Catalysis*; Rhee, H.-K., Nam, I.-S., Park, J. M., Eds.; Elsevier: 2006; Vol. 159, p 589.

(39) Leech, D.; Kavanagh, P.; Schuhmann, W. *Electrochim. Acta* **2012**, *84*, 223.

(40) Merchant, S. A.; Meredith, M. T.; Tran, T. O.; Brunski, D. B.; Johnson, M. B.; Glatzhofer, D. T.; Schmidtke, D. W. *J. Phys. Chem. C* **2010**, *114*, 11627.

(41) Solomon, E. I.; Sundaram, U. M.; Machonkin, T. E. *Chem. Rev.* **1996**, *96*, 2563.

(42) Armstrong, F. A.; Evans, R. M.; Hexter, S. V.; Murphy, B. J.; Roessler, M. M.; Wulff, P. *Acc. Chem. Res.* **2016**, *49*, 884.

(43) Evans, R. M.; Siritanaratkul, B.; Megarity, C. F.; Pandey, K.; Esterle, T. F.; Badiani, S.; Armstrong, F. A. *Chem. Soc. Rev.* **2019**.

(44) Chenevier, P.; Mugherli, L.; Darbe, S.; Darchy, L.; DiManno, S.; Tran, P. D.; Valentino, F.; Iannello, M.; Volbeda, A.; Cavazza, C.; Artero, V. *C. R. Chim.* **2013**, *16*, 491.

(45) Milton, R. D.; Abdellaoui, S.; Khadka, N.; Dean, D. R.; Leech, D.; Seefeldt, L. C.; Minteer, S. D. *Energy Environ. Sci.* **2016**, *9*, 2550.

(46) Khanova, L. A.; Topolev, V. V.; Krishtalik, L. I. *Chem. Phys.* **2006**, *326*, 33.

(47) Lee, C. C.; Hu, Y.; Ribbe, M. W. *Science* **2010**, *329*, 642.

(48) Hu, Y.; Lee, C. C.; Ribbe, M. W. *Dalton Trans.* **2012**, *41*, 1118.

(49) Lee, C. C.; Hu, Y.; Ribbe, M. W. *Angew. Chem. Int. Ed.* **2012**, *51*, 1947.

(50) Lee, C. C.; Hu, Y.; Ribbe, M. W. *Angew. Chem. Int. Ed.* **2015**, *54*, 1219.

(51) Rebelein, J. G.; Hu, Y.; Ribbe, M. W. *ChemBioChem* **2015**, *16*, 1993.

(52) Chung, L. C.; Kazuki, T.; Megan, N.; Jasper, L.; Yilin, H.; W., R. M. *ChemBioChem* **2018**, *19*, 649.

(53) Vincent, K. A.; Tilley, G. J.; Quammie, N. C.; Streeter, I.; Burgess, B. K.; Cheesman, M. R.; Armstrong, F. A. *Chem. Commun.* **2003**, 2590.

(54) Szostak, M.; Spain, M.; Procter, D. J. *J. Org. Chem.* **2014**, *79*, 2522.

(55) Sickerman, N. S.; Tanifuji, K.; Lee, C. C.; Ohki, Y.; Tatsumi, K.; Ribbe, M. W.; Hu, Y. *J. Am. Chem. Soc.* **2017**, *139*, 603.

(56) Sippel, D.; Einsle, O. *Nat Chem Biol* **2017**, *13*, 956.

(57) Lee, C. C.; Hu, Y.; Ribbe, M. W.; Holm, R. H. *Proc. Natl. Acad. Sci. U.S.A.* **2009**, *106*, 9209.

(58) Vaughn, S. A.; Burgess, B. K. *Biochemistry* **1989**, *28*, 419.

(59) Shaw, S.; Lukoyanov, D.; Danyal, K.; Dean, D. R.; Hoffman, B. M.; Seefeldt, L. C. *J. Am. Chem. Soc.* **2014**, *136*, 12776.

(60) Bard, A. J.; Faulkner, L. R. *Electrochemical Methods: Fundamentals and Applications*; 2 ed.; Wiley: New York, 2001.

(61) Fisher, K.; Dilworth, M. J.; Newton, W. E. *Biochemistry* **2000**, *39*, 15570.

(62) Fisher, K.; Dilworth, M. J.; Newton, W. E. *Biochemistry* **2006**, *45*, 4190.

(63) Christiansen, J.; Seefeldt, L. C.; Dean, D. R. *J Biol Chem* **2000**, *275*, 36104.

(64) Lee, C. C.; Tanifuji, K.; Newcomb, M.; Liedtke, J.; Hu, Y.; Ribbe, M. W. *ChemBioChem* **2018**, *19*, 649.

(65) Rebelein, J. G.; Stiebritz, M. T.; Lee, C. C.; Hu, Y. *Nat Chem Biol* **2017**, *13*, 147.

(66) Hu, B.; Harris, D. F.; Dean, D. R.; Liu, T. L.; Yang, Z.-Y.; Seefeldt, L. C. *Bioelectrochemistry* **2018**, *120*, 104.